

# NLO QCD+EW predictions for $2\ell 2\nu$ diboson signatures at the LHC

---

S. Kallweit,<sup>a</sup> J. M. Lindert,<sup>b</sup> S. Pozzorini,<sup>c</sup> and M. Schönherr<sup>c</sup>

<sup>a</sup>*TH Division, Physics Department, CERN, CH-1211 Geneva 23, Switzerland*

<sup>b</sup>*Institute for Particle Physics Phenomenology, Durham University, Durham DH1 3LE, UK*

<sup>c</sup>*Physik-Institut, Universität Zürich, Winterthurerstrasse 190, CH-8057 Zürich, Switzerland*

*E-mail:* [stefan.kallweit@cern.ch](mailto:stefan.kallweit@cern.ch), [lindert@physik.uzh.ch](mailto:lindert@physik.uzh.ch),  
[pozzorin@physik.uzh.ch](mailto:pozzorin@physik.uzh.ch), [marek.schoenherr@physik.uzh.ch](mailto:marek.schoenherr@physik.uzh.ch)

**ABSTRACT:** We present next-to-leading order (NLO) calculations including QCD and electroweak (EW) corrections for  $2\ell 2\nu$  diboson signatures with two opposite-charge leptons and two neutrinos. Specifically, we study the processes  $pp \rightarrow e^+\mu^-\nu_e\bar{\nu}_\mu$  and  $pp \rightarrow e^+e^-\nu\bar{\nu}$ , including all relevant off-shell diboson channels,  $W^+W^-$ ,  $ZZ$ ,  $\gamma Z$ , as well as non-resonant contributions. Photon-induced processes are computed at NLO EW, and we discuss subtle differences related to the definition and the renormalisation of the coupling  $\alpha$  for processes with initial- and final-state photons. All calculations are performed within the automated MUNICH/SHERPA+OPENLOOPS frameworks, and we provide numerical predictions for the LHC at 13 TeV. The behaviour of the corrections is investigated with emphasis on the high-energy regime, where NLO EW effects can amount to tens of percent due to large Sudakov logarithms. The interplay between  $WW$  and  $ZZ$  contributions to the same-flavour channel,  $pp \rightarrow e^+e^-\nu\bar{\nu}$ , is discussed in detail, and a quantitative analysis of photon-induced contributions is presented. Finally, we consider approximations that account for all sources of large logarithms, at high and low energy, by combining virtual EW corrections with a YFS soft-photon resummation or a QED parton shower.

**KEYWORDS:** Electroweak radiative corrections, NLO computations, Hadronic colliders

---

## Contents

<b>1</b>	<b>Introduction</b>	<b>1</b>
<b>2</b>	<b>Anatomy of hadronic <math>2\ell 2\nu</math> production at NLO QCD+EW</b>	<b>3</b>
2.1	Categorisation of $2\ell 2\nu$ final states	3
2.2	Photon-induced production	5
2.3	Ingredients of QCD and EW corrections	6
<b>3</b>	<b>Technical ingredients and setup of the simulations</b>	<b>7</b>
3.1	Tools	7
3.2	YFS soft-photon resummation and QED parton shower	8
3.3	Input parameters, scale choices and variations	9
3.4	PDFs	10
<b>4</b>	<b>Results</b>	<b>12</b>
4.1	The different-flavour channel $pp \rightarrow e^+ \mu^- \nu_e \bar{\nu}_\mu$	14
4.2	The same-flavour channel $pp \rightarrow e^+ e^- \nu \bar{\nu}$	20
<b>5</b>	<b>Summary and conclusions</b>	<b>26</b>
<b>A</b>	<b>Infrared subtraction, <math>\gamma</math>PDF renormalisation and definition of <math>\alpha</math></b>	<b>27</b>
A.1	Catani–Seymour subtraction at $\mathcal{O}(\alpha)$	27
A.2	$\gamma$ PDF renormalisation	31
A.3	Definition and renormalisation of $\alpha$ in processes with external photons	32
<b>B</b>	<b>Flavour-number scheme conversion</b>	<b>34</b>
<b>C</b>	<b>Electroweak corrections by parton luminosity</b>	<b>35</b>
<b>D</b>	<b>Cross section tables</b>	<b>36</b>

---

## 1 Introduction

The production of vector-boson pairs,  $W^+W^-$ ,  $W^\pm Z$  and  $ZZ$ , plays an important role in various areas of the LHC physics programme. Experimental studies of this family of processes permit to test key aspects of the Standard Model (SM) at energies that range from the EW scale up to the TeV regime. In particular, due to the high sensitivity to anomalous trilinear couplings, differential measurements at high transverse momentum allow one to test the gauge symmetry structure of EW interactions and to search for indirect effects of physics Beyond the Standard Model (BSM). Diboson final states are widely studied also in the context of direct BSM searches. Moreover, they play the role of nontrivial backgrounds in a broad range of measurements and searches. Most notably, they represent the irreducible background to Higgs-boson analyses in the  $H \rightarrow W^+W^-$  and  $H \rightarrow ZZ$  decay modes. These motivations, together with the increasing level of accuracy of experimental measurements, call for continuous improvements in the theoretical description of diboson production at the LHC.

Leptonically decaying vector-boson pairs yield clean experimental signatures with charged leptons and neutrinos. In this paper we focus on final states with two opposite-charge leptons and two neutrinos, generically denoted as  $2\ell 2\nu$ . Their production is dominated by  $W^+W^-$  resonances, resulting in the highest cross sections among the various channels with dibosons decaying into charged leptons and neutrinos. The resonant structure of  $pp \rightarrow 2\ell 2\nu$  depends on the lepton-flavour configuration, and we consider both the case of different and same charged-lepton flavours. In the different-flavour case,  $\ell_i^+ \ell_j^- \nu_i \bar{\nu}_j$  with  $\ell_i \neq \ell_j$ , only  $W^+W^-$  resonances contribute, whereas same-flavour final states,  $\ell_i^+ \ell_i^- \nu_k \bar{\nu}_k$ , can arise both through  $W^+W^-$  and  $ZZ$  resonances. While  $2\ell 2\nu$  production is dominated by resonant contributions, off-shell effects and non-resonant topologies play an important role for various phenomenological studies, for instance in  $H \rightarrow VV$  studies, where selection cuts or kinematic discriminants can force diboson backgrounds into the off-shell regime.

Theoretical predictions for  $W^+W^-$  and  $ZZ$  production and decays are available up to next-to-next-to-leading order (NNLO) in QCD [1–4]. More precisely, NNLO QCD predictions for  $2\ell 2\nu$  production have been published only in the  $W^+W^-$  mediated channel  $pp \rightarrow e^+ \mu^- \nu_e \bar{\nu}_\mu$  [2], while NNLO QCD calculations for  $ZZ$  mediated processes exist only for the  $pp \rightarrow 4\ell$  channel to date. At higher orders in QCD, both processes receive sizeable contributions from the opening of gluon-induced channels, and the important impact of QCD radiation results in a pronounced sensitivity to jet vetoes. Also loop-induced contributions from gluon fusion, known up to  $\mathcal{O}(\alpha_s^3)$  [5, 6], play an important role.

In order to reach the level of precision required by present and future experimental analyses, higher-order QCD predictions need to be supplemented by EW correction effects. In general, the dominant EW corrections are due to QED radiation effects in the distributions of final-state leptons, and large Sudakov logarithms that arise at scattering energies  $Q^2 \gg M_W^2$  [7]. The importance of EW Sudakov logarithms for  $pp \rightarrow W^+W^-/ZZ$  at the LHC was demonstrated in [8] and confirmed by full NLO EW calculations for on-shell vector-boson production [9–11]. At the TeV scale, due to the large SU(2) charges of  $W$  and  $Z$  bosons, EW Sudakov corrections can reach the level of 50% at  $\mathcal{O}(\alpha)$ , and also higher-order Sudakov EW effects become significant. For the case of  $W^+W^-$  production, corresponding results are available up to  $\mathcal{O}(\alpha^2)$  to NNLL accuracy [12].

A first calculation that includes diboson production and decays at NLO EW was performed for the different-flavour process  $pp \rightarrow W^+W^- \rightarrow e^+ \mu^- \nu_e \bar{\nu}_\mu$  using a spin-correlated double-pole approximation (DPA) [13]. More recently, full NLO EW predictions for the  $ZZ$  and  $W^+W^-$  mediated processes  $pp \rightarrow 4\ell$  [14, 15] and  $pp \rightarrow e^+ \mu^- \nu_e \bar{\nu}_\mu$  [16] became available. Here, at variance with the DPA, off-shell effects are fully included, and also non-resonant topologies are taken into account. This is crucial for analyses targeted at off-shell phase-space regions, such as  $H \rightarrow VV$  measurements, but also for lepton- $p_T$  distributions and other observables [16].

Besides the dominant  $q\bar{q}$  annihilation channel, also the  $\gamma\gamma$  channel enters  $pp \rightarrow W^+W^-$  at leading order (LO), contributing twice as much as the  $c\bar{c}$ -channel. The  $\gamma\gamma$  channel raises the inclusive cross section by about +1% at LO, and, due to the comparably large photon PDF at high  $x$ , it contributes significantly more at large transverse momenta or invariant masses. In the literature, photon-induced contributions to  $pp \rightarrow VV$  are typically included at LO, and the corresponding NLO EW corrections have been studied only for  $\gamma\gamma \rightarrow W^+W^-$  at a  $\gamma\gamma$  collider [17–19] and for the production of stable vector bosons at the LHC [10]. The quantitative impact of photon-induced diboson production and the related uncertainty strongly depend on the photon distribution function ( $\gamma$ PDF) supplied by the different PDF groups [20–23].

In this paper we present new NLO calculations of  $pp \rightarrow 2\ell 2\nu$  that extend previous results in various directions. First, we include both NLO QCD and EW corrections and address also the issue of their combination, which is of particular relevance in phase-space regions where both types of corrections are large, e.g. in the tails of transverse-momentum distributions. Second,

besides revisiting the different-flavour  $e^+\mu^-\nu_e\bar{\nu}_\mu$  channel, for the first time we also study the same-flavour  $e^+e^-\nu\bar{\nu}$  channel at NLO EW, including all relevant off-shell and non-resonant effects, as well as interferences and spin correlations. In the same-flavour channel, we investigate the relative importance of  $W^+W^-$  and  $ZZ$  resonances and of their interference. In particular, while  $ZZ$  resonances are generally subdominant, we point out that for certain distributions they can play a significant role. Third, at variance with previous studies, we treat  $q\bar{q}$ - and  $\gamma\gamma$ -induced channels on the same footing, including NLO EW corrections throughout, and not only for the  $q\bar{q}$  channel. In this respect, we note that the EW corrections to the  $q\bar{q}$  channel involve  $q\gamma$ -induced processes that are related—via cancellations of collinear singularities—to the EW corrections to the  $\gamma\gamma$  channel. Thus, the EW corrections to the  $\gamma\gamma$  channel are mandatory for a fully consistent treatment of  $pp \rightarrow 2\ell 2\nu$  at NLO EW. Fourth, we assess the importance of photon-induced contributions and related uncertainties based on various state-of-the-art PDFs and their comparison. Fifth, we study a convenient approximation of the EW corrections amenable to a simplified form of matching to parton showers and multi-jet merging at NLO QCD+EW [24]. Specifically, we consider IR regularised virtual EW corrections supplemented with QED radiation as described by YFS soft-photon resummation or, alternatively, by a QED parton shower.

Finally, motivated by subtleties that arise from photon-induced processes at NLO EW, we present a complete  $\mathcal{O}(\alpha)$  analysis of the interplay between the definition of the electromagnetic coupling and the renormalisation of the photon wave function and of the  $\gamma$ PDF in processes with external photons. In particular, we demonstrate that, in order to avoid large logarithms of the light-quark and lepton masses associated with  $\Delta\alpha(M_Z^2)$ , the coupling of initial-state photons should be defined at the scale  $\mu_F^2$  or at the EW scale, using, for instance, the  $G_\mu$  scheme or  $\alpha(M_Z)$  scheme. This was first pointed out in [25], based on considerations related to the evolution of the  $\gamma$ PDF at LO. In contrast, as is well known, for final-state photons  $\alpha(0)$  should be used.

The calculations presented in this paper have been performed with the fully automated NLO QCD+EW framework [24, 26] provided by the OPENLOOPS matrix-element generator [27, 28] in combination with the Monte Carlo programs MUNICH [29] and SHERPA [30–33].

This paper is organised as follows: In Section 2 we introduce general features and ingredients of  $pp \rightarrow 2\ell 2\nu$ , while technical aspects of the calculations are detailed in Section 3. Numerical predictions for the 13 TeV LHC are presented in Section 4, with emphasis on the behaviour of QCD and EW corrections, and our findings are summarised in Section 5. In Appendix A we document the implementation of Catani–Seymour subtraction at  $\mathcal{O}(\alpha)$  in SHERPA and MUNICH, and we discuss the issue of the definition and renormalisation of  $\alpha$  for processes with external photons. Technical details related to the separation of single-top contamination at NLO QCD are addressed in Appendix B. Appendix C details a breakdown of the electroweak corrections presented in Section 4 by flavour channels. Finally, in Appendix D we present benchmark cross sections for  $pp \rightarrow 2\ell 2\nu$  in various fiducial regions.

## 2 Anatomy of hadronic $2\ell 2\nu$ production at NLO QCD+EW

### 2.1 Categorisation of $2\ell 2\nu$ final states

In the Standard Model, the signature of two opposite-charged leptons and missing energy is dominantly produced through  $pp \rightarrow W^+W^-/ZZ \rightarrow 2\ell 2\nu$ , i.e. with two types of diboson resonances that decay into two leptons and two neutrinos. Such signatures can be categorized according to the flavour of the two charged leptons into a different-flavour (DF) mode and a same-flavour (SF) mode, with different implications on the underlying production mechanisms. We restrict our discussion to final states with electrons and muons, and we focus on  $pp \rightarrow 2\ell 2\nu$  processes with DF and SF final states corresponding, respectively, to  $e^+\mu^- + \cancel{E}_T$  and  $e^+e^- + \cancel{E}_T$ . Note that such processes

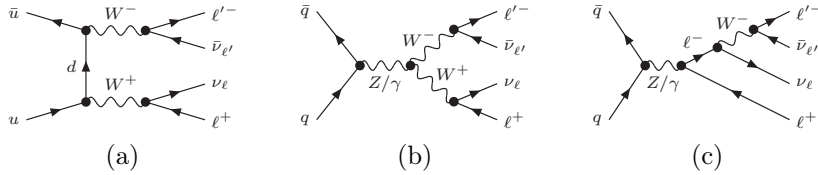


**Figure 1.** Sample of Born diagrams contributing to  $2\ell 2\nu$  production in the different-flavour case ( $\ell \neq \ell'$ ) and in the same-flavour case ( $\ell = \ell'$ ). Both double-resonant (a,b) and single-resonant (c) diagrams are shown.

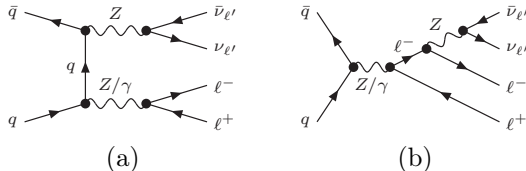


**Figure 2.** Sample of Born diagrams contributing to  $2\ell 2\nu$  final states only in the case of same lepton flavour (neutrinos can have flavour  $\ell' = \ell$  or  $\ell' \neq \ell$ ). Both double-resonant (a) and single-resonant (b) diagrams are shown.

are invariant with respect to  $e \leftrightarrow \mu$  interchange. More precisely, taking into account appropriate momentum mappings, we have

$$\begin{aligned}
 d\sigma(pp \rightarrow \mu^+ e^- \nu_\mu \bar{\nu}_e) &= d\sigma(pp \rightarrow e^+ \mu^- \nu_e \bar{\nu}_\mu), \\
 d\sigma(pp \rightarrow \mu^+ \mu^- \nu_\mu \bar{\nu}_\mu) &= d\sigma(pp \rightarrow e^+ e^- \nu_e \bar{\nu}_e), \\
 d\sigma(pp \rightarrow \mu^+ \mu^- \nu_{e/\tau} \bar{\nu}_{e/\tau}) &= d\sigma(pp \rightarrow e^+ e^- \nu_{\mu/\tau} \bar{\nu}_{\mu/\tau}).
 \end{aligned}
 \tag{2.1}$$

In our calculation we do not apply any resonance approximation, but include the full set of Feynman diagrams that contribute to  $pp \rightarrow 2\ell 2\nu$  at each perturbative order, thereby including all sub-dominant contributions with single- and non-resonant diagrams besides the dominant double-resonant ones. All off-shell effects, interferences and spin correlations are consistently taken into account, treating resonances in the complex-mass scheme [34] throughout.

At LO, the DF process  $pp \rightarrow e^+ \mu^- \nu_e \bar{\nu}_\mu$ , is dominated by resonant  $W^+ W^-$  production in the  $q\bar{q}$  channel and subsequent decays. The full set of Feynman diagrams contributing to  $pp \rightarrow e^+ \mu^- \nu_e \bar{\nu}_\mu$  will be referred to as  $\text{DF}_{WW}$  channel. Representative tree-level diagrams both for double-resonant and sub-leading contributions are shown in Fig. 1.

The situation in the SF case is more involved since its signature can be produced by different partonic processes,  $pp \rightarrow e^+ e^- \nu_{\mu/\tau} \bar{\nu}_{\mu/\tau}$  and  $pp \rightarrow e^+ e^- \nu_e \bar{\nu}_e$ . Their final states are indistinguishable on an event-wise level, as the produced neutrinos can only be detected as missing transverse energy and their flavours cannot be resolved. Consequently, predictions for  $e^+ e^- + \cancel{E}_T$  production originate as the incoherent sum over all three possible neutrino-flavour contributions.

The SF process  $pp \rightarrow e^+ e^- \nu_{\mu/\tau} \bar{\nu}_{\mu/\tau}$  is dominated by resonant  $ZZ$  production in  $q\bar{q}$  annihilation and subsequent  $Z \rightarrow e^+ e^-$  and  $Z \rightarrow \nu \bar{\nu}$  decays. Such double-resonant contributions are accompanied by all allowed topologies with sub-leading resonance structures, including diagrams with  $\gamma^* \rightarrow e^+ e^-$  subtopologies, as well as other single- and non-resonant topologies. The full set of Feynman diagrams contributing to  $pp \rightarrow e^+ e^- \nu_{\mu/\tau} \bar{\nu}_{\mu/\tau}$  will be referred to as  $\text{SF}_{ZZ}$  channel. Sample tree-level diagrams are depicted in Fig. 2.

Finally, the SF process  $pp \rightarrow e^+ e^- \nu_e \bar{\nu}_e$  proceeds both via  $W^+ W^-$  and  $ZZ$  diboson resonances. The corresponding amplitudes are built by coherently summing over all diagrams entering the

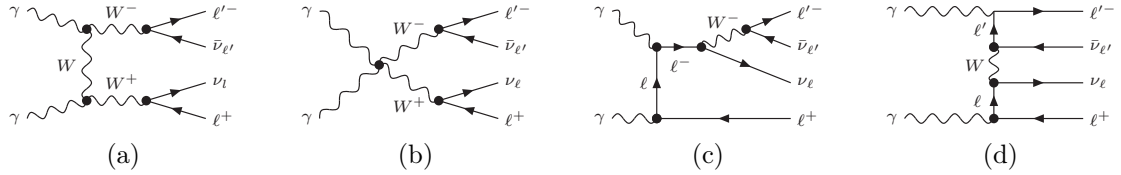


**Figure 3.** Sample of photon-induced Born diagrams contributing to  $2\ell 2\nu$  production in the different-flavour case ( $\ell \neq \ell'$ ) and in the same-flavour case ( $\ell = \ell'$ ). Double-resonant (a,b), single-resonant (c) and non-resonant (d) diagrams are shown.

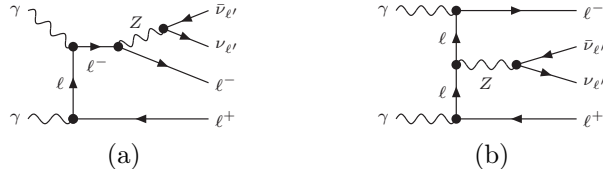


**Figure 4.** Sample of photon-induced Born diagrams contributing to  $2\ell 2\nu$  final states only in the same-lepton-flavour case, both for  $\ell' = \ell$  or  $\ell' \neq \ell$ . Only single-resonant diagrams contribute.

two previously discussed  $\text{DF}_{WW}$  and  $\text{SF}_{ZZ}$  channels. Consequently, this channel is referred to as  $\text{SF}_{WW/ZZ}$  channel, and all diagrams shown in Figs. 1–2 are representatives of the tree-level diagrams contributing here.

Due to the fact that the phase-space regions with resonant intermediate  $W^+W^-$  and  $ZZ$  states are typically distinct, the assumption is justified that the  $\text{SF}_{WW/ZZ}$  cross section is dominated by the incoherent sum of double-resonant contributions of one and the other type, while the effect of quantum interferences is small. It is, however, not obvious if this assumption still holds in phase-space regions away from such double-resonant topologies. Interference effects are studied in detail in Section 4.2 by comparing exact predictions in the  $\text{SF}_{WW/ZZ}$  channel against the incoherent sum of the  $W^+W^-$  and  $ZZ$  channels.

## 2.2 Photon-induced production

Besides the dominant  $q\bar{q}$  production mode,  $2\ell 2\nu$  final states can also be produced in photon-photon scattering. As we do not count the photon PDF as an  $\mathcal{O}(\alpha)$  suppressed quantity, such  $\gamma\gamma \rightarrow 2\ell 2\nu$  processes contribute already at the LO, i.e. at  $\mathcal{O}(\alpha^4)$ . Their quantitative relevance varies significantly between the channels. Photon-induced contributions to the DF channel are dominated by  $\gamma\gamma \rightarrow W^+W^- \rightarrow e^+\mu^-\nu_e\bar{\nu}_\mu$  topologies, which are accompanied by single-resonant topologies involving  $t$ -channel lepton-pair production with an emission of a  $W$  boson off one of the produced leptons, and non-resonant diagrams with multiperipheral topologies. Sample tree diagrams for the described DF topologies are collected in Fig. 3. Due to a  $t$ -channel pole, regulated by the  $W$  mass, the contribution of the double-resonant diagram depicted in Fig. 3(a) is enhanced for large invariant masses of the intermediate  $W^+W^-$  pair [9, 10]. In fact, for on-shell  $W^+W^-$  pair production the contribution of the  $\gamma\gamma$  channel was found to increase beyond 10% of the LO  $q\bar{q}$  annihilation mode for  $m_{WW} > 800$  GeV [9]. In this paper we investigate the significance of the  $\gamma$ -induced production mode using state-of-the-art PDFs and taking into account NLO EW corrections, as well as realistic selection cuts on the  $2\ell 2\nu$  final state.

The DF channel  $\gamma\gamma \rightarrow e^+e^-\nu_{\mu/\tau}\bar{\nu}_{\mu/\tau}$  does not involve any double-resonant topology due the lack of triple and quartic gauge couplings among neutral EW bosons. Similarly, non-resonant multiperipheral topologies do not exist due to lepton-flavour conservation. Thus, lepton-pair production

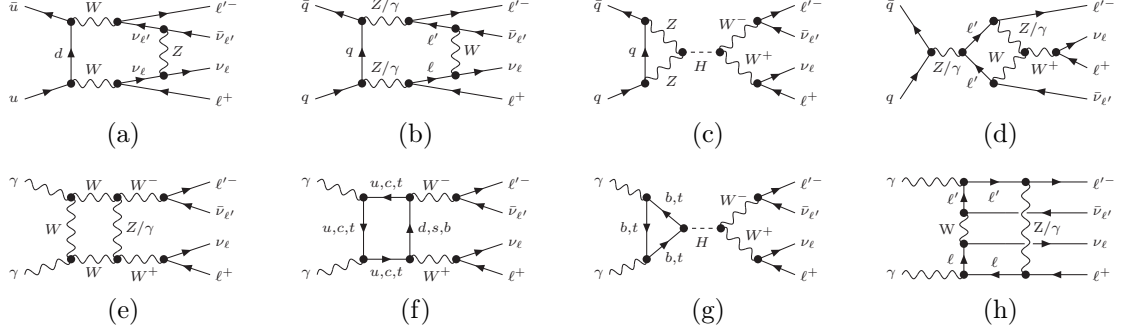


**Figure 5.** Sample of one loop diagrams contributing to  $2\ell 2\nu$  production in the different-flavour case ( $\ell \neq \ell'$ ) and in the same-flavour case ( $\ell = \ell'$ ) in the quark-induced (a-d) and photon-induced (e-h) channels.

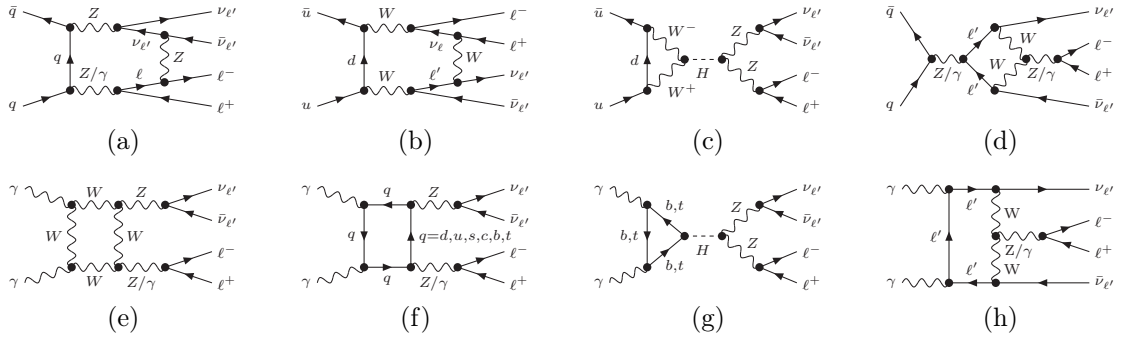


**Figure 6.** Sample of one-loop diagrams contributing to  $2\ell 2\nu$  final states only in the same-flavour (wrt. the charged leptons) case in the quark-induced (a-d) and photon-induced (e-h) channels.

in  $t$ -channel topologies with subsequent emission of a  $Z$  boson with  $Z \rightarrow \nu\bar{\nu}$  is the only photon-induced production mechanism at LO, as shown in the sample diagrams of Fig. 4. Consequently, the invariant mass of the charged-lepton pair does not show a Breit–Wigner peak around  $M_Z$ .

Similarly as for quark–antiquark annihilation, the  $\gamma\gamma \rightarrow e^+e^-\nu_e\bar{\nu}_e$  channel is build from the coherent sum of all diagrams entering  $\gamma\gamma \rightarrow e^+\mu^-\nu_e\bar{\nu}_\mu$  and  $\gamma\gamma \rightarrow e^+e^-\nu_\mu/\tau\bar{\nu}_\mu/\tau$ .

### 2.3 Ingredients of QCD and EW corrections

At NLO QCD all  $\mathcal{O}(\alpha_s\alpha^4)$  contributions to  $pp \rightarrow 2\ell 2\nu$  are taken into account. In the  $q\bar{q}$  channel, the only QCD loop corrections arise from virtual-gluon exchange, while the real corrections result from real-gluon emission and crossed topologies describing (anti-)quark–gluon channels. The infrared divergences separately arising in these two contributions are mediated by the standard dipole-subtraction approach [35, 36]. We note that the  $\gamma\gamma$  channels do not receive QCD corrections at NLO, due to the absence of any QCD partons in all tree-level diagrams.

At NLO EW we include the full set of  $\mathcal{O}(\alpha^5)$  contributions to  $pp \rightarrow 2\ell 2\nu$ . At this order both the  $q\bar{q}$  and  $\gamma\gamma$  channels receive corrections from virtual EW bosons and from closed fermion loops, cf. Figs. 5–6. These corrections include Higgs resonances with decay into four fermions coupled to weak bosons (in the  $q\bar{q}$  channel) or coupled to a heavy-fermion loop (in the  $\gamma\gamma$  channel). The real corrections in the  $q\bar{q}$  channel can be split into real-photon emission channels and  $\gamma q \rightarrow 2\ell 2\nu q$  channels<sup>1</sup> with initial-state  $\gamma \rightarrow q\bar{q}$  splittings. The  $\gamma\gamma$  channel also receives real corrections from

<sup>1</sup>Corresponding  $\gamma\bar{q}$ -induced channels are implicitly understood here and in the following.



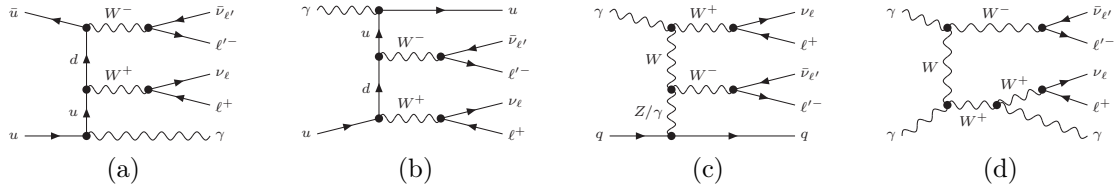


**Figure 7.** Sample of real emission diagrams contributing to  $2\ell 2\nu$  production in the different-flavour case ( $\ell \neq \ell'$ ) and in the same-flavour case ( $\ell = \ell'$ ), in the quark–antiquark channel (a), the (anti-)quark–photon channel (b,c) and the photon–photon channel (d).

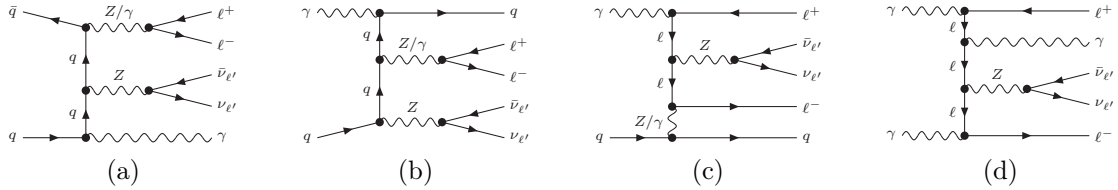


**Figure 8.** Sample of real emission diagrams contributing to  $2\ell 2\nu$  final states only in the same-flavour (wrt. the charged leptons) case in the quark–antiquark channel (a), the (anti-)quark–photon channel (b,c) and the photon–photon channel (d).

photon bremsstrahlung, and also from  $\gamma q \rightarrow 2\ell 2\nu q$  channels with initial-state  $q \rightarrow q\gamma$  splittings, cf. Figs. 7–8. While the separation into  $q\bar{q}$  and  $\gamma\gamma$  channels can still be preserved for virtual and photon-bremsstrahlung contributions, such separation is no longer meaningful for the  $q\gamma$ -initiated channels due to their singularity structure: both above-mentioned splittings result in infrared-divergent configurations, and these  $q\gamma$  channels simultaneously cancel infrared poles arising in  $q\bar{q}$  and  $\gamma\gamma$  channels. This situation demands the inclusion of the full NLO EW corrections to the  $q\bar{q}$  and  $\gamma\gamma$  Born processes to guarantee infrared safety and consistency. To deal with the mediation of these divergences between virtual and real corrections the QED extension of the dipole-subtraction method [37–39] is applied (see Appendix A).

Instead of a separation of NLO contributions into  $q\bar{q}$  and  $\gamma\gamma$  channels, we quantify the impact of photon-induced processes by considering contributions involving at least one photon PDF factor and all other contributions that are also present under the assumption of vanishing photon PDFs. At LO this distinction coincides with the splitting according to production modes, while at NLO EW it combines  $\gamma\gamma$  and  $q\gamma$  channels in spite of the fact that the latter involves  $q\bar{q}$ -related contributions.

### 3 Technical ingredients and setup of the simulations

#### 3.1 Tools

The calculations presented in this paper have been performed with the automated frameworks MUNCH+OPENLOOPS and SHERPA+OPENLOOPS. They automate the full chain of all operations—from process definition to collider observables—that enter NLO QCD+EW simulations at parton level. The recently achieved automation of EW corrections [24, 26] is based on the well established QCD implementations and allows for NLO QCD+EW simulations for a vast range of SM processes, up to high particle multiplicities, at current and future colliders.

In these frameworks virtual amplitudes are provided by the OPENLOOPS program [28], which is based on the open-loops algorithm [27] – a fast numerical recursion for the evaluation of one-loop scattering amplitudes. Combined with the COLLIER tensor reduction library [40], which imple-



ments the Denner–Dittmaier reduction techniques [41, 42] and the scalar integrals of [43], or with CUTTOOLS [44], which implements the OPP method [45], together with the ONELOOP library [46], the employed recursion permits to achieve very high CPU performance and a high degree of numerical stability. We validated phase-space point wise the contributing tree amplitudes between SHERPA and OPENLOOPS, and the one-loop amplitudes between OPENLOOPS and an in-house algebraic amplitude generator and also against RECOLA [47]. All remaining tasks, i.e. the bookkeeping of partonic subprocesses, phase-space integration, and the subtraction of QCD and QED bremsstrahlung, are supported by the two independent and fully automated Monte Carlo generators, MUNICH [29] and SHERPA [30–33]. These two tools have been validated extensively against each other. As a further validation of the Monte Carlo integration employed for the results presented here, we want to note the perfect agreement between SHERPA and the results of [16] for the related process  $pp \rightarrow 4\ell$  presented in [48].

### 3.2 YFS soft-photon resummation and QED parton shower

As discussed in Section 1, the NLO EW corrections to  $pp \rightarrow 2\ell 2\nu$  are dominated by EW Sudakov logarithms of virtual origin and QED logarithms stemming from photon radiation off leptons. In [24] it was shown that, for observables that are sufficiently inclusive with respect to photon radiation, full NLO EW results can be reproduced with good accuracy by an approximation consisting only of virtual EW corrections upon appropriate subtraction of IR singularities. This approximation, which was dubbed  $\text{EW}_{\text{VI}}$ , is defined through

$$d\sigma_{\text{NLO EW}_{\text{VI}}} = d\sigma_{\text{LO}} + d\sigma_{\text{EW}}^{\text{V}} + d\sigma_{\text{EW}}^{\text{I}} = d\sigma_{\text{LO}} (1 + \delta_{\text{EW}_{\text{VI}}}) . \quad (3.1)$$

Therein,  $d\sigma_{\text{LO}}$  is the leading order differential cross section, while  $d\sigma_{\text{EW}}^{\text{V}}$  and  $d\sigma_{\text{EW}}^{\text{I}}$  are the NLO EW virtual correction and the endpoint part of the integrated Catani-Seymour subtraction terms, ensuring a finite result by construction. In practice, a logarithmic approximation over the real photon emission phase space is added to the virtual corrections. This approach captures all Sudakov effects at NLO EW [49] and is very suitable for a combination of QCD and EW higher-order effects through a simplified multi-jet merging approach at NLO QCD+EW [24]. As a further possible step towards a fully consistent implementation of matching and merging at NLO QCD+EW, in this paper we investigate the possibility of supplementing the  $\text{EW}_{\text{VI}}$  approximation with QED radiation effects by means of naive matching to QED parton showers or QED resummation. Specifically, we consider a soft-photon resummation in the Yennie-Frautschi-Suura (YFS) scheme [50] and, alternatively, the CSSHOWER QED parton shower [51, 52] based on Catani-Seymour splitting kernels. Combined with the  $\text{EW}_{\text{VI}}$  approximation and a differentially applied NLO QCD  $K$ -factor, the NLO QCD $\times$ EW $_{\text{VI}} \otimes$  YFS and NLO QCD $\times$ EW $_{\text{VI}} \otimes$  CSS approximations are defined. As in the fixed-order calculation, both  $q\bar{q}$  and  $\gamma\gamma$  channels are taken into account on the same footing.

The original YFS scheme resums real and virtual soft-photon corrections to arbitrary scattering processes. The implementation in SHERPA [53] is specialised to correct decays of massive resonances, and for both cases relevant in this paper, i.e. for  $W$  and  $Z$  resonances, the resummation of soft logarithms is matched to exact  $\mathcal{O}(\alpha)$  corrections.<sup>2</sup> Its accuracy in charged- and neutral-current Drell-Yan processes has been validated in [54, 55]. As neither photon emissions off the initial states nor  $\gamma \rightarrow f\bar{f}$  splittings are included, it is worth noting that no  $\gamma q$  channels, occurring in the real emission correction of the full calculation, are accounted for.

The YFS implementation in SHERPA includes a generic resonance identification, ensuring that collective multipole radiation off the charged lepton ensemble preserves all resonance structures present in the event. To this end, first the final state of a scattering process is analysed, and possible resonances decaying into leptons and neutrinos are identified on the basis of event kinematics

<sup>2</sup> To be precise, the virtual corrections used neglect terms of  $\mathcal{O}(m_\ell^2/m_\nu^2)$  or higher, which are however negligible.

and existing vertices in the model. For the process studied in this paper,  $pp \rightarrow 2\ell 2\nu$ , multiple resonance structures are possible. They are disentangled on the basis of the distance measures<sup>3</sup>  $\Delta_Z = |m_{\ell\ell} - M_Z|/\Gamma_Z$  and  $\Delta_W = |m_{\ell\nu} - M_W|/\Gamma_W$ . In  $2\ell 2\nu$  production this leads to three distinct cases: (a) two pairs of leptons are identified to come from a specific resonance; (b) one pair of leptons is identified to come from a specific resonance, the other is classified as non-resonant; (c) all leptons are classified as non-resonant. Subsequently, identified resonant-production subprocesses are separated from the rest of the event, and the emerging decay is dressed with photon radiation respecting the Breit–Wigner distribution of the resonance, i.e. preserving the original virtuality of the off-shell lepton/neutrino system. Finally, all left-over non-resonantly produced leptons are grouped in a fictitious  $X \rightarrow n\ell + m\nu$  process, with suitably adjusted charges and masses for  $X$ . In this case, resummed real and virtual radiative QED corrections are applied in the soft limit only, including however hard collinear real-emission corrections through suitably subtracted Catani-Seymour dipole splitting functions [53].

In the CSSHOWER, the construction of the emitting dipoles follows the subtraction terms used in the fixed-order calculation. Owing to the unitary nature of all parton showers, dipoles whose splitting functions are negative, i.e. all dipoles formed by partons with like-sign electric charges, are inactive and do not contribute.<sup>4</sup> In the QCD case this corresponds to the leading-colour limit, and keeping  $C_F$  and  $C_A$  at their  $N_C = 3$  values guarantees a full-colour treatment of the collinear limit, while the soft-limit remains at  $N_C \rightarrow \infty$ . No such limit is meaningful in QED. Consequently, the absence of the like-signed dipoles has a degrading impact both on the description of the collinear and the soft limit. Moreover, the CSSHOWER has no knowledge of the internal resonance structure of the Born process. Thus, dipoles of charged particles spanning across one or multiple resonances will inevitably distort their line shape through their recoil assignments.<sup>5</sup> At the same time, however, all processes including photon radiation off the initial state quarks and  $\gamma \rightarrow f\bar{f}$  splittings are present. Thus, every channel occurring in the fixed-order calculation is described in its respective soft-collinear limits.

### 3.3 Input parameters, scale choices and variations

The input parameters for the NLO QCD+EW calculations of  $pp \rightarrow 2\ell 2\nu$  presented in Section 4 are summarised in Table 1. All unstable particles are treated in the complex-mass scheme [34], where width effects are absorbed into the complex-valued renormalised squared masses

$$\mu_i^2 = M_i^2 - i\Gamma_i M_i \quad \text{for } i = W, Z, H, t. \quad (3.2)$$

As top-quark and Higgs-boson contributions enter only at loop level, the dependence of our results on  $\Gamma_t$  and  $\Gamma_H$  is completely negligible. The CKM matrix is assumed to be diagonal. In fact, due to the negligible mixing of the first two and the third quark generations and because all quarks of the first two quark generations are taken to be massless, the unitarity of the CKM matrix ensures the independence of all physical results from the values of its matrix elements. The EW couplings are derived from the gauge-boson masses and the Fermi constant using

$$\alpha = \left| \frac{\sqrt{2} s_w^2 \mu_W^2 G_\mu}{\pi} \right|, \quad (3.3)$$

<sup>3</sup> We choose to identify a resonance only if  $\Delta_{Z,W} < \Delta_{\text{cut}} = 10$ . Thus, in the far off-shell regions no resonance is identified. We have checked that the results presented here are independent of  $\Delta_{\text{cut}}$  if it is chosen not too small, which would exclude higher-order corrections for a significant resonant phase-space region.

<sup>4</sup> Radiation from negative-valued splitting functions could in principle be taken into account using the algorithms of [52, 56], but are not implemented in the general shower.

<sup>5</sup> Comparing various resonance blind recoil schemes [57] and different evolution variables [58] we found similar effects for all observables discussed in Section 4.

$G_\mu = 1.1663787 \cdot 10^{-5} \text{ GeV}^2$	$\Gamma_W = 2.0897 \text{ GeV}$
$M_W = 80.385 \text{ GeV}$	$\Gamma_Z = 2.4955 \text{ GeV}$
$M_Z = 91.1876 \text{ GeV}$	$\Gamma_H = 4.07 \text{ MeV}$
$M_H = 125 \text{ GeV}$	$\Gamma_b = 0$
$m_b = 4.75 \text{ GeV}$	$\Gamma_t = 1.339 \text{ GeV}$
$m_t = 173.2 \text{ GeV}$	
$m_e = 511 \text{ keV}$	$m_\mu = 105 \text{ MeV}$
$\alpha(0) = 1/137.03599976$	

**Table 1.** Numerical values of all input parameters. The gauge boson masses are taken from [59], while their widths are obtained from state-of-the-art calculations. The Higgs mass and width are taken from [60]. The top quark mass is taken from [59] while its width has been calculated at NLO QCD. The electron and muon masses as well as the electromagnetic coupling in the Thomson limit,  $\alpha(0)$ , are only relevant for calculations involving YFS soft-photon resummation and the CSSHOWER.

where the  $W$ -boson mass and the squared sine of the mixing angle,

$$s_w^2 = 1 - c_w^2 = 1 - \frac{\mu_W^2}{\mu_Z^2}, \quad (3.4)$$

are complex-valued. The  $G_\mu$ -scheme guarantees an optimal description of pure SU(2) interactions at the EW scale. It is used for all channels, including photon-induced ones. In this respect, while it is well known that the coupling of final-state photons should be parametrised in terms of  $\alpha(0)$ , in Appendix A analysing the interplay between the counterterms associated with the renormalisation of  $\alpha$ , the photon wave function, and the  $\gamma$ PDF, we demonstrate that the coupling of initial-state photons cannot be parametrised in terms of  $\alpha(0)$ . Instead a high-energy definition of  $\alpha$ , for example in the  $\alpha(M_Z)$ - or the  $G_\mu$ -scheme, for the coupling of initial-state photons should be employed.

In all fixed-order results the renormalisation scale  $\mu_R$  and factorisation scale  $\mu_F$  are set to

$$\mu_{R,F} = \xi_{R,F} \mu_0, \quad \text{with} \quad \mu_0 = \frac{1}{2} H_T^{\text{lep}} \quad \text{and} \quad \frac{1}{2} \leq \xi_R, \xi_F \leq 2. \quad (3.5)$$

Therein,  $H_T^{\text{lep}}$  is the scalar sum of the transverse momenta of all charged final-state leptons plus the missing transverse momentum,

$$H_T^{\text{lep}} = \sum_{i \in \{\ell^\pm\}} p_{T,i} + \cancel{E}_T, \quad (3.6)$$

with  $\cancel{E}_T = |\vec{p}_{T,\nu} + \vec{p}_{T,\bar{\nu}}|$ . In order to guarantee infrared safety at NLO EW, the scale of (3.6) must be insensitive to collinear photon emissions off charged leptons. To this end, any charged leptons are dressed with collinear photons with  $\Delta R_{\ell\gamma} < 0.1$ . Our default scale choice corresponds to  $\xi_R = \xi_F = 1$ , and theoretical uncertainties are assessed by applying the scale variations  $(\xi_R, \xi_F) = (2, 2), (2, 1), (1, 2), (1, 1), (1, \frac{1}{2}), (\frac{1}{2}, 1), (\frac{1}{2}, \frac{1}{2})$ . For all considered processes at the inclusive level the difference with respect to a fixed scale choice  $\mu_0 = M_W$  is below 2% at NLO QCD, while inclusive NLO EW corrections agree at the level of one permille.

### 3.4 PDFs

For the calculation of hadron-level cross sections we employ the CT14qed parton distributions [22], which include NLO QCD and LO QED effects,<sup>6</sup> with the corresponding  $\alpha_S(M_Z) = 0.118$ . The NLO

<sup>6</sup> To be precise we use the CT14qed\_inc\_proton set interfaced through LHAPDF 6.1.6 [61].

PDF set is used for LO computations as well as for NLO QCD and NLO EW predictions. In order to assess the potentially large uncertainties stemming from photon-induced processes, two alternative sets based on different determinations of the photon PDF are considered, namely the recently calculated LUXqed PDFs [23] and the data driven fit of NNPDF3.0qed [21, 62]. Specifically, we replace the photon PDF of the default set by the alternative parametrisations, while using CT14qed quark and gluon PDFs throughout. This is justified by the negligible dependence of the quark and gluon densities on the  $\gamma$ PDF.

The three considered sets implement different treatments of the photon PDF. The CT14qed PDFs assume as initial condition for the  $\gamma$ PDF at  $Q_0 = 1.295$  GeV an inelastic contribution that results from the convolution of primordial quark distributions with QED splitting functions. This ansatz involves a free normalisation parameter, which is traded for the inelastic photon momentum fraction,  $p_0^\gamma = \int_0^1 dx x \gamma(x, Q_0)$ , and fitted to DIS data with isolated photons. For our default predictions we use a CT14qed set corresponding to the best fit value,  $p_0^\gamma = 0.05\%$ . The inelastic component, which describes processes where the proton breaks, is complemented by an elastic component, corresponding to the case where the proton remains intact. The latter is determined at the scale  $Q_0$  using the equivalent photon approximation (EPA) [63]. The sum of inelastic and elastic contributions at  $Q_0$  is evolved as a single photon density<sup>7</sup> through coupled DGLAP equations for photons, quarks and gluons at NLO QCD + LO QED.

In the LUXqed approach, the usual description of  $ep \rightarrow e + X$  data, where a virtual photon radiated from the electron beam probes quarks inside the proton via  $\gamma^*q$  scattering, is related to an alternative interpretation, where the lepton beam probes the photon content of the proton via  $\ell\gamma$  scattering. In this way, the photon density can be derived from proton structure functions in a model-independent way, and building on available global fits of QCD PDFs, parametrisations of  $ep$  data at low  $Q^2$ , and elastic contributions, one arrives at an accurate determination of the  $\gamma$ PDF. Then, starting at  $Q_0 = 10$  GeV, the photon density is evolved with all other QCD partons through DGLAP equations including QED corrections up to  $\mathcal{O}(\alpha_S\alpha)$ .

The NNPDF3.0qed photon PDF is based on a much more general multiparameter neural-network parametrisation, which can naturally account for both the elastic and inelastic components. Thus the NNPDF3.0qed photon density is much more receptive to the poor sensitivity of current data to photon-induced processes. This leads to much larger admissible photon densities combined with much bigger uncertainties as compared to the other PDF sets. The resulting photon density is evolved at NLO QCD + LO QED.

In order to avoid undesired contaminations from single-top contributions of type  $pp \rightarrow Wt \rightarrow WWb \rightarrow 2\ell 2\nu$  in the NLO QCD and NLO EW corrections, in our calculations we apply a full veto against final-state  $b$ -quarks. Since such a veto would jeopardize IR cancellations for  $m_b = 0$ , we consider the  $b$ -quark to be massive, i.e. we assume the presence of only four light flavours. In order to reconcile this choice with the fact that the employed PDFs involve five active flavours, an appropriate PDF-scheme conversion [66] is applied. As discussed in Appendix B, this transformation is almost trivial for the process at hand. At LO,  $pp \rightarrow 2\ell 2\nu$  comprises neither gluon channels nor  $\alpha_S$  terms. Thus, only the  $\gamma\gamma$  channel requires a correction related to the scheme dependence of the  $\gamma$ PDF. Taking this into account, we can safely perform our calculations using five-flavour PDFs,

---

<sup>7</sup> Note that, in contrast to “inelastic photons”, which are inherently off-shell, “elastic” photons as obtained from the EPA at  $Q_0^2$  are exactly on-shell, even when they enter hard-scattering processes at  $Q^2 \gg m_p^2$ . Nevertheless, also elastic photons can undergo  $\gamma \rightarrow q\bar{q}$  splittings at arbitrary  $Q^2$ . Thus, elastic and inelastic photons contribute to the PDF evolution towards high  $Q^2$  on the same footing. In practice, the photon PDF at high- $Q^2$  receives contributions from the elastic and inelastic  $\gamma$ PDF at  $Q_0^2$ , both decreased due to  $\gamma \rightarrow q\bar{q}$  splittings, and positive contributions from (anti)quark distributions via  $q \rightarrow \gamma q$  splittings. It turns out that, due to the much larger quark density, the latter contributions dominate by far. Thus, the details of the evolution of the elastic and inelastic  $\gamma$ PDFs play only a marginal role [64, 65].

omitting initial- and final-state  $b$ -quarks, and using  $m_b > 0$  in the loops. Up to terms beyond NLO QCD+EW, this approach is perfectly consistent with a conventional calculation in the 4F scheme.

## 4 Results

In this section we present numerical predictions for the DF and SF processes,  $pp \rightarrow e^+ \mu^- \nu_e \bar{\nu}_\mu$  and  $pp \rightarrow e^+ e^- \nu \bar{\nu}$ , at  $\sqrt{s} = 13$  TeV. The impact of NLO corrections is illustrated by comparing against LO predictions, which include  $q\bar{q}$  and  $\gamma\gamma$ -induced processes at  $\mathcal{O}(\alpha^4)$ . For the combination of QCD and EW higher-order effects we consider both an additive and a multiplicative approach, defined, respectively, as

$$d\sigma_{\text{NLO QCD+EW}} = d\sigma_{\text{LO}} (1 + \delta_{\text{QCD}} + \delta_{\text{EW}}) \quad (4.1)$$

and

$$d\sigma_{\text{NLO QCD}\times\text{EW}} = d\sigma_{\text{LO}} (1 + \delta_{\text{QCD}}) (1 + \delta_{\text{EW}}) . \quad (4.2)$$

Therein, the relative QCD and EW corrections are defined as

$$\delta_{\text{QCD}} = \frac{d\sigma_{(1,4)}}{d\sigma_{(0,4)}} \quad \text{and} \quad \delta_{\text{EW}} = \frac{d\sigma_{(0,5)}}{d\sigma_{(0,4)}} , \quad (4.3)$$

where the  $d\sigma_{(i,j)}$  are the cross section contributions of  $\mathcal{O}(\alpha_S^i \alpha^j)$ , thus  $d\sigma_{(0,4)} \equiv d\sigma_{\text{LO}}$ . In order to illustrate the interplay of the various partonic channels in the multiplicative QCD $\times$ EW combination, we write each  $d\sigma_{(i,j)}$  as a sum over contributions  $d\sigma_{(i,j)}^{ab}$  where  $a$  and  $b$  are the proton constituents initiating the subprocess at the given order. At LO, for the decomposition into  $q\bar{q}$  and  $\gamma\gamma$  channels and their relative weights we write

$$d\sigma_{\text{LO}} = d\sigma_{(0,4)}^{q\bar{q}} + d\sigma_{(0,4)}^{\gamma\gamma} \quad (4.4)$$

and

$$\epsilon_{q\bar{q}} = \frac{d\sigma_{(0,4)}^{q\bar{q}}}{d\sigma_{(0,4)}^{q\bar{q}} + d\sigma_{(0,4)}^{\gamma\gamma}} , \quad \epsilon_{\gamma\gamma} = 1 - \epsilon_{q\bar{q}} = \frac{d\sigma_{(0,4)}^{\gamma\gamma}}{d\sigma_{(0,4)}^{q\bar{q}} + d\sigma_{(0,4)}^{\gamma\gamma}} . \quad (4.5)$$

At NLO, the QCD correction factor in (4.3) corresponds to

$$\delta_{\text{QCD}} = \frac{d\sigma_{(1,4)}^{q\bar{q}} + d\sigma_{(1,4)}^{gq/g\bar{q}}}{d\sigma_{(0,4)}^{q\bar{q}} + d\sigma_{(0,4)}^{\gamma\gamma}} = \epsilon_{q\bar{q}} \delta_{\text{QCD}}^{q\bar{q}} , \quad (4.6)$$

where the relative correction

$$\delta_{\text{QCD}}^{q\bar{q}} = \frac{d\sigma_{(1,4)}^{q\bar{q}} + d\sigma_{(1,4)}^{gq/g\bar{q}}}{d\sigma_{(0,4)}^{q\bar{q}}} \quad (4.7)$$

is restricted to the  $q\bar{q}$  channel. Finally, for the EW correction in (4.3) we have

$$\delta_{\text{EW}} = \frac{d\sigma_{(0,5)}^{q\bar{q}} + d\sigma_{(0,5)}^{\gamma q/\gamma\bar{q}} + d\sigma_{(0,5)}^{\gamma\gamma}}{d\sigma_{(0,4)}^{q\bar{q}} + d\sigma_{(0,4)}^{\gamma\gamma}} = \delta_{\text{EW}}^{q\bar{q}/\gamma\gamma} . \quad (4.8)$$

Here, since the newly emerging  $\gamma q$  and  $\gamma\bar{q}$  channels act as real emission corrections to both the LO  $q\bar{q}$  and  $\gamma\gamma$  channels, it is not possible to unambiguously split the full EW correction into two parts associated with the  $q\bar{q}$  and  $\gamma\gamma$  channels.<sup>8</sup> Therefore, our definition of  $\delta_{\text{EW}}$  amounts to choosing not

<sup>8</sup> The situation is analogous to the case of  $t\bar{t}$  production at NLO QCD. At leading order a distinction can be made between the  $q\bar{q}$ - and  $gg$ -induced channels. At NLO QCD, the emerging  $qg$ - and  $\bar{q}g$ -induced channels act as real corrections to both and therefore link both LO processes. An unambiguous assignment of the  $qg$ - and  $\bar{q}g$ -induced NLO corrections to the  $q\bar{q}$  and  $gg$  LO channels is thus not possible.

to assign arbitrary fractions of the  $\gamma q$ - and  $\gamma\bar{q}$ -corrections to act as corrections to the LO  $q\bar{q}$  and  $\gamma\gamma$  channels, but to define an overall NLO EW correction factor.

With the above definitions the multiplicative combination (4.2) can be cast in the form

$$\begin{aligned} d\sigma_{\text{NLO QCD}\times\text{EW}} &= d\sigma_{\text{LO}} (1 + \delta_{\text{QCD}}) (1 + \delta_{\text{EW}}) \\ &= \left[ d\sigma_{(0,4)}^{q\bar{q}} \left( 1 + \delta_{\text{QCD}}^{q\bar{q}} \right) + d\sigma_{(0,4)}^{\gamma\gamma} \right] \left( 1 + \delta_{\text{EW}}^{q\bar{q}/\gamma\gamma} \right), \end{aligned} \quad (4.9)$$

where the relative weight of QCD corrections in the different partonic channels is manifestly respected. In particular, the  $\gamma\gamma$  channel remains free of QCD correction effects, consistent with its behaviour at NLO QCD.

Alternatively, as is often done in the literature, one may choose to regard the combination of the  $\gamma q$ - and  $\gamma\bar{q}$ -induced NLO EW effects as a correction to the  $q\bar{q}$  channel, and to attribute the remnant NLO EW corrections to the  $\gamma\gamma$  channel. With this *ad hoc* splitting,

$$\delta_{\text{EW}}^{q\bar{q}} = \frac{d\sigma_{(0,5)}^{q\bar{q}} + d\sigma_{(0,5)}^{\gamma q/\gamma\bar{q}}}{d\sigma_{(0,4)}^{q\bar{q}}}, \quad \delta_{\text{EW}}^{\gamma\gamma} = \frac{d\sigma_{(0,5)}^{\gamma\gamma}}{d\sigma_{(0,4)}^{\gamma\gamma}}, \quad (4.10)$$

it is natural to adopt a channel-by-channel factorisation of EW and QCD corrections,

$$d\sigma_{\text{NLO QCD}\otimes\text{EW}} = d\sigma_{(0,4)}^{q\bar{q}} \left( 1 + \delta_{\text{QCD}}^{q\bar{q}} \right) \left( 1 + \delta_{\text{EW}}^{q\bar{q}} \right) + d\sigma_{(0,4)}^{\gamma\gamma} \left( 1 + \delta_{\text{EW}}^{\gamma\gamma} \right). \quad (4.11)$$

While one may debate if (4.2) is more or less motivated than (4.11), we observe that, using

$$\delta_{\text{EW}} = \epsilon_{q\bar{q}} \delta_{\text{EW}}^{q\bar{q}} + \epsilon_{\gamma\gamma} \delta_{\text{EW}}^{\gamma\gamma}, \quad (4.12)$$

the difference between the two prescriptions can be cast in the form

$$d\sigma_{\text{NLO QCD}\times\text{EW}} - d\sigma_{\text{NLO QCD}\otimes\text{EW}} = d\sigma_{\text{LO}} \epsilon_{q\bar{q}} \epsilon_{\gamma\gamma} \delta_{\text{QCD}}^{q\bar{q}} \left( \delta_{\text{EW}}^{\gamma\gamma} - \delta_{\text{EW}}^{q\bar{q}} \right). \quad (4.13)$$

This indicates that the two prescriptions tend to coincide if either one LO channel dominates, the QCD correction is small, or both channels' EW corrections are of the same size. In large regions of the phase space these conditions are simultaneously satisfied, and for all observables studied in the following the scheme dependence (4.13) is found to be smaller than 5%, in most cases even below 0.5%, of the LO cross section. Both the size of the EW corrections contributed by the three individual channels and the above scheme dependence are detailed in Appendix C.

In the multiplicative approach, which we deem our best prediction, the uncertainties are estimated by scaling the NLO QCD predictions with the relative NLO EW correction,

$$1 + \delta_{\text{EW}}(\mu_{\text{R}}, \mu_{\text{F}}) = \frac{d\sigma_{\text{NLO EW}}(\mu_{\text{R}}, \mu_{\text{F}})}{d\sigma_{\text{LO}}(\mu_{\text{R}}, \mu_{\text{F}})}, \quad (4.14)$$

evaluated at the central scale. This is justified by the fact that  $\delta_{\text{EW}}(\mu_{\text{R}}, \mu_{\text{F}})$  is independent of  $\mu_{\text{R}}$  and involves only a very weak  $\mu_{\text{F}}$  dependence of  $\mathcal{O}(\alpha)$ , while the LO QCD  $\mu_{\text{F}}$ -dependence cancels out in the ratio.

As discussed in Section 2.1, we include photon-induced contributions throughout, including  $\gamma\gamma \rightarrow 2\ell 2\nu$ ,  $\gamma\gamma \rightarrow 2\ell 2\nu\gamma$  and  $\gamma q \rightarrow 2\ell 2\nu q$  channels at NLO EW. To assess the uncertainty arising from the choice of photon PDF we vary their parametrisation from their default (CT14qed) to that of LUXqed and NNPDF3.0qed, while keeping the quark and gluon PDFs fixed, cf. Section 3.4. The overall impact of photon-induced processes is illustrated by switching off the photon PDF, both at LO and NLO EW.

Additionally, as discussed in Section 3.2, we investigate to which degree exact NLO QCD $\times$ EW results can be reproduced by approximations based on the combination of IR-subtracted virtual

Inclusive cuts	
$\cancel{E}_T$	$> 20 \text{ GeV}$
$p_{T,\ell^\pm}$	$> 20 \text{ GeV}$
$ \eta_{\ell^\pm} $	$< 2.5$
$\Delta R_{\ell^+\ell^-}$	$> 0.2$
$H_T^{\text{jet}}$	$< 0.2 H_T^{\text{lep}}$

**Table 2.** Inclusive selection cuts for off-shell vector-boson pair production in the  $2\ell 2\nu$  channel. The missing transverse momentum  $\cancel{E}_T$  is calculated from the vector sum of neutrino momenta.

EW corrections ( $\text{EW}_{\text{VI}}$ ) with YFS QED resummation or, alternatively, with the CSSHOWER. Such approximation, denoted as  $\text{NLO QCD} \times \text{EW}_{\text{VI}} \otimes \text{YFS}$  and  $\text{NLO QCD} \times \text{EW}_{\text{VI}} \otimes \text{CSS}$ , can be realised in realistic particle-level simulations using currently public tools, and can be regarded as a first step towards NLO QCD+EW matching and merging.

In the following, we study various fiducial cross sections and differential distributions. Physical observables involving charged leptons are known to be highly sensitive to QED radiative corrections. This should be avoided by using dressed leptons. To this end we recombine all leptons with nearly collinear photons that lie within a cone

$$\Delta R_{\ell\gamma} = \sqrt{\Delta\phi_{\ell\gamma}^2 + \Delta\eta_{\ell\gamma}^2} < R_{\text{rec}} = 0.1. \quad (4.15)$$

This dressing procedure captures the bulk of the collinear final-state radiation, while keeping contamination from large-angle photon radiation at a negligible level.

In our analysis we apply a set of acceptance cuts, as listed in Table 2, on the transverse momentum, pseudo-rapidity and angular separation of the dressed charged leptons and on the missing transverse momentum calculated based on the neutrino momenta,  $\cancel{E}_T = p_{T,\nu\bar{\nu}}$ .

Inclusive vector-boson pair production receives large NLO QCD corrections in kinematic regions where one of the vector bosons might become soft. This effect is a variant of the well known ‘giant  $K$ -factors’ [67]. In order to suppress these large QCD corrections that spoil the perturbative convergence we veto events with

$$H_T^{\text{jet}} > 0.2 H_T^{\text{lep}}, \quad (4.16)$$

where  $H_T^{\text{jet}} = \sum_{i \in \text{jets}} p_{T,i}$  based on anti- $k_T$  jets with  $R = 0.4$  and  $p_T > 30 \text{ GeV}$ . In practice,  $H_T^{\text{jet}} = p_{T,j}$  at NLO QCD. A reliable inclusive prediction without such a jet veto requires the merging of  $pp \rightarrow 2\ell 2\nu + 0, 1 \text{ jets}$  at NLO QCD+EW, but goes beyond the scope of the present paper. The complete analysis has been implemented in RIVET [68]. For reference, we present the cross sections of the inclusive as well as three more exclusive event selections for both channels in Appendix D.

#### 4.1 The different-flavour channel $pp \rightarrow e^+ \mu^- \nu_e \bar{\nu}_\mu$

Differential distributions for  $pp \rightarrow e^+ \mu^- \nu_e \bar{\nu}_\mu$  are presented in Figs. 9–15. In every figure, the left plot shows absolute predictions as well as relative NLO corrections with scale-variation bands. The upper-right ratio plot quantifies the importance of photon-induced contributions as well as the effect of using different  $\gamma$ PDFs, while the lower-right ratio plot compares exact NLO results against the  $\text{NLO QCD} \times \text{EW}_{\text{VI}} \otimes \text{YFS}$  and  $\text{NLO QCD} \times \text{EW}_{\text{VI}} \otimes \text{CSS}$  approximations. For reference, we also show the pure fixed-order NLO QCD  $\times$  EW<sub>VI</sub> approximation, which includes only the IR-subtracted part of virtual EW corrections and lacks any differential description of QED real corrections.

In Figs. 9–12 we present distributions in the transverse momenta of the leading and subleading leptons,  $p_{T,\ell_1}$  and  $p_{T,\ell_2}$ , the total missing transverse momentum,  $\cancel{E}_T$ , and the invariant mass of



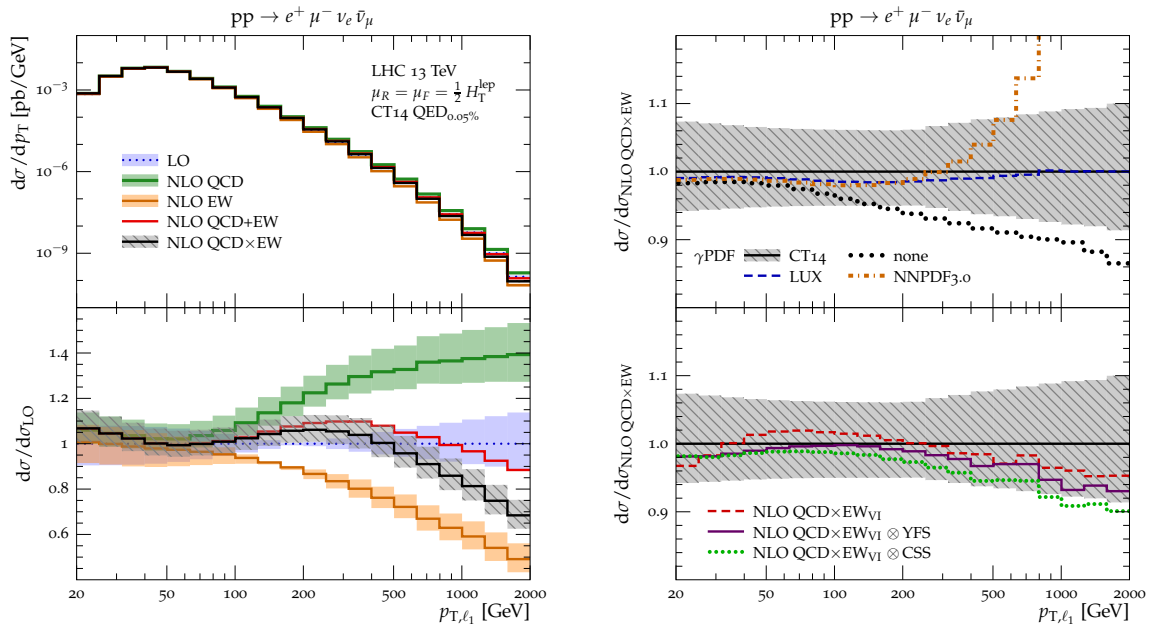


**Figure 9.** Distribution in the transverse momentum of the leading lepton,  $p_{T,\ell_1}$ , for  $pp \rightarrow e^+ \mu^- \nu_e \bar{\nu}_\mu$  at 13 TeV. The left panel shows the absolute predictions and relative corrections with respect to LO (including  $\gamma\gamma \rightarrow 2\ell 2\nu$ ) for the nominal CT14qed PDF. The bands correspond to factor-two scale variations. The upper-right panel shows the effect, at NLO QCD $\times$ EW level, of switching off  $\gamma$ -induced contributions or applying different photon densities from different current PDFs, while using quark and gluon densities from the nominal CT14qed set throughout. The lower-right ratio shows the level of agreement of the NLO QCD $\times$ EW $_{VI}$ , NLO QCD $\times$ EW $_{VI} \otimes$  YFS and NLO QCD $\times$ EW $_{VI} \otimes$  CSS approximations with the exact NLO QCD $\times$ EW calculation.

the  $e^+ \mu^-$  pair,  $m_{\ell\ell}$ . The leading and subleading lepton are defined by their ordering in transverse momentum, irrespective of their charge. EW corrections to these observables feature the typical Sudakov behaviour, with small effects below 100 GeV and large negative corrections at the TeV scale. In the tails of the lepton- $p_T$  and  $m_{\ell\ell}$  distributions NLO EW corrections can reach and even largely exceed  $-50\%$ . The dominant effects originate from  $q\bar{q} \rightarrow W^+W^-$  topologies with resonant  $W$  bosons, and the strong enhancement of EW Sudakov corrections is induced by the high  $p_T$  and the large SU(2) charges of the  $W$  bosons. In the presence of EW corrections of several tens of percent, fixed-order NLO predictions should be supplemented by a resummation of Sudakov logarithms. As a rough indication of the possible magnitude of higher-order EW effects, we observe that naïve exponentiation can turn NLO EW corrections of  $-50$ – $80\%$  into an overall all-order EW correction of  $-40$ – $55\%$ . We also note that EW corrections of this magnitude appear in a kinematic range that cannot be probed with decent statistics at the LHC. Nevertheless, such phase-space regions would play an important role at a 100 TeV  $pp$  collider [69].

Due to the presence of the jet veto (4.16), the impact of QCD corrections in Figs. 9–12 is rather mild at energies below  $M_W$ , and grows only up to  $+10$ – $40\%$  in the tails. While the actual size of QCD  $K$ -factors depends on the scale choice, we recall that, in general, QCD corrections to  $pp \rightarrow e^+ \mu^- \nu_e \bar{\nu}_\mu$  receive sizeable real-emission contributions in the absence of jet vetoes [2]. Scale uncertainties at NLO QCD are rather constant and somewhat below 10%.

Due to their opposite sign, QCD and EW corrections cancel against each other to a certain extent. At the same time, in regions where both QCD and EW corrections are well beyond 10%,

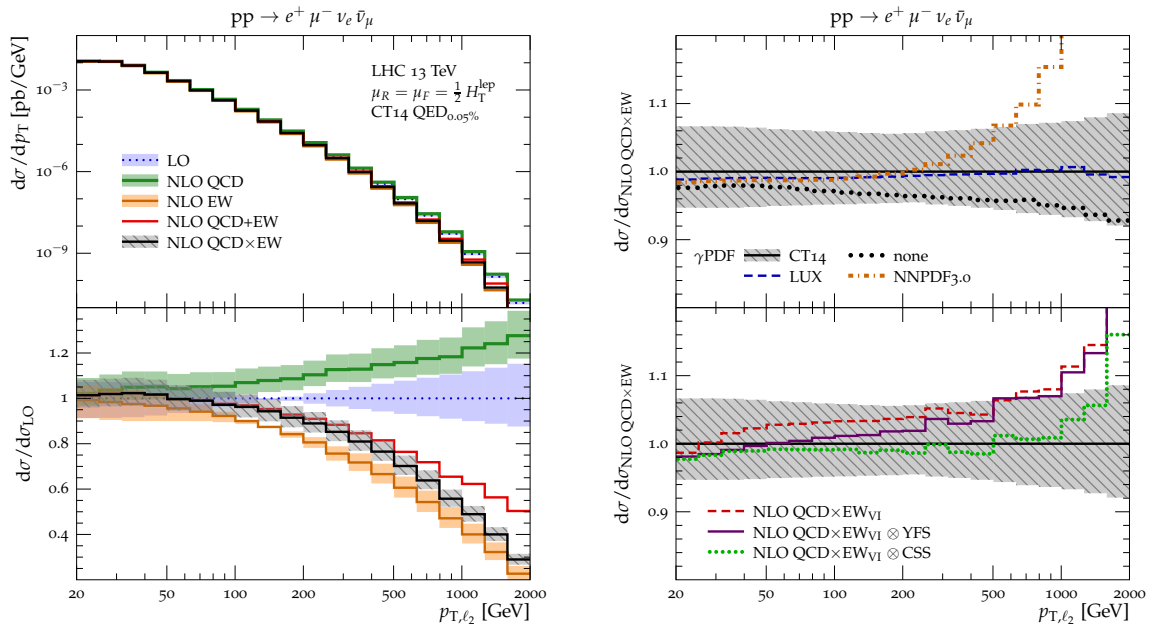


**Figure 10.** Distribution in the transverse momentum of the subleading lepton,  $p_{T,\ell_2}$ , for  $pp \rightarrow e^+ \mu^- \nu_e \bar{\nu}_\mu$  at 13 TeV. Details as in Fig. 9.

contributions of relative  $\mathcal{O}(\alpha_S \alpha)$  become relevant. Such NNLO QCD $\times$ EW effects are estimated in our predictions by means of the multiplicative combination of NLO corrections (4.2), which is well justified if EW corrections are dominated by Sudakov logarithms and QCD radiation is softer than the characteristic scale of the  $q\bar{q} \rightarrow 2\ell 2\nu$  EW subprocess. Comparing the additive and multiplicative combination of QCD and EW corrections in Figs. 9–12, we find that contributions of relative  $\mathcal{O}(\alpha_S \alpha)$  can exceed 10% in the tails. Among the virtues of a multiplicative combination of QCD and EW corrections, it is worth pointing out that NLO EW corrections are implicitly supplemented by QCD radiation, resulting, for instance, in a reasonable behaviour with respect to possible jet vetoes. At the same time, it should be stressed that, for a more reliable assessment of  $\mathcal{O}(\alpha_S)$  corrections, an approach like NLO QCD+EW merging [24] is certainly preferable.

The behaviour of the  $\cancel{E}_T$  distribution (Fig. 11) deserves a few additional comments. First, in the tail of this distribution we observe that Sudakov EW effects are less pronounced than in other observables. This is due to the fact that requiring a high- $p_T$   $\nu_e \bar{\nu}_\mu$  pair forces the  $W$  bosons into the off-shell regime. As a result, Sudakov logarithms arise only from EW interactions between the on-shell final-state leptons and, like in Drell-Yan processes, they turn out to be less enhanced than in  $pp \rightarrow W^+ W^-$ . Second, the QCD  $K$ -factor features a sizeable enhancement characterised by a rather sharp threshold at  $\cancel{E}_T \sim M_W$ . This is related to the fact that, in  $pp \rightarrow W^+ W^-$  at LO,  $p_{T,W^+W^-} = 0$  strongly disfavours the production of a  $\nu_e \bar{\nu}_\mu$  pair with  $p_T > M_W$ . Therefore, the  $W^+ W^-$  transverse momentum induced by NLO QCD radiation results in a sizeable enhancement in the  $\cancel{E}_T > M_W$  region (see [2]).

Photon-induced contributions in Figs. 9–12 can reach up to 5–20%, depending on the observable. The largest effects are typically observed in the TeV tails. The  $\gamma$ -induced contributions to the  $\cancel{E}_T$  distribution, however, approach 10% already at 200 GeV, an effect that can already be observed at LO. This is due to the presence of non-resonant diagrams that are absent in the  $q\bar{q}$  channels. They can populate this phase-space region, which is disfavoured as soon as the neutrinos need to

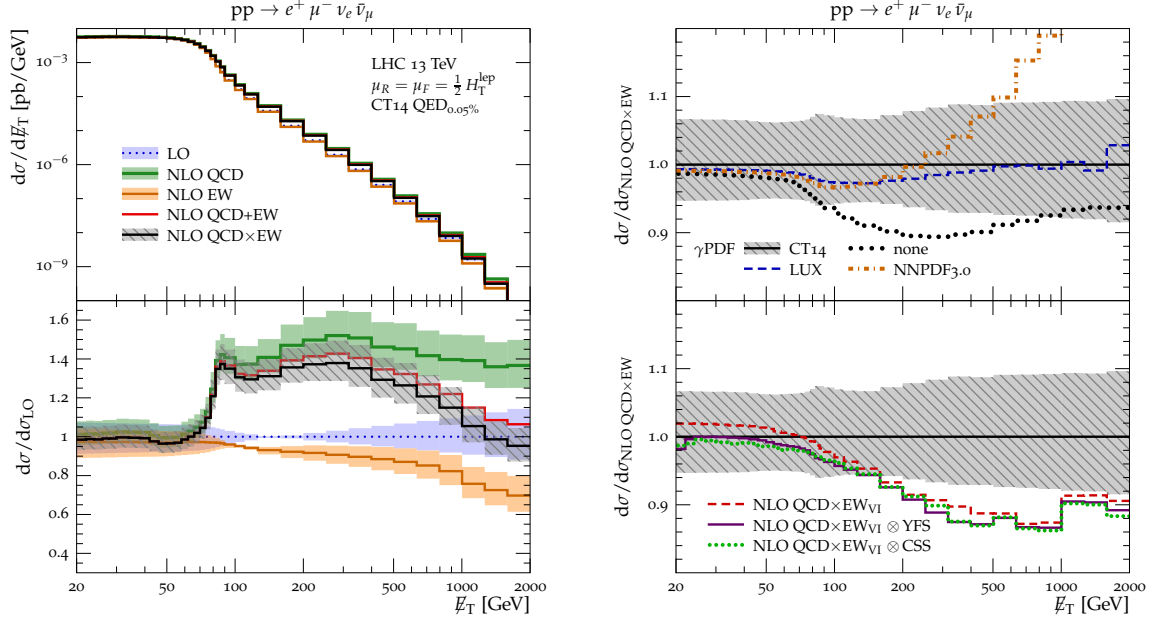


**Figure 11.** Distribution of the missing transverse momentum,  $\cancel{E}_T$ , for  $pp \rightarrow e^+ \mu^- \nu_e \bar{\nu}_\mu$  at 13 TeV. Details as in Fig. 9.

be produced through an  $s$ -channel  $W$  propagator. This effect is further increased by real-emission channels of type  $\gamma q \rightarrow 2\ell 2\nu q$ , which are strongly enhanced at  $\cancel{E}_T \geq M_W$ , similarly as for QCD radiative effects.

Comparing different photon PDFs, for all observables we find a fairly good agreement between CT14qed and LUXqed  $\gamma$ PDFs, with differences that never exceed the level of five percent. Conversely, the usage of the NNPDF3.0qed  $\gamma$ PDF yields similar inclusive cross sections as CT14qed and LUXqed, but much bigger  $\gamma$ -induced contributions in the tails. Nevertheless the differences are consistent with the large uncertainty of the photon density in NNPDF3.0qed, while using the other PDF sets leads to a  $\gamma$ PDF uncertainty well below the overall QCD scale uncertainty. The largest  $\gamma$ -induced effects are observed in the tail of the  $m_{\ell\ell}$  distribution, where the dominant contribution originates from  $\gamma\gamma \rightarrow W^+W^-$  topologies with  $t$ -channel poles in the forward/backward regions. We note that relaxing rapidity cuts on charged leptons, which act as a cut-off on  $t$ -channel poles, would further enhance  $\gamma\gamma \rightarrow W^+W^-$  contributions.

Comparing the NLO QCD $\times$ EW $_{\text{VI}} \otimes$  YFS and NLO QCD $\times$ EW $_{\text{VI}} \otimes$  CSS approximations against exact NLO QCD $\times$ EW results, in Figs. 9–12 we observe agreement at the few-percent level for  $p_{T,\ell_1}$  and  $m_{\ell\ell}$ , while in the tails of the  $p_{T,\ell_2}$  and  $\cancel{E}_T$  distributions the error of the NLO QCD $\times$ EW $_{\text{VI}} \otimes$  YFS approximation can exceed 10%. This can be attributed to the fact that the YFS resummation as implemented in SHERPA does not account for initial-state QED radiation in the  $q\bar{q}$  channels and neglects the  $\gamma q$  channels. The CSSHOWER, on the other hand, describes these configurations, but lacks accuracy due to its dipole structure. In any case, both approximations improve the pure fixed-order approximation of NLO QCD $\times$ EW $_{\text{VI}}$ .

Figs. 13–14 illustrate distributions in the  $W$ -boson mass,  $m_{\ell\nu}$ , and in the  $W^+W^-$  invariant mass,  $m_{\ell\ell\nu\nu}$ . Such observables are not experimentally accessible, but they provide valuable insights into the resonance structure of  $pp \rightarrow e^+ \mu^- \nu_e \bar{\nu}_\mu$  and into the behaviour of EW corrections. Focussing on the  $m_{\ell\nu}$  and  $m_{\ell\ell\nu\nu}$  regions of the  $W \rightarrow \ell\nu$  and  $Z \rightarrow 2\ell 2\nu$  peaks and the  $W^+W^- \rightarrow \ell\ell\nu\nu$

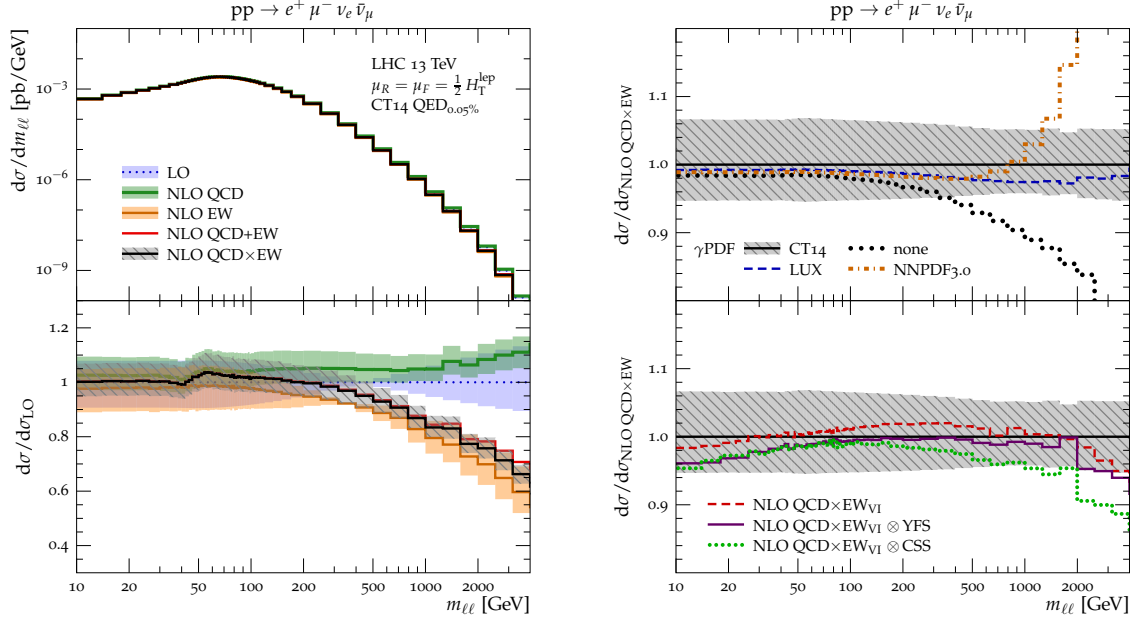
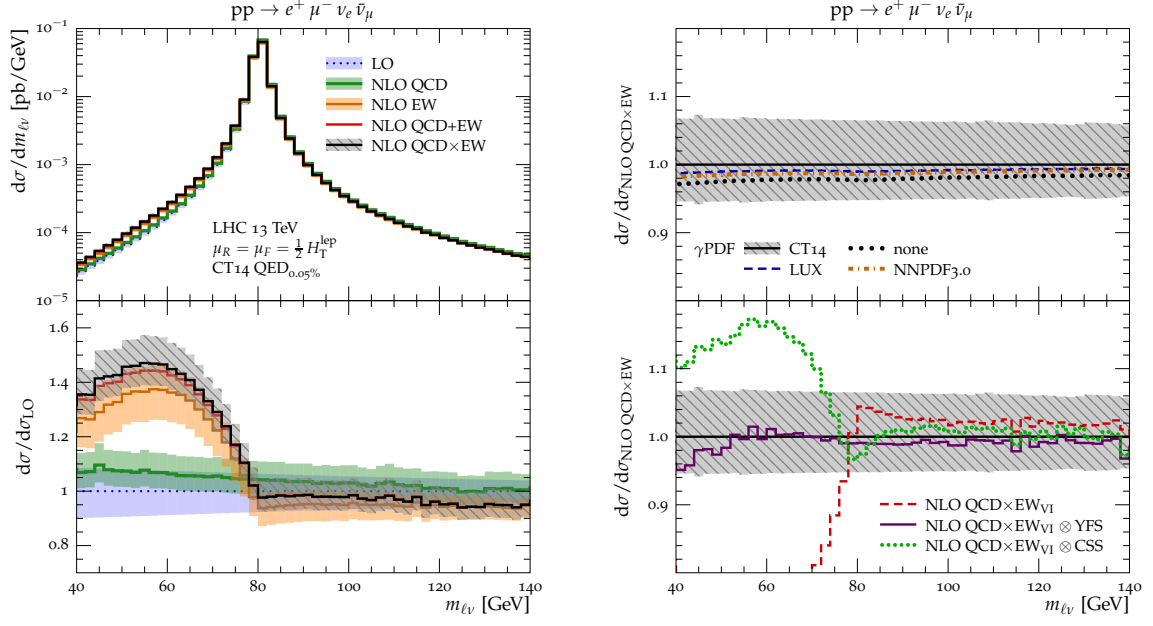


**Figure 12.** Distribution in the invariant mass of the  $e^+ \mu^-$  pair,  $m_{\ell\ell}$ , for  $pp \rightarrow e^+ \mu^- \nu_e \bar{\nu}_\mu$  at 13 TeV. Details as in Fig. 9.

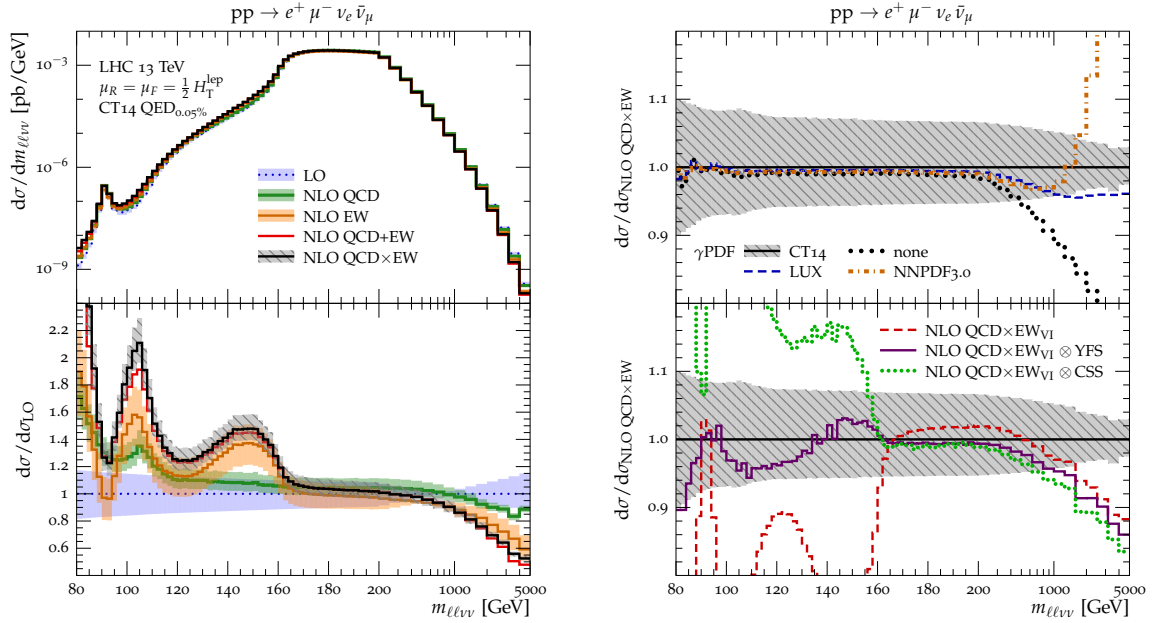
threshold, we observe that QCD corrections are almost insensitive to the presence of EW resonances and thresholds. Photon-induced contributions are on the level of 1–3%, while EW corrections feature sizeable shape distortions due to  $\gamma$  bremsstrahlung off the charged leptons. Such shape corrections can be understood as a net migration of events from the peak and threshold regions towards the low-mass tails and, in the case of the  $m_{\ell\nu\nu}$  distribution, towards the local minimum above the  $Z \rightarrow \ell\nu\nu$  peak. In these observables, apart from the region of very high  $m_{\ell\nu\nu}$ , the NLO QCD $\times$ EW $_{\text{VI}}$   $\otimes$  YFS approximation is found to reproduce exact results with fairly good accuracy. In particular, in the off-shell regime, i.e. for  $m_{\ell\nu} < M_W$  or  $m_{\ell\nu\nu} < 2M_W$ , the offset between NLO QCD $\times$ EW $_{\text{VI}}$  approximation and exact results indicates the presence of QED radiation effects beyond 10%, which turn out to be well described by the YFS approach. The remaining differences are below 5% or so. They can be attributed to higher-order corrections, missing in the fixed-order calculations, and to ambiguities related to the YFS resummation for highly off-shell decays. In contrast, QED radiative corrections to  $m_{\ell\nu}$  and  $m_{\ell\nu\nu}$  are strongly overestimated in the NLO QCD $\times$ EW $_{\text{VI}}$   $\otimes$  CSS approach. This is most likely due to the fact that the CSSHOWER is unaware of resonance structures.

Fig. 14 also displays the multi-TeV region of the  $m_{\ell\nu\nu}$  distribution, where large negative EW Sudakov corrections are observed, as well as  $\gamma$ -induced contributions beyond 10%, with large deviations between the different  $\gamma$ PDF sets. At the same time the NLO QCD $\times$ EW $_{\text{VI}}$   $\otimes$  YFS and NLO QCD $\times$ EW $_{\text{VI}}$   $\otimes$  CSS predictions grow gradually worse when compared with the exact NLO QCD $\times$ EW calculation due, respectively, to the missing or limited accuracy in the description of  $\gamma \rightarrow q\bar{q}$ -splittings in the initial state.

Finally, in Fig. 15 we show the distribution in the azimuthal separation of the  $e^+ \mu^-$  pair,  $\Delta\phi_{\ell\ell}$ . For this observable, EW corrections and  $\gamma$ -induced effects are almost flat and similarly small as for the integrated cross section. As for QCD corrections, we observe a pronounced kinematic dependence for  $\Delta\phi_{\ell\ell} \rightarrow \pi$ . This can be understood as a statistical effect related to the migration of events from highly populated to poorly populated bins.



**Figure 13.** Distribution in the invariant mass of the matching lepton-neutrino pair,  $m_{l\nu}$ , for  $pp \rightarrow e^+ \mu^- \nu_e \bar{\nu}_\mu$  at 13 TeV. Details as in Fig. 9.



**Figure 14.** Distribution in the invariant mass of all four final state leptons and neutrinos,  $m_{\ell\nu\nu}$ , for  $pp \rightarrow e^+ \mu^- \nu_e \bar{\nu}_\mu$  at 13 TeV. Details as in Fig. 9.

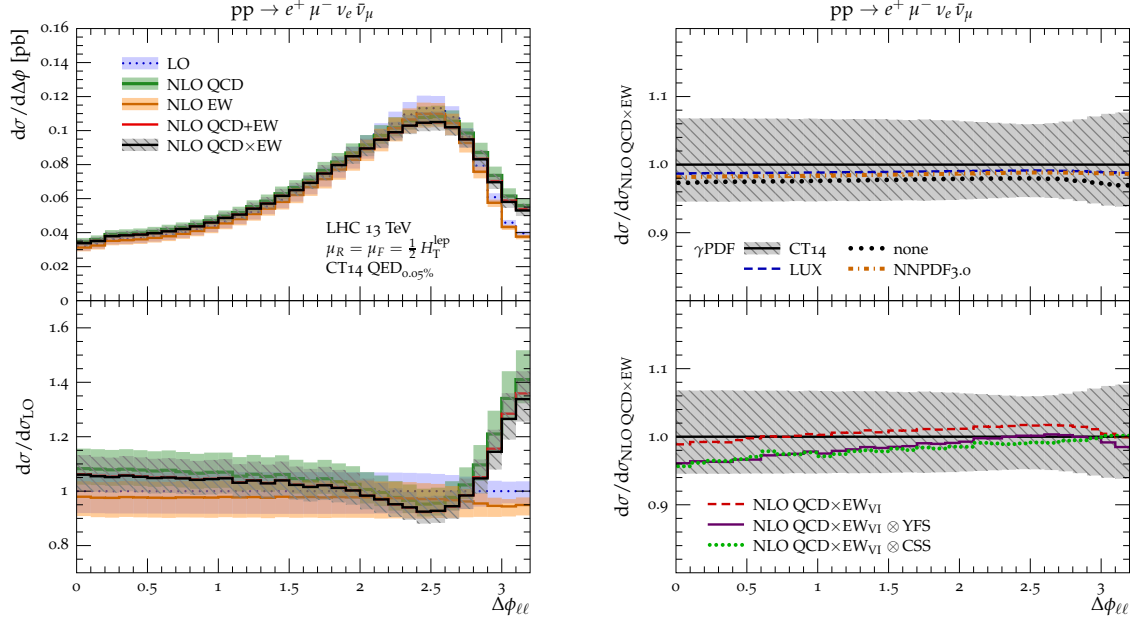


**Figure 15.** Distribution in the azimuthal separation of the  $e^+ \mu^-$  pair,  $\Delta\phi_{\ell\ell}$ , for  $pp \rightarrow e^+ \mu^- \nu_e \bar{\nu}_\mu$  at 13 TeV. Details as in Fig. 9.

#### 4.2 The same-flavour channel $pp \rightarrow e^+ e^- \nu \bar{\nu}$

In this section we discuss results for  $pp \rightarrow e^+ e^- \nu \bar{\nu}$  at 13 TeV, including all neutrino flavours, i.e.

$$d\sigma(pp \rightarrow e^+ e^- \nu \bar{\nu}) = \sum_{\ell=e,\mu,\tau} d\sigma(pp \rightarrow e^+ e^- \nu_\ell \bar{\nu}_\ell). \quad (4.17)$$

As discussed in Section 2, the  $e^+ e^- \nu_e \bar{\nu}_e$  channel receives contributions from  $ZZ$  and  $WW$  diboson resonances, while the channels with  $\mu^-$  and  $\tau^-$  neutrinos involve only  $ZZ$  resonances. In order to disentangle the individual contributions of  $WW$  and  $ZZ$  resonances to the full cross section (4.17), we define

$$\begin{aligned} d\sigma(pp \rightarrow WW \rightarrow e^+ e^- \nu \bar{\nu}) &= d\sigma(pp \rightarrow WW \rightarrow e^+ e^- \nu_e \bar{\nu}_e) \\ &= d\sigma(pp \rightarrow e^+ \mu^- \nu_e \bar{\nu}_\mu), \end{aligned} \quad (4.18)$$

and

$$d\sigma(pp \rightarrow ZZ \rightarrow e^+ e^- \nu \bar{\nu}) = 3 \times d\sigma(pp \rightarrow e^+ e^- \nu_\mu \bar{\nu}_\mu), \quad (4.19)$$

where  $ZZ$  or  $WW$  resonances are excluded by selecting  $2\ell 2\nu$  flavour configurations that admit only interactions between  $\ell^+ \nu$  and  $\ell^- \bar{\nu}$  final states or  $\ell^+ \ell^-$  and  $\nu \bar{\nu}$  final states, respectively. The  $WW$  cross section (4.18) is dominated by  $WW$  diboson resonances and is free from  $ZZ$  resonances. By definition, it includes all resonant and non-resonant topologies that contribute to  $pp \rightarrow e^+ \mu^- \nu_e \bar{\nu}_\mu$ , and it receives contributions only from the  $pp \rightarrow e^+ e^- \nu_e \bar{\nu}_e$  channel. Similarly, the  $ZZ$  cross section (4.19) is dominated by  $ZZ$  diboson resonances and is free from  $WW$  resonances. It involves only resonant and non-resonant topologies that contribute to  $pp \rightarrow e^+ e^- \nu_\mu \bar{\nu}_\mu$ , and it receives contributions from all neutrino flavours. The various neutrino-flavour contributions to (4.17) are related to (4.18)–(4.19) through

$$d\sigma(pp \rightarrow e^+ e^- \nu_\mu \bar{\nu}_\mu) = d\sigma(pp \rightarrow e^+ e^- \nu_\tau \bar{\nu}_\tau) = \frac{1}{3} d\sigma(pp \rightarrow ZZ \rightarrow e^+ e^- \nu \bar{\nu}), \quad (4.20)$$

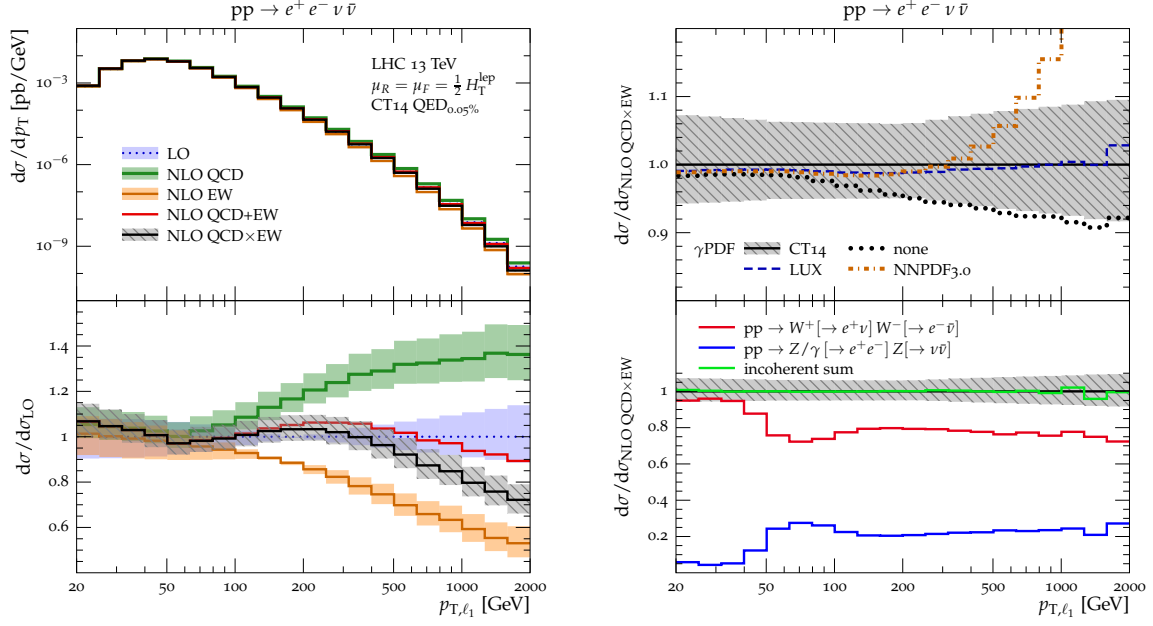


**Figure 16.** Distribution in the transverse momentum of the leading lepton,  $p_{T,\ell_1}$ , for  $pp \rightarrow e^+ e^- \nu \bar{\nu}$  at 13 TeV. All neutrino flavours,  $\nu = \nu_e, \nu_\mu, \nu_\tau$ , are included. Left and upper-right plots as in Fig. 9. The lower-right ratio plot shows the relative weight of the  $W^+W^- \rightarrow e^+ e^- \nu \bar{\nu}$  and  $ZZ \rightarrow e^+ e^- \nu \bar{\nu}$  contributions, as defined in (4.18)–(4.19), as well as their incoherent sum (4.22).

and the following separation holds

$$\begin{aligned} d\sigma(pp \rightarrow e^+ e^- \nu_e \bar{\nu}_e) &= d\sigma(pp \rightarrow WW \rightarrow e^+ e^- \nu \bar{\nu}) + \frac{1}{3} d\sigma(pp \rightarrow ZZ \rightarrow e^+ e^- \nu \bar{\nu}) \\ &+ d\sigma_{\text{int}}, \end{aligned} \quad (4.21)$$

where  $d\sigma_{\text{int}}$  stands for the interference between topologies of  $WW$  and  $ZZ$  type. As we will see, the splitting of the DF cross section into a  $WW$  and a  $ZZ$  channel (and the interference of the two) is very instructive in order to understand the shapes and higher-order corrections of certain kinematic distributions, which are affected to a different extent by these two dominant contributions in different regions of phase space.

A selection of differential distributions is presented in Figs. 16–22. Similarly as in Section 4.1, in every figure we illustrate NLO QCD and EW predictions with corresponding  $K$ -factors (left plot) as well as  $\gamma$ -induced effects (upper-right plot). Since the NLO QCD $\times$ EW $_{\text{VI}} \otimes$  YFS and NLO QCD $\times$ EW $_{\text{VI}} \otimes$  CSS approximations behave similarly as for the different-flavour process, we do not show corresponding plots.<sup>9</sup> Instead, in the lower-right panels we quantify the relative importance of the  $WW$  and  $ZZ$  contributions defined in (4.18)–(4.19), as well as their incoherent sum,

$$\begin{aligned} &d\sigma(pp \rightarrow WW \rightarrow e^+ e^- \nu \bar{\nu}) + d\sigma(pp \rightarrow ZZ \rightarrow e^+ e^- \nu \bar{\nu}) \\ &= \sum_{\ell=e,\mu,\tau} d\sigma(pp \rightarrow e^+ e^- \nu_\ell \bar{\nu}_\ell) - d\sigma_{\text{int}}. \end{aligned} \quad (4.22)$$

<sup>9</sup> It should be noted, however, that the NLO QCD $\times$ EW $_{\text{VI}} \otimes$  YFS and NLO QCD $\times$ EW $_{\text{VI}} \otimes$  CSS approximations reproduce the generally subdominant  $ZZ$  processes to much higher precision in the TeV regime than the dominant  $WW$  processes.



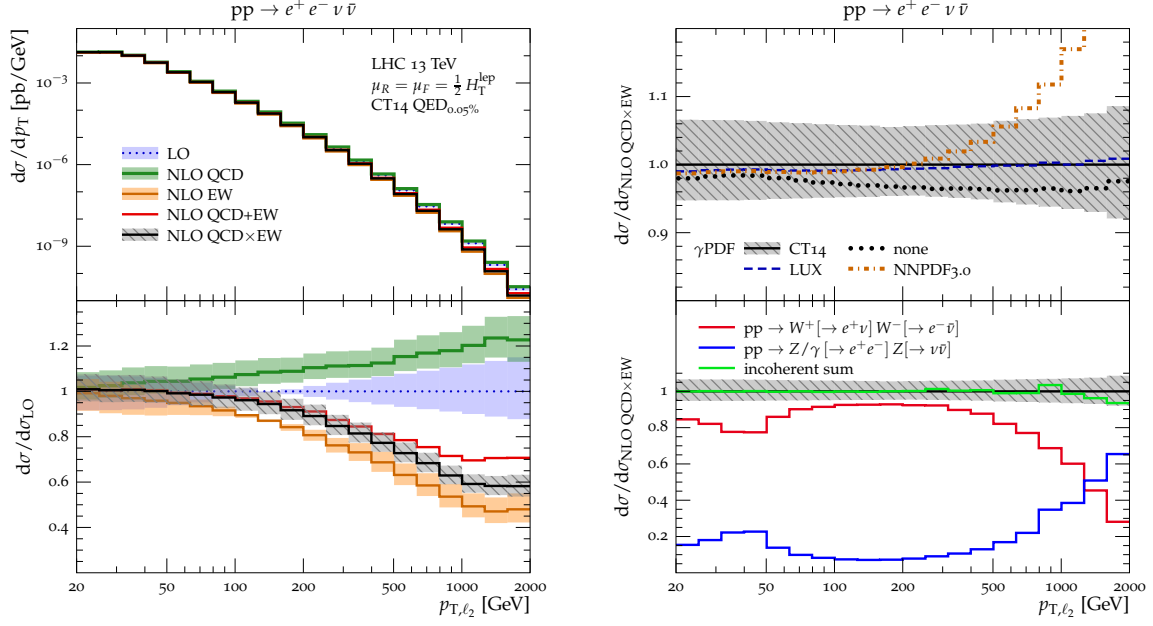


**Figure 17.** Distribution in the transverse momentum of the subleading lepton,  $p_{T,\ell_2}$ , for  $pp \rightarrow e^+ e^- \nu \bar{\nu}$  at 13 TeV. Details as in Fig. 16.

The most striking evidence emerging from Figs. 16–19 is that the incoherent sum (4.22) provides an excellent approximation of the full  $e^+ e^- \nu \bar{\nu}$  cross section at NLO QCD  $\times$  EW level. In fact, in all considered observables, apart from the far off-shell tail of the four-lepton invariant mass distribution  $m_{\ell\ell\nu\nu}$  shown in Fig. 22, interference effects are so suppressed that they cannot be resolved at all with the available Monte Carlo statistics.

The integrated  $e^+ e^- \nu \bar{\nu}$  cross section, the distributions in  $p_{T,\ell_1}$  (Fig. 16),  $p_{T,\ell_2}$  (Fig. 17),  $m_{\ell\ell}$  (Fig. 19), and  $\Delta\phi_{\ell\ell}$  (Fig. 22) are dominated by  $WW$  resonances in the majority of the plotted range. In those regions it is not surprising to observe that QCD and EW corrections behave very similarly as in the different-flavour case discussed in Section 4.1. Vice versa, in the presence of sizeable  $ZZ$  contributions, radiative corrections can behave in a different manner as compared to the different-flavour case. For example, this is observed in the tail of the  $p_{T,\ell_2}$  distribution beyond 1 TeV. There,  $ZZ$  resonance contributions become as important as  $WW$  ones, resulting in a reduction of the magnitude and a change in shape of the EW corrections. Similarly, the size of the contributions from  $\gamma$ -induced processes is reduced as compared to  $pp \rightarrow e^+ \mu^- \nu_e \bar{\nu}_\mu$  (Fig. 10).

In the  $\cancel{E}_T$  distribution (Fig. 18) we observe a more intriguing interplay between  $WW$  and  $ZZ$  resonances. While  $WW$  topologies represent the main contribution at low and very high  $\cancel{E}_T$ , the region between 100 GeV and 1 TeV is dominated by  $ZZ$  resonances. This is related to the fact—already observed in the different-flavour case—that the production of a  $\nu\bar{\nu}$  system via  $WW$  resonances is strongly suppressed for  $\cancel{E}_T > M_W$ . In the  $pp \rightarrow e^+ e^- \nu \bar{\nu}$  channel, this suppression manifests itself through the enhancement of  $ZZ$  contributions, where large  $\cancel{E}_T$  can directly arise through a boosted  $Z$  boson decaying to  $\nu\bar{\nu}$ . In contrast, due to the absence of  $ZZ$  resonances, in the  $e^+ \mu^- \nu_e \bar{\nu}_\mu$  channel the suppression of  $WW$  resonances leads to the enhancement of radiative effects at NLO QCD and NLO EW. Vice versa, due to the opening of  $ZZ$  resonances, in the  $e^+ e^- \nu \bar{\nu}$  channel we observe smaller NLO QCD and photon-induced contributions and larger negative NLO EW corrections.

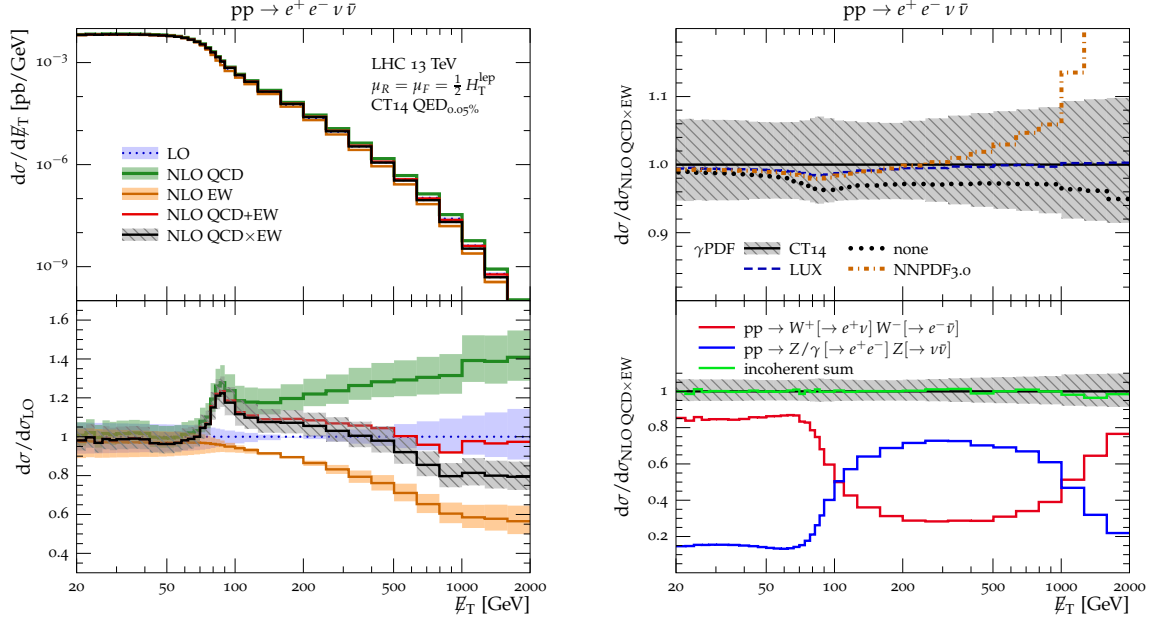


**Figure 18.** Distribution in the missing transverse momentum,  $E_T$ , for  $pp \rightarrow e^+e^- \nu \bar{\nu}$  at 13 TeV. Details as in Fig. 16.

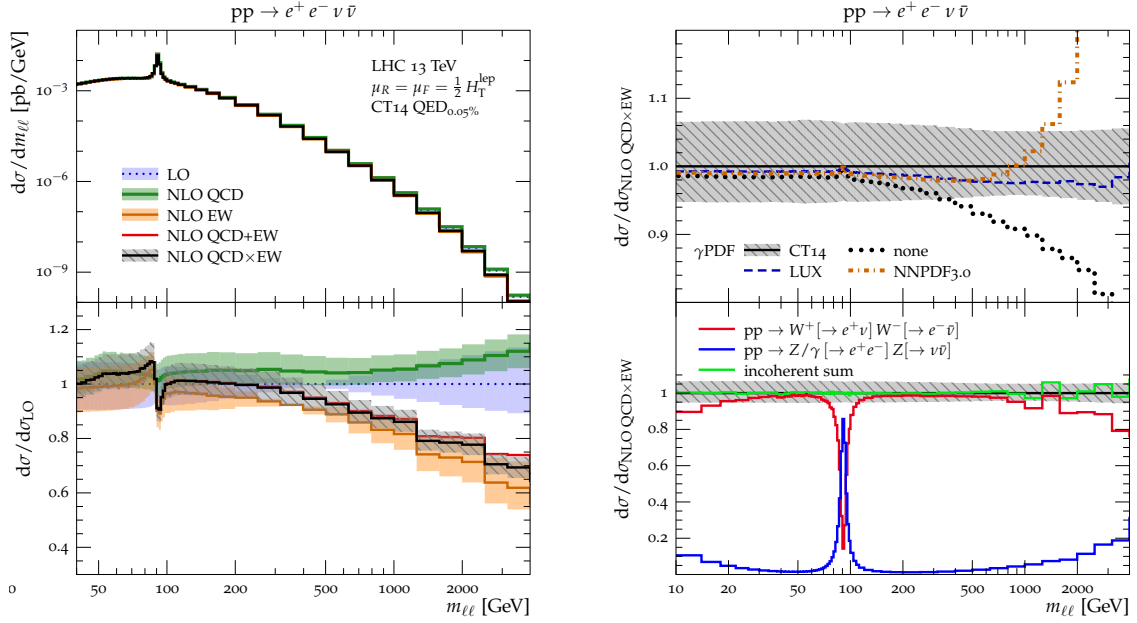


**Figure 19.** Distribution in the  $e^+e^-$  pair,  $m_{\ell\ell}$ , for  $pp \rightarrow e^+e^- \nu \bar{\nu}$  at 13 TeV. Details as in Fig. 16.

The invariant mass of the  $e^+e^-$  pair (Fig. 19) represents a powerful discriminant between  $WW$  and  $ZZ$  channels. On the one hand, most of the spectrum is driven by  $WW$  contributions and behaves very similarly as for the corresponding different-flavour observable shown in Fig. 12. On the other hand, in the vicinity of  $m_{\ell\ell} \approx M_Z$ , the  $ZZ$  channel gives rise to a sharp  $Z \rightarrow e^+e^-$  peak well above the  $WW$  continuum. In this region photon radiation off the charged leptons induces

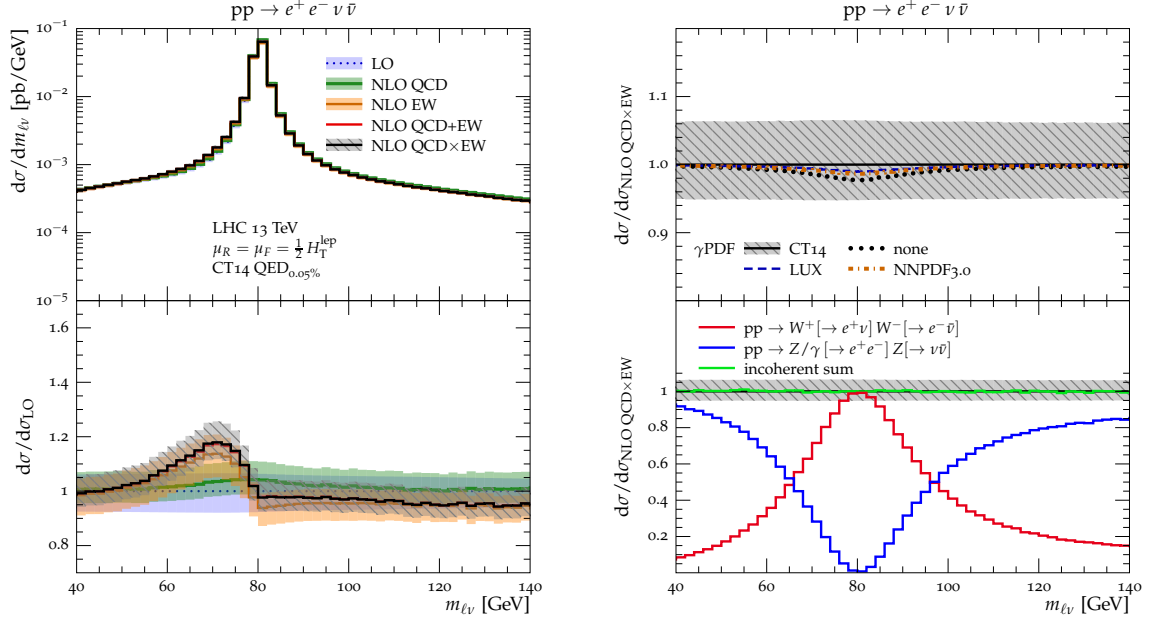


**Figure 20.** Distribution in the invariant mass of one matching lepton-neutrino pair,  $m_{\ell\nu}$ , for  $pp \rightarrow e^+ e^- \nu \bar{\nu}$  at 13 TeV. Details as in Fig. 16.

significant distortions of the  $Z$  line shape that are obviously not present in the DF case. Such shape corrections are qualitatively similar to those in Fig. 13 for the  $m_{\ell\nu}$  spectrum. However, since  $Z \rightarrow e^+ e^-$  decays involve two charged leptons, we find an even more significant reduction of the peak cross section. Moreover, due to the presence of a large  $WW$  background, the positive NLO EW  $K$ -factor below the peak turns out to be much less pronounced than in  $m_{\ell\nu}$ .

Similarly, the experimentally unobservable  $m_{\ell\nu}$  distribution shown in Fig. 20 for the SF case, while dominated by  $WW$  resonant channels near the  $W$  resonance, receives large contributions from  $ZZ$  channels on either side. Consequently, the large NLO EW corrections below the  $W$  peak in the  $WW$  channel, dominated by real photon radiation, cf. Fig. 13, are much smaller as they are diluted by the very small corrections for the  $ZZ$  channel.

The equally unobservable four-lepton invariant mass,  $m_{\ell\ell\nu\nu}$ , displayed in Fig. 21, shows similar features as its DF counterpart. Again, the reason is the dominance of the  $WW$  channels over much of its range. Only at very low invariant masses, near the  $Z$ -pole, the importance of the  $ZZ$  channels increases up to becoming dominant. This is the only regime out of all observables considered in this paper, where a visible interference effect between the  $WW$  and  $ZZ$  channels can be observed, reaching up to -25% on the  $Z$ -pole itself. This observation can be explained by the fact that this is the only region where at least one of the gauge bosons is forced off shell and both the  $WW$  and  $ZZ$  channels populate the same surviving resonance, cf. the diagrams of Fig. 1c and Fig. 2b.

Finally, Fig. 22 shows the azimuthal separation of both charged leptons. Here, due to the dominance of the  $WW$  channel throughout we observe very similar effects as already documented in Fig. 15 for the DF case.

Similarly as for the DF case, we have checked that the NLO QCD  $\times$  EW predictions of Figs. 19–22 are reproduced with sufficient accuracy by the NLO QCD  $\times$  EW<sub>VI</sub>  $\otimes$  YFS approximation.

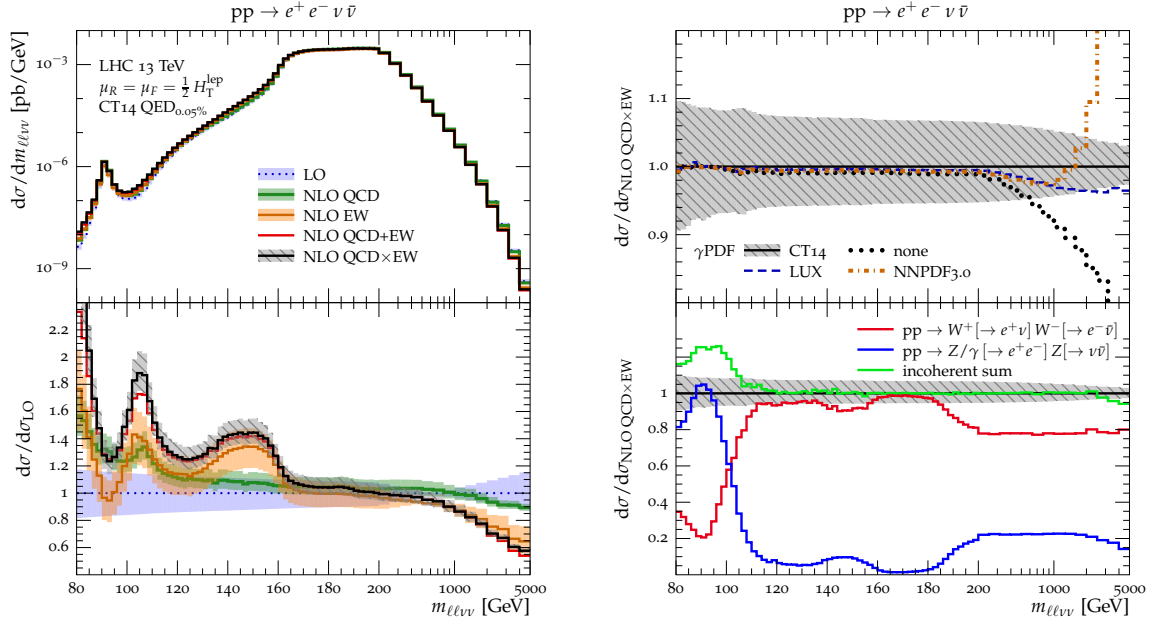


**Figure 21.** Distribution in the invariant mass of all four final state leptons and neutrinos,  $m_{\ell\ell\nu\nu}$ , for  $pp \rightarrow e^+e^-\nu\bar{\nu}$  at 13 TeV. Details as in Fig. 16.

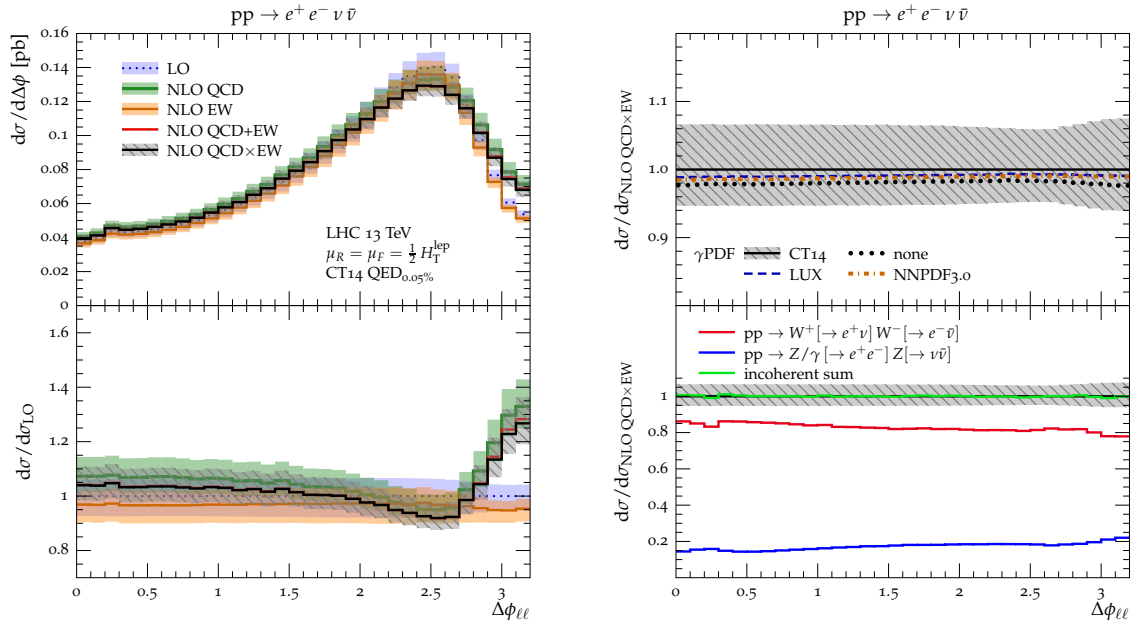


**Figure 22.** Distribution in the azimuthal separation of the  $e^+e^-$  pair,  $\Delta\phi_{\ell\ell}$ , for  $pp \rightarrow e^+e^-\nu\bar{\nu}$  at 13 TeV. Details as in Fig. 16.

## 5 Summary and conclusions

We have presented NLO QCD and EW predictions for  $e^+\mu^-\nu_e\bar{\nu}_\mu$  and  $e^+e^-\nu\bar{\nu}$  production at the LHC. These reactions are representative of all possible diboson processes  $pp \rightarrow WW/ZZ \rightarrow \ell_i^+ \ell_j^- \nu\bar{\nu}$ , which lead to signatures with two leptons of opposite charge plus missing transverse energy. Due to the large SU(2) charges of the intermediate  $W$  and  $Z$  bosons, the underlying  $q\bar{q} \rightarrow VV$  subprocesses induce huge EW Sudakov effects at high energy. As a result, in various observables we find negative EW corrections beyond  $-50\%$  at the TeV scale. Also QCD corrections can be sizeable, and in order to account for unknown NNLO contributions of  $\mathcal{O}(\alpha_S\alpha)$  in an approximate way, we have advocated a factorised combination of NLO QCD and EW corrections.

Photon-induced processes have been computed at NLO EW, taking into account the channels of type  $\gamma\gamma \rightarrow 2\ell 2\nu$ ,  $\gamma\gamma \rightarrow 2\ell 2\nu\gamma$ , and  $\gamma q \rightarrow 2\ell 2\nu q$ . In the tails of the  $m_{\ell\ell}$  and leading-lepton  $p_T$  distributions, such contributions can become important. In particular, the  $\cancel{E}_T$  distribution receives large  $\gamma$ -induced corrections starting already from about 100 GeV due to a suppression of the LO  $q\bar{q} \rightarrow WW$  process in this region. With the poorly constrained photon density of the NNPDF3.0qed fit,  $\gamma$ -induced processes can be strong enough to compensate the negative corrections of Sudakov type. However, based on the more precise photon densities in the CT14qed and LUXqed PDFs,  $\gamma$ -induced contributions can reach at most 10–20% and remain clearly subleading with respect to EW Sudakov logarithms.

For observables that are inclusive with respect to QED radiation, NLO EW corrections can be described with good accuracy by a so-called EW<sub>VI</sub> approximation, which includes only IR-subtracted virtual EW corrections and is particularly suitable in the context of multi-jet merging. However, for observables depending on charged leptons, also radiative QED effects can play an important role. Thus we have studied the possibility of augmenting the EW<sub>VI</sub> approximation through QED radiation effects generated via YFS soft-photon resummation or, alternatively, by the Catani–Seymour dipole-based DGLAP-type resummation of the CSSHOWER. In general, both approaches provide reasonably accurate results. More precisely, both approaches describe the high-energy regions on a similar level with deviations being typically smaller than 10%, while the YFS resummation implementation in SHERPA also preserves the existing resonance structure.

Radiative corrections in  $2\ell 2\nu$  channels with same and opposite lepton flavour behave in a fairly similar way. This can be understood in the light of the respective resonance structures. On the one hand,  $pp \rightarrow e^+\mu^-\nu_e\bar{\nu}_\mu$  solely contains  $W^+W^-$  resonances, while  $pp \rightarrow e^+e^-\nu\bar{\nu}$  involves both  $W^+W^-$  and  $ZZ$  resonances. On the other hand, possible interferences between  $W^+W^-$  and  $ZZ$  topologies turn out to be completely negligible for all relevant observables. Moreover,  $W^+W^-$  contributions to  $pp \rightarrow e^+e^-\nu\bar{\nu}$  are widely dominant with respect to  $ZZ$  ones. This is the reason why QCD and EW corrections behave very similarly in  $e^+e^-\nu\bar{\nu}$  and  $e^+\mu^-\nu_e\bar{\nu}_\mu$  production. Nevertheless, we have pointed out that NLO effects can still be quite sensitive to the flavour structure in certain observables. This can for example be observed in the  $m_{\ell\ell}$  and  $\cancel{E}_T$  distributions in correspondence to the occurrence of  $ZZ$  dominated regions that originate, respectively, from the  $Z \rightarrow \ell^+\ell^-$  resonance and due to the suppression of  $W^+W^-$  topologies for  $\cancel{E}_T > M_W$ .

Concerning the treatment of hard scattering processes with external photons at NLO EW, in Appendix A we have presented a general analysis of the interplay between the definition of the coupling  $\alpha$  for external photons, the renormalisation of the photon wave function, and the renormalisation of the  $\gamma$ PDF. In particular, we have pointed out that, in order to avoid large logarithms associated with  $\Delta\alpha(M_Z^2)$ , the coupling  $\alpha$  for final- and initial-state photons should be defined, respectively, at high energy and in the Thomson limit,  $Q^2 \rightarrow 0$ . In practice, at energies of the order of the EW scale or above, initial-state photon couplings can be parametrised in the  $G_\mu$  scheme or in the  $\alpha(M_Z)$  scheme, while  $\alpha(0)$  should not be used.

The tools that have been used in this project—SHERPA, MUNICH, and OPENLOOPS—implement

automated NLO QCD+EW algorithms that are applicable to any Standard Model process and will be made publicly available in the near future.

## Acknowledgments

MS is grateful for illuminating discussions with G. Salam, C. Schmidt and C.-P. Yuan. This research was supported in part by the Swiss National Science Foundation (SNF) under contracts PP00P2-128552 and BSCGI0-157722 as well as by the Research Executive Agency (REA) of the European Union under the Grant Agreements PITN-GA-2010-264564 (*LHCPhenoNet*), PITN-GA-2012-315877 (*MCnet*), PITN-GA-2012-316704 (*HiggsTools*) and the ERC Advanced Grant MC@NNLO (340983).

## A Infrared subtraction, $\gamma$ PDF renormalisation and definition of $\alpha$

This Appendix starts, in Section A.1, with a general documentation of the implementation of Catani–Seymour subtraction at NLO EW in SHERPA and MUNICH. This serves as a basis for the discussion, in Sections A.2–A.3, of the cancellation of light-fermion mass singularities in processes with external photons. Such cancellations involve a subtle interplay between the definition of the coupling  $\alpha$ , the renormalisation of the  $\gamma$ PDF, and the photon wave-function renormalisation. In particular we point out that, in order to avoid a logarithmic sensitivity to light-quark and lepton masses, the coupling of on-shell final-state photons should be defined in the limit of vanishing  $Q^2$ , while for initial-state photons a definition of  $\alpha$  at the EW scale or at  $\mu_F^2 \sim \hat{s}$  should be used. This was first noticed in [25], based on arguments related to the evolution of the  $\gamma$ PDF at LO, and is confirmed by our explicit analysis at NLO EW.

### A.1 Catani–Seymour subtraction at $\mathcal{O}(\alpha)$

In this section we present the implementation of Catani–Seymour subtraction at NLO EW in SHERPA and MUNICH. While the construction of Catani–Seymour dipoles for QED radiation has been discussed in detail in [37–39], our implementation relies on the direct transposition of the original  $\mathcal{O}(\alpha_S)$  subtraction formalism [35, 36] to  $\mathcal{O}(\alpha)$ . In the following, we provide the complete set of formulae that permits to obtain  $\mathcal{O}(\alpha)$  dipoles from the results of [35] for massless partons, thereby extending the schematic description given in [26]. Moreover, we point out some subtle aspects related to leptonic contributions and external photons, which are relevant for the cancellation of fermion-mass logarithms discussed in Sections A.2–A.3.

Let us consider the  $\mathcal{O}(\alpha)$  corrections to a  $2 \rightarrow m$  hard-scattering process. The subtraction term for the singularities stemming from photon- or fermion-bremsstrahlung in the  $(m+1)$ -parton phase space has the general form

$$d\sigma^A = - \sum_{I \in \mathcal{S}_{\text{in+out}}} \sum_{J \in \mathcal{S}_{\text{out}}} \frac{1}{2p_I p_J} \sum_{K \neq I, J} Q_{\widetilde{IJ}, K} \hat{V}_{IJ, K} \otimes d\sigma^B|_{IJ \rightarrow \widetilde{IJ}}, \quad (\text{A.1})$$

where  $\mathcal{S}_{\text{in+out}} = \mathcal{S}_{\text{in}} \cup \mathcal{S}_{\text{out}}$  is the full set of initial-state ( $\mathcal{S}_{\text{in}}$ ) and final-state ( $\mathcal{S}_{\text{out}}$ ) partons. Each term in the triple sum over  $I$ ,  $J$  and  $K$  describes  $1/(p_I p_J)$  singularities arising from the exchange of a soft parton  $J$  between an emitter  $I$  and a spectator  $K$ , as well as collinear singularities involving the partons  $I, J$ . The relevant splitting kernels  $\hat{V}_{IJ, K}$  in (A.1) are convoluted with the reduced Born cross section  $d\sigma^B|_{IJ \rightarrow \widetilde{IJ}}$ , where the partons  $I$  and  $J$  are clustered into a single parton  $\widetilde{IJ}$  according to the respective splitting process.<sup>10</sup> The various types of splitting kernels are listed in Table 3. In general we consider  $\mathcal{O}(\alpha)$  emissions off quarks and leptons, generically denoted as  $f = q, \bar{q}, \ell^-, \ell^+$ ,

<sup>10</sup>For details of the  $\mathbf{V} \otimes d\sigma^B$  convolution, such as kinematic mappings, we refer to [35].

dipole type	$I$	$J$	$K$	splitting	$\hat{\mathbf{V}}_{IJ,K}$
final-final	$i \in \mathcal{S}_{\text{out}}$	$j \in \mathcal{S}_{\text{out}}$	$k \in \mathcal{S}_{\text{out}}$	$ij \rightarrow i + j$	$\mathbf{V}_{ij,k}$
final-initial	$i \in \mathcal{S}_{\text{out}}$	$j \in \mathcal{S}_{\text{out}}$	$b \in \mathcal{S}_{\text{in}}$	$ij \rightarrow i + j$	$x_{ij,b}^{-1} \mathbf{V}_{ij}^b$
initial-final	$a \in \mathcal{S}_{\text{in}}$	$j \in \mathcal{S}_{\text{out}}$	$k \in \mathcal{S}_{\text{out}}$	$a \rightarrow (aj) + j$	$x_{jk,a}^{-1} \mathbf{V}_k^{aj}$
initial-initial	$a \in \mathcal{S}_{\text{in}}$	$j \in \mathcal{S}_{\text{out}}$	$b \in \mathcal{S}_{\text{in}}$	$a \rightarrow (aj) + j$	$x_{j,ab}^{-1} \mathbf{V}^{aj,b}$

**Table 3.** Correspondence between the generic splitting kernels  $\hat{\mathbf{V}}_{IJ,K}$  of (A.1) and the kernels  $\mathbf{V}$  of [35]. For initial-state and final-state partons we use specific indices  $a, b \in \mathcal{S}_{\text{in}}$  and  $i, j, k \in \mathcal{S}_{\text{out}}$ . Moreover, since the emittee  $J \in \mathcal{S}_{\text{out}}$  we identify  $J = j$ . The terms with initial-state emitters,  $I = a \in \mathcal{S}_{\text{in}}$ , describe splittings  $a \rightarrow (aj) + j$ , while final-state emitters,  $I = i \in \mathcal{S}_{\text{out}}$ , corresponds to splittings  $(ij) \rightarrow i + j$ . The spectators  $K$  can be either initial-state ( $K = b$ ) or final-state ( $K = k$ ) partons.

as well as photon splittings. Explicit expressions for  $\hat{\mathbf{V}}_{IJ,K}$  corresponding to  $f \rightarrow f\gamma$  and  $\gamma \rightarrow f\bar{f}$  splittings can be obtained from the corresponding QCD kernels [35] for  $q \rightarrow qg$ ,  $\bar{q} \rightarrow \bar{q}g$ , and  $g \rightarrow q\bar{q}$  splittings by replacing

$$\alpha_s \rightarrow \alpha, \quad C_F \rightarrow Q_f^2, \quad T_R \rightarrow N_{C,f} Q_f^2, \quad n_f T_R \rightarrow \sum_f N_{C,f} Q_f^2, \quad C_A \rightarrow 0, \quad (\text{A.2})$$

where  $N_{c,f} = 1$  for leptons and 3 for quarks. As discussed in Appendix A.2, all terms  $\sum_f N_{C,f} Q_f^2$ , which arise from massless fermion-loop insertions in the photon propagator or related real-emission contributions, should include both quarks and charged leptons. The matrix  $Q_{\widetilde{IJ},K}$  in (A.1) collects the charge factors of the partons  $\widetilde{IJ}$  and  $K$ . It is related to the colour-insertion operators of [35] via

$$\frac{\mathbf{T}_{\widetilde{IJ}} \cdot \mathbf{T}_K}{\mathbf{T}_{\widetilde{IJ}}^2} \rightarrow Q_{\widetilde{IJ},K}. \quad (\text{A.3})$$

If emitter  $\widetilde{IJ}$  is a charged fermion, we simply have

$$Q_{\widetilde{IJ},K} = \frac{Q_{\widetilde{IJ}} Q_K}{Q_{\widetilde{IJ}}^2} \quad \text{for } \widetilde{IJ} = f \in \mathcal{S}_{\text{in+out}}, \quad (\text{A.4})$$

where  $Q$  is the incoming charge, e.g.  $Q = \mp 1$  ( $\pm 1$ ) for an incoming (outgoing)  $\ell^\mp$ . For a photon emitter,  $\widetilde{IJ} = \gamma$ , (A.4) is not applicable due to  $Q_\gamma = 0$ . This situation occurs for final-state  $\gamma \rightarrow f\bar{f}$  splittings and initial-state  $f \rightarrow \gamma f$  splittings, which involve only collinear singularities that are insensitive to the electromagnetic charge of the spectator  $K$ . In fact, the role of the spectator is merely to absorb the recoil resulting from the splitting process, and the matrix  $Q_{\widetilde{IJ},K}$  in (A.1) distributes the recoil to the various spectators based on the identity

$$\sum_{K \neq \widetilde{IJ}} Q_{\widetilde{IJ},K} = -1, \quad (\text{A.5})$$

which is a manifestation of the charge-conservation relation  $\sum_K Q_K = 0$ . Since  $Q_{\gamma,K}$  does not need to be related to the actual charges of the spectators  $K$ , any matrix  $Q_{\gamma,K}$  that obeys (A.5) guarantees a consistent IR subtraction. The choice implemented in SHERPA and MUNICH for initial-state photon emitters reads

$$Q_{a,K} = -\delta_{b,K} \quad \text{for } a = \gamma \in \mathcal{S}_{\text{in}}. \quad (\text{A.6})$$

Here,  $a$  and  $b$  denote the two initial-state partons, i.e. the recoil of initial-state  $\gamma \rightarrow f\bar{f}$  splittings is absorbed by the initial-state partner  $b$  of the emitter photon  $a$ .



$AB$	$P^{AB}(x)$	$\overline{K}^{AB}(x)$	$\tilde{K}^{AB}(x)$
$f\gamma$	$Q_f^2 \frac{1+(1-x)^2}{x}$	$P^{f\gamma}(x) \ln \frac{1-x}{x} + Q_f^2 x$	$P^{f\gamma}(x) \ln(1-x)$
$\gamma f$	$N_{C,f} Q_f^2 [x^2 + (1-x)^2]$	$P^{\gamma f}(x) \ln \frac{1-x}{x} + 2N_{C,f} Q_f^2 x(1-x)$	$P^{\gamma f}(x) \ln(1-x)$
$ff$	$Q_f^2 \left( \frac{1+x^2}{1-x} \right)_+$	$Q_f^2 \left[ \tilde{G}^{ff}(x) - \delta(1-x)(5-\pi^2) \right]$	$Q_f^2 \left[ \tilde{G}^{ff}(x) - \frac{\pi^2}{3} \delta(1-x) \right]$
$\gamma\gamma$	$\gamma_\gamma \delta(1-x)$	$-\frac{8}{3} \gamma_\gamma \delta(1-x)$	0

**Table 4.** Explicit expressions for  $P^{AB}$ ,  $\overline{K}^{AB}$ , and  $\tilde{K}^{AB}$  in (A.15) for all relevant combinations of photons and fermions,  $f = q, \bar{q}, \ell^+, \ell^-$ , with the auxiliary functions  $\tilde{G}^{ff}(x) = \left( \frac{2}{1-x} \ln \frac{1-x}{x} \right)_+ - (1+x) \ln \frac{1-x}{x} + (1-x)$  and  $\tilde{G}^{ff}(x) = \left( \frac{2}{1-x} \ln(1-x) \right)_+ - (1+x) \ln(1-x)$ .

Final-state  $\gamma \rightarrow f\bar{f}$  splittings should not be considered for processes with identified on-shell photons. However, they should be taken into account when photons are not distinguished from  $f\bar{f}$  pairs. In order to account for both cases in a flexible way, we introduce a discriminator  $\epsilon_{\text{FS},\gamma_i}$  for every final-state photon, defined as

$$\epsilon_{\text{FS},\gamma_i} = \begin{cases} 1 \\ 0 \end{cases} \quad \text{when final-state } \gamma_i \rightarrow f\bar{f} \text{ splittings are } \begin{cases} \text{allowed} \\ \text{disallowed} \end{cases}. \quad (\text{A.7})$$

The  $\epsilon_{\text{FS},\gamma_i}$  can be set individually for each photon, taking care that the prescription is infrared safe. Of course, if multiple photons fulfil the identification criteria simultaneously the assignment has to be properly symmetrised.<sup>11</sup> The charge correlation matrix in SHERPA and MUNICH is then chosen as<sup>12</sup>

$$Q_{\gamma_i,K} = -\frac{1}{2} \epsilon_{\text{FS},\gamma_i} (\delta_{a,K} + \delta_{b,K}) \quad \text{for every } \gamma_i \in \mathcal{S}_{\text{out}}. \quad (\text{A.8})$$

In this way, when final-state  $\gamma_i \rightarrow f\bar{f}$  splittings are allowed the resulting recoil is shared by the two initial-state partons  $a$  and  $b$ .

The cancellation of soft and collinear singularities against virtual corrections requires the analytic integrals of the dipole terms (A.1) supplemented by PDF-factorisation counterterms. This leads to [35]

$$\begin{aligned} \int_1 d\sigma_{ab}^A + \sigma_{ab}^{\text{CT}}(\mu_F) &= \mathbf{I}(\{p\}; \epsilon) d\sigma_{ab}^B(p_a, p_b) \\ &+ \int_0^1 dx \sum_{a'} [\mathbf{P}(\{p\}; x, \mu_F^2) + \mathbf{K}(x)]^{a,a'} d\sigma_{a'b}^B(xp_a, p_b) \\ &+ \int_0^1 dx \sum_{b'} [\mathbf{P}(\{p\}; x, \mu_F^2) + \mathbf{K}(x)]^{b,b'} d\sigma_{ab'}^B(p_a, xp_b), \end{aligned} \quad (\text{A.9})$$

<sup>11</sup> One example may be the production of an isolated photon accompanied by a jet, which at  $\mathcal{O}(\alpha^2)$  can be described by  $q\bar{q} \rightarrow \gamma\gamma$ . Now, once an isolated photon is found, for which we set  $\epsilon_{\text{FS},\gamma_i} = 0$ , the remaining photon forming the jet at LO is allowed to split, thus its  $\epsilon_{\text{FS},\gamma_i} = 1$ .

<sup>12</sup> Other recoil strategies for initial and final state photon splittings are possible and a number of generic choices is implemented in SHERPA.

where the various  $d\sigma_{ab}^{\text{B}}$  terms denote reduced Born cross sections that result from the clustering of an unresolved parton. All IR divergences are captured by the  $\mathbf{I}$  operator. For massless fermions at  $\mathcal{O}(\alpha)$  it reads

$$\mathbf{I}(\{p\}; \epsilon) = -\frac{\alpha}{2\pi} C_\epsilon \sum_{I \in \mathcal{S}_{\text{in+out}}} \mathcal{V}_I(\epsilon) \sum_{\substack{K \in \mathcal{S}_{\text{in+out}} \\ K \neq I}} Q_{I,K} \left( \frac{\mu_{\text{D}}^2}{2p_I \cdot p_K} \right)^\epsilon, \quad (\text{A.10})$$

with

$$C_\epsilon = \frac{(4\pi)^\epsilon}{\Gamma(1-\epsilon)} = 1 + \epsilon \left[ \ln(4\pi) - \gamma_{\text{E}} \right] + \mathcal{O}(\epsilon^2), \quad (\text{A.11})$$

$$\mathcal{V}_I(\epsilon) = Q_I^2 \left( \frac{1}{\epsilon^2} - \frac{\pi^2}{3} \right) + \gamma_I \frac{1}{\epsilon} + \gamma_I + K_I, \quad (\text{A.12})$$

and

$$\gamma_f = \frac{3}{2} Q_f^2, \quad \gamma_\gamma = -\frac{2}{3} \sum_f N_{C,f} Q_f^2, \quad K_f = Q_f^2 \left( \frac{7}{2} - \frac{\pi^2}{6} \right), \quad K_\gamma = \frac{5}{3} \gamma_\gamma, \quad (\text{A.13})$$

for  $f = q, \bar{q}, \ell^-, \ell^+$ . The fermion sum in (A.13) runs over massless fermions and includes a single term per fermion–antifermion pair. As discussed in Appendix A.2, all massless leptons and quarks should be taken into account, i.e.

$$\gamma_\gamma = -\frac{2}{3} \sum_f N_{C,f} Q_f^2 = -\frac{6N_{0,\ell} + 8N_{0,u} + 2N_{0,d}}{9}, \quad (\text{A.14})$$

where  $N_{0,\ell}$ ,  $N_{0,u}$  and  $N_{0,d}$  are the number of massless leptons and quarks of type up and down, respectively.

The  $\mathbf{P}$  and  $\mathbf{K}$  operators in (A.9) read

$$\mathbf{P}^{a,a'}(\{p\}; x; \mu_{\text{F}}^2) = \frac{\alpha}{2\pi} P^{aa'}(x) \sum_{\substack{K \in \mathcal{S}_{\text{in+out}} \\ K \neq a'}} Q_{a',K} \ln \frac{\mu_{\text{F}}^2}{2x p_a p_K}, \quad (\text{A.15})$$

$$\mathbf{K}^{a,a'}(x) = \frac{\alpha}{2\pi} \left\{ \overline{K}^{aa'}(x) + \delta^{aa'} \sum_{i \in \mathcal{S}_{\text{out}}} Q_{i,a'} \gamma_i \left[ \left( \frac{1}{1-x} \right)_+ + \delta(1-x) \right] \right\} - \frac{\alpha}{2\pi} Q_{a',b} \widetilde{K}^{aa'}(x),$$

where  $b$  stands for the initial-state partner of  $a$ . All relevant ingredients are specified in Table 4. Note that  $\mathcal{S}_{\text{in+out}} = \mathcal{S}_{\text{in}} \cup \mathcal{S}_{\text{out}}$  in (A.10) and (A.15) should be understood as the incoming and outgoing partons of the relevant Born sub-process. The  $\mathbf{P}$  and  $\mathbf{K}$  operators are free from soft and collinear singularities. The former depends on the factorisation-scale  $\mu_{\text{F}}$  introduced via the PDF counterterm, while the latter depends on the factorisation scheme. The result (A.15) corresponds to the case of two initial-state hadrons in the  $\overline{\text{MS}}$  scheme and can be easily translated to the DIS scheme [35].

### Processes with resolved photons

For hard processes with resolved photons in the final state, real-emission processes corresponding to final-state  $\gamma \rightarrow f\bar{f}$  splittings and related subtraction terms should be omitted at  $\mathcal{O}(\alpha)$ . This is achieved by setting  $\epsilon_{\text{FS},\gamma_i} = 0$  in (A.8). Consequently, in the subtraction term (A.1) we have

$$Q_{f\bar{f},K}^{\widetilde{\gamma}} = 0 \quad \text{if } f\bar{f} \equiv \gamma \in \mathcal{S}_{\text{out}}, \quad \text{and } Q_{\widetilde{IJ},\gamma} = 0 \quad \text{if } \gamma \in \mathcal{S}_{\text{out}}. \quad (\text{A.16})$$

Thus, external photons contribute to (A.1) only through  $\widetilde{IJ} \rightarrow I + J$  final-state splittings of type  $f \rightarrow f\gamma$ , while they can contribute to all types of  $I \rightarrow \widetilde{IJ} + J$  initial-state splittings, i.e.  $\gamma \rightarrow f\bar{f}$ ,

$f \rightarrow \gamma f$ , and  $f \rightarrow f\gamma$ . In analogy to (A.16), for the matrix (identical)  $Q_{I,J}$  that enters the  $\mathbf{I}$ ,  $\mathbf{K}$  and  $\mathbf{P}$  operators we have

$$Q_{\gamma,K} = Q_{I,\gamma} = 0 \quad \text{if } \gamma \in \mathcal{S}_{\text{out}}. \quad (\text{A.17})$$

Thus, resolved final-state photons can be completely excluded from the sums over  $I \in \mathcal{S}_{\text{out}}$  and  $K \in \mathcal{S}_{\text{out}}$  in (A.10) and (A.15), and external photon contributions to  $\mathbf{I}$ ,  $\mathbf{K}$  and  $\mathbf{P}$  arise only through

$$Q_{\gamma,b} = -1 \quad \text{for } \gamma, b \in \mathcal{S}_{\text{in}}, \quad (\text{A.18})$$

i.e. from dipoles with initial-state emitters  $a = \gamma$  and initial-state spectators  $b$ .

### Processes with unresolved photons

For hard processes with unresolved photons in the final state, the  $\mathbf{I}$ ,  $\mathbf{P}$  and  $\mathbf{K}$  operators in (A.10) and (A.15), contain, as compared to the case of resolved photons, the following additional contributions from final-state  $\gamma \rightarrow f\bar{f}$  splittings,

$$\begin{aligned} \Delta_{\text{FS},\gamma} \mathbf{I}(\{p\}; \epsilon) &= \mathbf{I}(\{p\}; \epsilon) - \left[ \mathbf{I}(\{p\}; \epsilon) \right]_{\epsilon_{\text{FS},\gamma_i}=0} \\ &= \frac{\alpha}{4\pi} \gamma_\gamma C_\epsilon \sum_{\gamma_i \in \mathcal{S}_{\text{out}}} \epsilon_{\text{FS},\gamma_i} \left[ 2 \left( \frac{1}{\epsilon} + \frac{8}{3} \right) + \sum_{K \in \mathcal{S}_{\text{in}}} \ln \left( \frac{\mu_{\text{D}}^2}{2p_i \cdot p_K} \right) \right], \\ \Delta_{\text{FS},\gamma} \mathbf{K}^{a,a'}(x) &= \mathbf{K}^{a,a'}(x) - \left[ \mathbf{K}^{a,a'}(x) \right]_{\epsilon_{\text{FS},\gamma_i}=0} \\ &= -\frac{\alpha}{4\pi} \gamma_\gamma \delta^{aa'} \sum_{\gamma_i \in \mathcal{S}_{\text{out}}} \epsilon_{\text{FS},\gamma_i} \left[ \left( \frac{1}{1-x} \right)_+ + \delta(1-x) \right], \\ \Delta_{\text{FS},\gamma} \mathbf{P}^{a,a'}(\{p\}; x; \mu_{\text{F}}^2) &= \mathbf{P}^{a,a'}(\{p\}; x; \mu_{\text{F}}^2) - \left[ \mathbf{P}^{a,a'}(\{p\}; x; \mu_{\text{F}}^2) \right]_{\epsilon_{\text{FS},\gamma_i}=0} \\ &= 0. \end{aligned} \quad (\text{A.19})$$

### A.2 $\gamma$ PDF renormalisation

External-photon contributions to the  $\mathbf{I}$  operator (A.10) yield the collinear poles

$$\mathbf{I}(\{p\}; \epsilon) \Big|_{\gamma, \text{sing}} = \frac{\alpha}{2\pi} C_\epsilon \left[ n_\gamma^{(\text{in})} + n_{\gamma,\epsilon}^{(\text{out})} \right] \frac{\gamma_\gamma}{\epsilon}, \quad (\text{A.20})$$

where  $n_\gamma^{(\text{in})}$  and  $n_{\gamma,\epsilon}^{(\text{out})} = \sum_i \epsilon_{\text{FS},\gamma_i}$  are the number of incoming photons and outgoing unresolved photons. When final-state  $\gamma \rightarrow f\bar{f}$  splittings are disabled ( $\epsilon_{\text{FS},\gamma_i} = 0$ ), real bremsstrahlung at  $\mathcal{O}(\alpha)$  is free from collinear  $\gamma_\gamma/\epsilon$  poles originating from final-state photon emitters, and the only pole contributions are due to initial-state photons in (A.20). Such collinear singularities arise through the  $\mathcal{O}(\alpha)$  renormalisation of the photon PDF,

$$\hat{\gamma}(x, \mu_{\text{F}}) = \gamma(x) - \frac{\alpha}{2\pi} \left[ \frac{C_\epsilon}{\epsilon} + \ln \left( \frac{\mu_{\text{D}}^2}{\mu_{\text{F}}^2} \right) \right] \int_x^1 \frac{dy}{y} \left\{ \sum_f P_{\gamma f} \left( \frac{x}{y} \right) [f(y) + \bar{f}(y)] + P_{\gamma\gamma} \left( \frac{x}{y} \right) \gamma(y) \right\}. \quad (\text{A.21})$$

Here,  $\mu_{\text{D}}$  is the scale of the dimensional regularisation. The term proportional to  $P_{\gamma f}$  absorbs collinear singularities arising from real-emission processes where the (off-shell) initial-state photon originates from  $f \rightarrow \gamma f$  splittings. The remaining term is due to the  $\gamma\gamma$  splitting function (see Table 4),

$$P_{\gamma\gamma} \left( \frac{x}{y} \right) = \gamma_\gamma \delta \left( 1 - \frac{x}{y} \right), \quad (\text{A.22})$$

which consists only of virtual fermion-loop contributions associated with the photon wave function renormalisation. It can be understood as a negative correction to the  $\gamma$ PDF that compensates real  $\gamma \rightarrow f\bar{f}$  splittings. The corresponding splitting functions are related via the momentum sum rule

$$\int_0^1 dz z \left\{ P_{\gamma\gamma}(z) + \sum_f \left[ P_{f\gamma}(z) + P_{\bar{f}\gamma}(z) \right] \right\} = 1. \quad (\text{A.23})$$

Including also the logarithmic dependence on  $\mu_F$ , which appears in the  $\mathbf{P}$  operator in (A.15), the effect of the  $\gamma$ PDF renormalisation can be summarised through an overall renormalisation factor,

$$\delta Z_{\gamma,\text{PDF}} = \frac{\alpha}{2\pi} \gamma_\gamma \left[ \frac{C_\epsilon}{\epsilon} + \ln \left( \frac{\mu_D^2}{\mu_F^2} \right) \right], \quad (\text{A.24})$$

for each initial-state photon.

### Contributions from $\gamma \rightarrow \ell^+\ell^-$ splittings

Photon splittings into  $q\bar{q}$  and  $\ell^+\ell^-$  should be included on the same footing at  $\mathcal{O}(\alpha)$ . Thus, as pointed out above, the photon anomalous dimension of (A.14) should include both quark and lepton contributions. This should be clear, since  $\gamma_\gamma$  represents contributions of virtual type, and different kinds of fermion loops are indistinguishable. Moreover, omitting leptonic contributions to  $\gamma_\gamma$  would jeopardise the cancellations of fermion-mass singularities between (A.24) and the virtual corrections to the hard cross section (see Appendix A.3).

Since  $\gamma_\gamma$  in (A.24) arises from the renormalisation of the  $\gamma$ PDF of (A.21), virtual  $\gamma \rightarrow \ell^+\ell^-$  splittings should be taken into account also in the evolution of  $\gamma(x, \mu_F)$ . In addition, for consistency with the sum rule (A.23), also real  $\gamma \rightarrow \ell^+\ell^-$  splittings and thus lepton distributions should be included in the PDF evolution. While this is desirable from the theoretical viewpoint, the effect of  $\gamma \rightarrow \ell^+\ell^-$  splittings hardly exceeds 1% in the photon PDF [22] and is completely negligible in the quark PDFs. Moreover, lepton-induced processes are extremely suppressed at the LHC [70]. Thus, excluding  $\gamma \rightarrow \ell^+\ell^-$  splittings from the PDF evolution, as in the CT14qed set used in the nominal predictions in this paper, is well justified.

### A.3 Definition and renormalisation of $\alpha$ in processes with external photons

The collinear singularities in (A.24) have to be combined with corresponding singularities that arise from the 1-loop counterterms associated with the renormalisation of the photon wave function ( $\delta Z_{AA}$ ) and of the electromagnetic coupling  $\alpha$ . Such counterterms yield a universal correction factor

$$\delta Z_{\gamma,\text{virt}} = \frac{\delta\alpha}{\alpha} + \delta Z_{AA} \quad (\text{A.25})$$

for each external (incoming or outgoing) photon in the hard scattering process. In the following, in order to articulate the interplay between the renormalisation of  $\alpha$  and the cancellation of collinear singularities, we will focus on the contributions from light fermions with  $0 \leq m_f < M_Z$ , which can be either treated in dimensional regularisation or using finite fermion masses. While all massless and massive fermions are assumed to contribute to the virtual corrections and to the ultraviolet renormalisation, only massless fermions are assumed to be included in the Catani-Seymour subtraction and in the  $\gamma$ PDF renormalisation.

The photon wave function counterterm reads,

$$\delta Z_{AA} = -\Pi^{\gamma\gamma}(0) = -\Pi_{\text{light}}^{\gamma\gamma}(0) - \Pi_{\text{heavy}}^{\gamma\gamma}(0), \quad (\text{A.26})$$

where *light* and *heavy* refer, respectively, to light-fermion and top-quark plus bosonic contributions. The UV and collinear singularities in (A.26) can be separated from each other by rewriting

$$\Pi_{\text{light}}^{\gamma\gamma}(0) = \Pi_{\text{light}}^{\gamma\gamma}(M_Z^2) + \Delta\alpha(M_Z^2). \quad (\text{A.27})$$

Here<sup>13</sup>

$$\Pi_{\text{light}}^{\gamma\gamma}(M_Z^2) = -\frac{\alpha}{2\pi} \gamma_\gamma \left[ \frac{C_\epsilon}{\epsilon} + \ln \left( \frac{\mu_D^2}{M_Z^2} \right) + \frac{5}{3} \right] \quad (\text{A.28})$$

represents the UV divergent piece, while all collinear singularities are contained in

$$\begin{aligned} \Delta\alpha(M_Z^2) &= \Pi_{\text{light}}^{\gamma\gamma}(0) - \Pi_{\text{light}}^{\gamma\gamma}(M_Z^2) \\ &= \frac{\alpha}{2\pi} \gamma_\gamma \left[ \frac{C_\epsilon}{\epsilon} + \ln \left( \frac{\mu_D^2}{M_Z^2} \right) + \frac{5}{3} \right] - \frac{\alpha}{3\pi} \sum_{f \in F_m} N_{C,f} Q_f^2 \left[ \ln \left( \frac{m_f^2}{M_Z^2} \right) + \frac{5}{3} \right], \end{aligned} \quad (\text{A.29})$$

where the anomalous dimension  $\gamma_\gamma$ , defined in (A.14), accounts for all massless fermion loops, while the sum over  $f \in F_m$  includes all light fermions with  $0 < m_f < M_Z$ . As is well known,  $\Delta\alpha(M_Z^2)$  is associated with the running of  $\alpha$  from  $Q^2 = 0$  to  $Q^2 = M_Z^2$ . In order to arrive at a finite expression for  $\Delta\alpha(M_Z^2)$ , all fermions could be treated as massive, in which case  $\gamma_\gamma = 0$ . Alternatively, hadronic contributions to  $\Delta\alpha(M_Z^2)$  can be obtained via dispersion relations. However, we advocate the approach of choosing an appropriate definition of  $\alpha$ , such as to cancel all singularities associated with  $\Delta\alpha(M_Z^2)$  in the final result. As detailed in the following, such a definition depends on the presence of resolved external photons in the processes at hand.

### Resolved final-state photons

In processes with resolved on-shell photons that do not split into  $f\bar{f}$  pairs the collinear singularity from  $\delta Z_{AA}$  remains uncanceled unless the electromagnetic coupling is renormalised in the on-shell scheme. Thus,  $\alpha$  should be defined as the photon coupling in the on-shell limit  $q^2 \rightarrow 0$ . The resulting counterterm is related to the photon wave-function renormalisation via [71]

$$\frac{\delta\alpha(0)}{\alpha(0)} = -\delta Z_{AA} - \frac{\sin\theta_w}{\cos\theta_w} \delta Z_{ZA} = \Pi^{\gamma\gamma}(0) - 2 \frac{\sin\theta_w}{\cos\theta_w} \frac{\Sigma_T^{AZ}(0)}{M_Z^2}, \quad (\text{A.30})$$

where  $\theta_w$  is the weak mixing angle. Light-fermion contributions to (A.30) read

$$\left. \frac{\delta\alpha(0)}{\alpha(0)} \right|_{\text{light}} = \Pi_{\text{light}}^{\gamma\gamma}(0), \quad (\text{A.31})$$

since the  $\Sigma_T^{AZ}(0)$  term receives only bosonic contributions. This yields, for each on-shell photon in the final state,

$$\delta Z_{\gamma,\text{virt}} \Big|_{\text{OS,light}} = \left[ \frac{\delta\alpha(0)}{\alpha(0)} + \delta Z_{AA} \right]_{\text{light}} = 0, \quad (\text{A.32})$$

while using the  $\alpha(M_Z)$  scheme, cf. (A.35)–(A.36), would lead to

$$\delta Z_{\gamma,\text{virt}} \Big|_{M_Z,\text{light}} = \left[ \frac{\delta\alpha(M_Z^2)}{\alpha(M_Z^2)} + \delta Z_{AA} \right]_{\text{light}} = -\Delta\alpha(M_Z^2). \quad (\text{A.33})$$

Thus, as is well known, in order to avoid fermion-mass singularities from  $\Delta\alpha(M_Z^2)$  in the hard cross section, the couplings of on-shell (resolved) final-state photons should be parametrised in terms of  $\alpha(0)$ .

<sup>13</sup>For simplicity, in the following we omit mass-suppressed terms of  $\mathcal{O}(m_f^2/M_Z^2)$  from light fermions with  $0 < m_f < M_Z$ . However such terms are typically included in realistic calculations, as it is the case for the calculation presented in this paper.

## Initial-state photons and unresolved final-state photons

In the case of initial-state photons, virtual contributions to the  $\gamma$ PDF renormalisation (A.21) are designed such as to absorb the collinear singularity of  $\delta Z_{AA}$ . Thus, by construction, the combination

$$\begin{aligned} \delta Z_{AA} \Big|_{\text{light}} + \delta Z_{\gamma, \text{PDF}} &= -\Pi_{\text{light}}^{\gamma\gamma}(M_Z^2) - \frac{\alpha}{2\pi} \gamma_\gamma \left[ \ln \left( \frac{\mu_F^2}{M_Z^2} \right) + \frac{5}{3} \right] \\ &= \frac{\alpha}{3\pi} \sum_{f \in F_m} N_{C,f} Q_f^2 \left[ \ln \left( \frac{m_f^2}{M_Z^2} \right) + \frac{5}{3} \right], \end{aligned} \quad (\text{A.34})$$

is free from  $1/\epsilon$  mass singularities, and there is no need to adopt the  $\alpha(0)$  scheme. In fact, expressing the coupling of initial-state photons in terms of

$$\alpha(M_Z^2) = \frac{\alpha(0)}{1 - \Delta\alpha(M_Z^2)}, \quad (\text{A.35})$$

with counterterm

$$\frac{\delta\alpha(M_Z^2)}{\alpha(M_Z^2)} = \frac{\delta\alpha(0)}{\alpha(0)} - \Delta\alpha(M_Z^2) = \Pi_{\text{light}}^{\gamma\gamma}(M_Z^2) + \Pi_{\text{heavy}}^{\gamma\gamma}(0) - 2 \frac{\sin\theta_w}{\cos\theta_w} \frac{\Sigma_T^{AZ}(0)}{M_Z^2}, \quad (\text{A.36})$$

results in the overall initial-state photon factor

$$\begin{aligned} \delta Z_{\gamma, \text{virt}} \Big|_{M_Z, \text{light}} + \delta Z_{\gamma, \text{PDF}} &= \left[ \frac{\delta\alpha(M_Z^2)}{\alpha(M_Z^2)} + \delta Z_{AA} \right]_{\text{light}} + \delta Z_{\gamma, \text{PDF}} \\ &= -\frac{\alpha}{2\pi} \gamma_\gamma \left[ \ln \left( \frac{\mu_F^2}{M_Z^2} \right) + \frac{5}{3} \right] + \frac{\alpha}{3\pi} \sum_{f \in F_m} N_{C,f} Q_f^2 \left[ \ln \left( \frac{m_f^2}{M_Z^2} \right) + \frac{5}{3} \right], \end{aligned} \quad (\text{A.37})$$

which is manifestly free from  $1/\epsilon$  fermion-mass singularities, while, as usual, those degrees of freedom that do not contribute as active fermions in the PDF evolution give rise to logarithms of  $m_f$  in the hard-scattering cross section. Vice versa, using the  $\alpha(0)$  scheme for initial-state photons would lead to the divergent result

$$\begin{aligned} \delta Z_{\gamma, \text{virt}} \Big|_{\text{OS, light}} + \delta Z_{\gamma, \text{PDF}} &= \left[ \frac{\delta\alpha(0)}{\alpha(0)} + \delta Z_{AA} \right]_{\text{light}} + \delta Z_{\gamma, \text{PDF}} \\ &= \delta Z_{\gamma, \text{virt}} \Big|_{M_Z, \text{light}} + \delta Z_{\gamma, \text{PDF}} + \Delta\alpha(M_Z^2) \\ &= \frac{\alpha}{2\pi} \gamma_\gamma \left[ \frac{C_\epsilon}{\epsilon} + \ln \left( \frac{\mu_D^2}{\mu_F^2} \right) \right]. \end{aligned} \quad (\text{A.38})$$

A fully analogous cancellation mechanism applies also to unresolved final-state photons, where the term proportional to  $n_{\gamma, \epsilon}^{(\text{out})}$  in (A.20), which originates from final-state  $\gamma \rightarrow f\bar{f}$  splittings, plays a similar role as the  $\gamma$ PDF counterterm for initial-state photons.

Thus, in order to avoid fermion-mass singularities in the hard cross section, the couplings of initial-state photons and unresolved final-state photons should be parametrised in terms of  $\alpha(M_Z^2)$  or any other scheme where  $\alpha$  is defined at a hard scale, such as the  $G_\mu$ -scheme or a running  $\alpha(\mu_R^2)$  with  $\mu_R^2 \sim \hat{s}$ . For the case of initial-state photons, this was first pointed out in [25] based on arguments related to the PDF evolution.

## B Flavour-number scheme conversion

As discussed in Section 3.4, in order to avoid single-top contributions, we compute parton-level cross sections using  $m_b > 0$  and omitting external  $b$ -quarks, both in the initial and in the final state.

This approach corresponds to the four-flavour scheme, and can be consistently used in combination with five-flavour PDFs by applying a simple scheme conversion [66], which amounts to the following substitution at the level of squared Born matrix elements,

$$\mathcal{B}_{ij} \rightarrow \left\{ 1 + \frac{\alpha_S}{3\pi} T_R \left[ n_{ij}^{(\alpha_S)} \theta(\mu_R^2 - m_b^2) \log\left(\frac{m_b^2}{\mu_R^2}\right) - n_{ij}^{(g)} \theta(\mu_F^2 - m_b^2) \log\left(\frac{m_b^2}{\mu_F^2}\right) \right] \right\} \mathcal{B}_{ij}. \quad (\text{B.1})$$

Here  $ij \in \{q\bar{q}, gq, g\bar{q}, gg\}$  are the initial-state QCD partons, while  $n_{ij}^{(\alpha_S)}$  and  $n_{ij}^{(g)}$  are, respectively, the power of  $\alpha_S$  and the number of initial-state gluons in the channel at hand. For the process of interest in this paper,  $pp \rightarrow 2\ell 2\nu$ , initial-state gluons do not contribute at Born level, and in the  $q\bar{q}$  channel we have  $n_{q\bar{q}}^{(\alpha_S)} = n_{q\bar{q}}^{(g)} = 0$ . Thus, as far as QCD partons are concerned, the scheme conversion of (B.1) is trivial. However, the  $\gamma\gamma \rightarrow 2\ell 2\nu$  channel requires a non-zero scheme transformation,

$$\mathcal{B}_{\gamma\gamma} \rightarrow \left[ 1 - \frac{2\alpha}{3\pi} N_C Q_b^2 \theta(\mu_F^2 - m_b^2) \log\left(\frac{m_b^2}{\mu_F^2}\right) \right] \mathcal{B}_{\gamma\gamma}, \quad (\text{B.2})$$

which involves a single term, related to the scheme dependence of the photon PDF. Note that there is no scheme-conversion term associated with the electromagnetic coupling required since, usually,  $\alpha$  is not defined in the  $\overline{\text{MS}}$  scheme.

## C Electroweak corrections by parton luminosity

Figs. 23–24 and 25–26 detail the relative electroweak correction induced by each parton luminosity for the DF and SF  $pp \rightarrow 2\ell 2\nu$  production processes, respectively. Here, only the CT14qed PDF is used for the photon density. As described in Section 2, the  $pp \rightarrow 2\ell 2\nu$  production process at LO receives contributions from the  $q\bar{q}$  and  $\gamma\gamma$  channels, while at NLO EW also the  $q\gamma$  and  $\bar{q}\gamma$  channels arise. It needs to be noted that the relative contributions from different parton luminosities are factorisation scale dependent. In each figure, the upper panel shows the relative correction of the  $\gamma\gamma$ -induced production process at LO in addition to the relative size of the NLO EW corrections in the  $q\bar{q}$ -,  $q\gamma/\bar{q}\gamma$ - and  $\gamma\gamma$ -induced channels relative to the LO  $q\bar{q}$ -induced process. In addition it quantifies the size of the scheme conversion term (4.13) that originates when relating our definition of the multiplicative combination of NLO QCD and EW correction to another definition based upon individual corrections to both LO production channels. This scheme dependence is of relative  $\mathcal{O}(\alpha_S\alpha)$  and contributes generally 0.5%, rising to 5% in extreme regions. The lower panel compares the size of both electroweak Sudakov-like corrections to their respective Born process.

Naturally, the LO  $\gamma\gamma$ -induced correction is small but positive throughout. The NLO EW corrections are dominated by the  $q\bar{q}$ -channel exhibiting the usual Sudakov suppression at large transverse momenta. The distribution in the missing transverse momentum in the DF case provides an exception, the origins of which and its specific characteristics have been discussed in detail in Section 4.1.

The  $\gamma\gamma$ -induced NLO EW corrections are detailed both in the upper panel, showing their relative size in comparison to the LO  $q\bar{q}$  channel, and the lower panel, showing their relative size in comparison to the LO  $\gamma\gamma$  channel. While they contribute only small amounts to the total NLO EW correction, the comparison against the LO  $\gamma\gamma$  channel clearly exhibits their Sudakov-like behaviour as transverse momenta are increasing. Despite similar shapes, the size of this Sudakov-type correction is found to be slightly larger in the  $\gamma\gamma$  channel than in the  $q\bar{q}$  channel.

The NLO EW  $q\gamma$ - and  $\bar{q}\gamma$ -induced corrections that are associated with both LO processes show a different behaviour. At this order, no one-loop diagrams contribute and, thus, the Sudakov-type behaviour is absent. Instead, the corrections are positive and of a similar magnitude as the LO  $\gamma\gamma$  channel. Please note, since these two channels exhibit a final state quark or anti-quark, their precise



magnitudes are strongly dependent on the chosen form of the jet veto. Choosing a tighter veto, e.g. by applying a strict veto against any jet activity above 30 GeV, decreases their contribution, while loosening it, e.g. by not vetoing jets altogether, increases it.

In conclusion, while the NLO EW correction in the  $\gamma\gamma$  channel is dominated by EW Sudakov logarithms whose magnitude in the TeV region balances the additional power of  $\alpha$  to arrive at a result of the same magnitude as the LO  $\gamma\gamma$ -induced contribution, the NLO EW correction in the  $\gamma q$  and  $\gamma\bar{q}$  channels uses the replacement of one of its PDF by a quark or anti-quark PDF (relative to the LO  $\gamma\gamma$ -induced process) to cancel the additional power in  $\alpha$ . Thus, when summing all contributions that depend on the photon density in the proton, LO  $\gamma\gamma$  and NLO EW  $\gamma q$ -,  $\gamma\bar{q}$ - and  $\gamma\gamma$  channels, there are sizeable cancellations between the different contributions to the cross sections at NLO EW accuracy.

## D Cross section tables

This last section compiles, for reference, a list of cross sections and corrections with different phase-space cuts applied. Tables 5–6 detail the cross sections for DF and SF  $2\ell 2\nu$  production, while Tables 7–8 show the contribution from the SF<sub>WW/ZZ</sub> and one of the two SF<sub>ZZ</sub> channels making up the SF signature. We list cross sections and corrections for the inclusive fiducial phase space as well as three more exclusive phase-space regions focussing on various high- $p_T$  scenarios. In each case, the LO cross section serves as a reference to define the NLO QCD, NLO EW, NLO QCD+EW and NLO QCD×EW corrections, computed in our default setup using the CT14qed PDFs, cf. Section 3. The latter we consider our best prediction for each particle selection.

$pp \rightarrow e^+ \mu^- \nu_e \bar{\nu}_\mu$	inclusive	$p_{T,\ell_1} > 500 \text{ GeV}$	$\cancel{E}_T > 500 \text{ GeV}$	$m_{\ell\ell} > 1 \text{ TeV}$
$\sigma^{\text{LO}}$ [fb]	$299^{+6\%}_{-8\%}$	$0.079^{+7\%}_{-6\%}$	$0.017^{+8\%}_{-7\%}$	$0.149^{+7\%}_{-6\%}$
$\sigma^{\text{NLO QCD}}/\sigma^{\text{LO}}$	$1.04^{+7\%}_{-5\%}$	$1.34^{+11\%}_{-9\%}$	$1.41^{+13\%}_{-10\%}$	$1.06^{+5\%}_{-5\%}$
$\sigma^{\text{NLO EW}}/\sigma^{\text{LO}}$	$0.97^{+6\%}_{-7\%}$	$0.71^{+6\%}_{-5\%}$	$0.85^{+7\%}_{-6\%}$	$0.79^{+7\%}_{-6\%}$
$\sigma^{\text{NLO QCD+EW}}/\sigma^{\text{LO}}$	$1.01^{+7\%}_{-5\%}$	$1.05^{+10\%}_{-8\%}$	$1.27^{+12\%}_{-10\%}$	$0.85^{+5\%}_{-5\%}$
$\sigma^{\text{NLO QCD}\times\text{EW}}/\sigma^{\text{LO}}$	$1.01^{+7\%}_{-5\%}$	$0.95^{+8\%}_{-6\%}$	$1.21^{+11\%}_{-9\%}$	$0.83^{+4\%}_{-4\%}$
$\delta^{\text{LO}}_{\text{no } \gamma\text{PDF}}$	-1 %	-4 %	-5 %	-6 %
$\delta^{\text{LO}}_{\text{LUXqed}}$	0 %	-0 %	-0 %	-0 %
$\delta^{\text{LO}}_{\text{NNPDF3.0qed}}$	-0 %	8 %	12 %	6 %
$\delta^{\text{NLO QCD}\times\text{EW}}_{\text{no } \gamma\text{PDF}}$	-2 %	-9 %	-9 %	-12 %
$\delta^{\text{NLO QCD}\times\text{EW}}_{\text{LUXqed}}$	-1 %	-1 %	-0 %	-3 %
$\delta^{\text{NLO QCD}\times\text{EW}}_{\text{NNPDF3.0qed}}$	-1 %	10 %	13 %	5 %

**Table 5.** Cross-sections for  $pp \rightarrow e^+ \mu^- \nu_e \bar{\nu}_\mu$  at 13 TeV with CT14qed PDFs and fiducial cuts of Table 2 (1<sup>st</sup> column) plus one additional cut on  $p_{T,\ell_1}$  (2<sup>nd</sup> column),  $\cancel{E}_T$  (3<sup>rd</sup> column), or  $m_{\ell\ell}$  (4<sup>th</sup> column). The top row lists LO cross sections, while the following four rows give the relative change induced by the NLO QCD, EW, QCD+EW and QCD×EW corrections. The sub- and superscripts give their respective relative uncertainties determined through customary  $\mu_R$  and  $\mu_F$  variations, while keeping the reference LO cross section fixed in the ratios. The impact of alternative descriptions of the photon density are explored by neglecting it entirely (no  $\gamma$ PDF) or using the densities provided by the LUXqed and NNPDF3.0qed sets. For quarks and gluons always the central PDF set CT14qed is chosen.

$pp \rightarrow e^+ e^- \nu \bar{\nu}$	inclusive	$p_{T,\ell_1} > 500 \text{ GeV}$	$\cancel{E}_T > 500 \text{ GeV}$	$m_{\ell\ell} > 1 \text{ TeV}$
$\sigma^{\text{LO}}$ [fb]	$368^{+6\%}_{-7\%}$	$0.108^{+7\%}_{-6\%}$	$0.074^{+7\%}_{-6\%}$	$0.158^{+7\%}_{-6\%}$
$\sigma^{\text{NLO QCD}}/\sigma^{\text{LO}}$	$1.04^{+7\%}_{-5\%}$	$1.32^{+11\%}_{-9\%}$	$1.30^{+10\%}_{-9\%}$	$1.06^{+6\%}_{-5\%}$
$\sigma^{\text{NLO EW}}/\sigma^{\text{LO}}$	$0.97^{+5\%}_{-7\%}$	$0.68^{+5\%}_{-5\%}$	$0.68^{+5\%}_{-4\%}$	$0.78^{+7\%}_{-6\%}$
$\sigma^{\text{NLO QCD+EW}}/\sigma^{\text{LO}}$	$1.00^{+7\%}_{-5\%}$	$1.00^{+9\%}_{-7\%}$	$0.98^{+8\%}_{-7\%}$	$0.84^{+5\%}_{-5\%}$
$\sigma^{\text{NLO QCD}\times\text{EW}}/\sigma^{\text{LO}}$	$1.00^{+6\%}_{-5\%}$	$0.90^{+7\%}_{-6\%}$	$0.89^{+7\%}_{-6\%}$	$0.83^{+4\%}_{-4\%}$
$\delta^{\text{LO}}_{\text{no } \gamma\text{PDF}}$	-1 %	-3 %	-1 %	-6 %
$\delta^{\text{LO}}_{\text{LUXqed}}$	0 %	-0 %	-0 %	-0 %
$\delta^{\text{LO}}_{\text{NNPDF3.0qed}}$	-0 %	6 %	3 %	6 %
$\delta^{\text{NLO QCD}\times\text{EW}}_{\text{no } \gamma\text{PDF}}$	-2 %	-7 %	-3 %	-10 %
$\delta^{\text{NLO QCD}\times\text{EW}}_{\text{LUXqed}}$	-1 %	-0 %	-0 %	-2 %
$\delta^{\text{NLO QCD}\times\text{EW}}_{\text{NNPDF3.0qed}}$	-1 %	7 %	3 %	4 %

**Table 6.** Cross-sections for  $pp \rightarrow e^+ e^- \nu \bar{\nu}$  at 13 TeV including all neutrino flavours. Higher-order corrections, scale uncertainties and photon-induced contributions are presented as in Table 5.

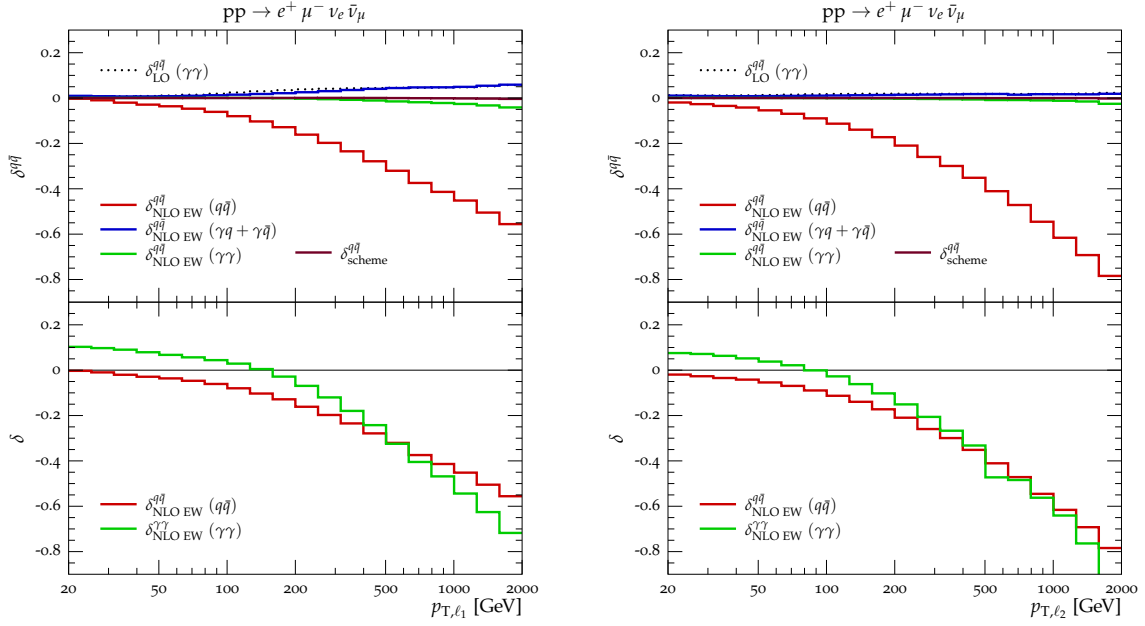


**Figure 23.** Relative corrections in the transverse momentum of the leading and subleading lepton,  $p_{T,\ell_1}$  and  $p_{T,\ell_2}$ , for  $pp \rightarrow e^+ \mu^- \nu_e \bar{\nu}_\mu$  at 13 TeV. In the upper panel we show the relative corrections to the LO  $q\bar{q}$  channel, induced by the LO  $\gamma\gamma$  channel ( $\delta_{LO}^{q\bar{q}}(\gamma\gamma)$ ), and the NLO EW  $q\bar{q}$ -,  $q\gamma/\bar{q}\gamma$ - and  $\gamma\gamma$ -induced processes ( $\delta_{NLO EW}^{q\bar{q}}(q\bar{q})$ ,  $\delta_{NLO EW}^{q\bar{q}}(\gamma q + \bar{q}\gamma)$ ,  $\delta_{NLO EW}^{q\bar{q}}(\gamma\gamma)$ , respectively). We further also show the relative size of the scheme conversion term of (4.13) with respect to the LO  $q\bar{q}$  channel ( $\delta_{scheme}^{q\bar{q}}$ ). The lower panel shows the  $q\bar{q}$ - and  $\gamma\gamma$ -induced NLO EW corrections relative to the LO cross section in the  $q\bar{q}$  and  $\gamma\gamma$  channel, respectively. At large transverse momenta, this corresponds to the channels' respective electroweak Sudakov corrections.

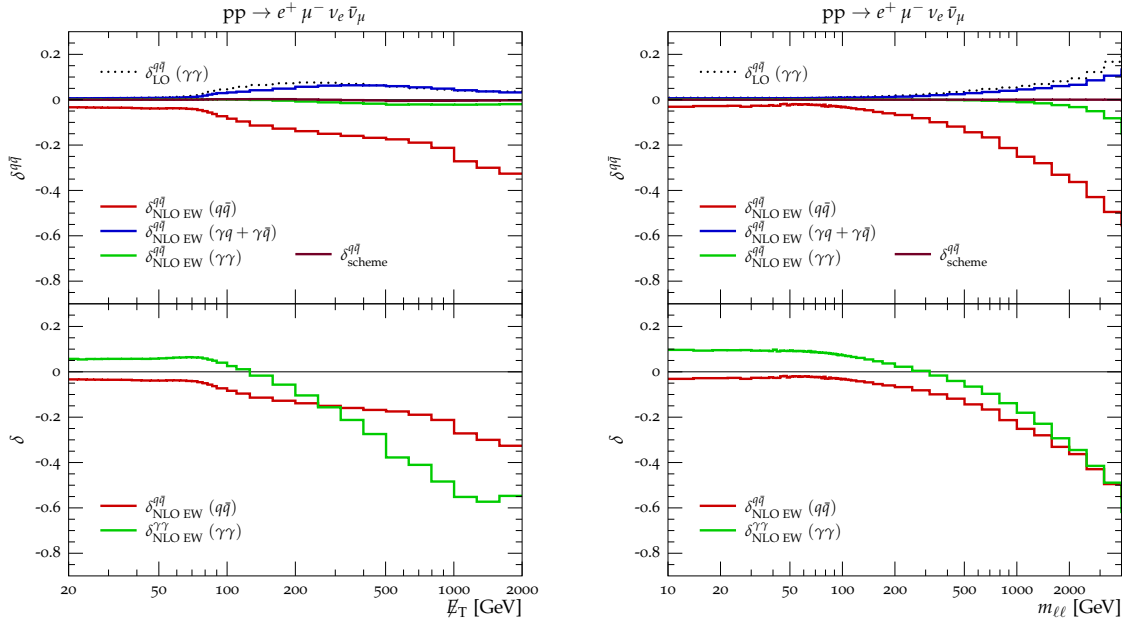


**Figure 24.** Relative corrections in the missing transverse momentum,  $E_T$ , and the invariant mass of the  $e^+ \mu^-$  pair,  $m_{\ell\ell}$ , for  $pp \rightarrow e^+ \mu^- \nu_e \bar{\nu}_\mu$  at 13 TeV. Details as in Fig. 23.

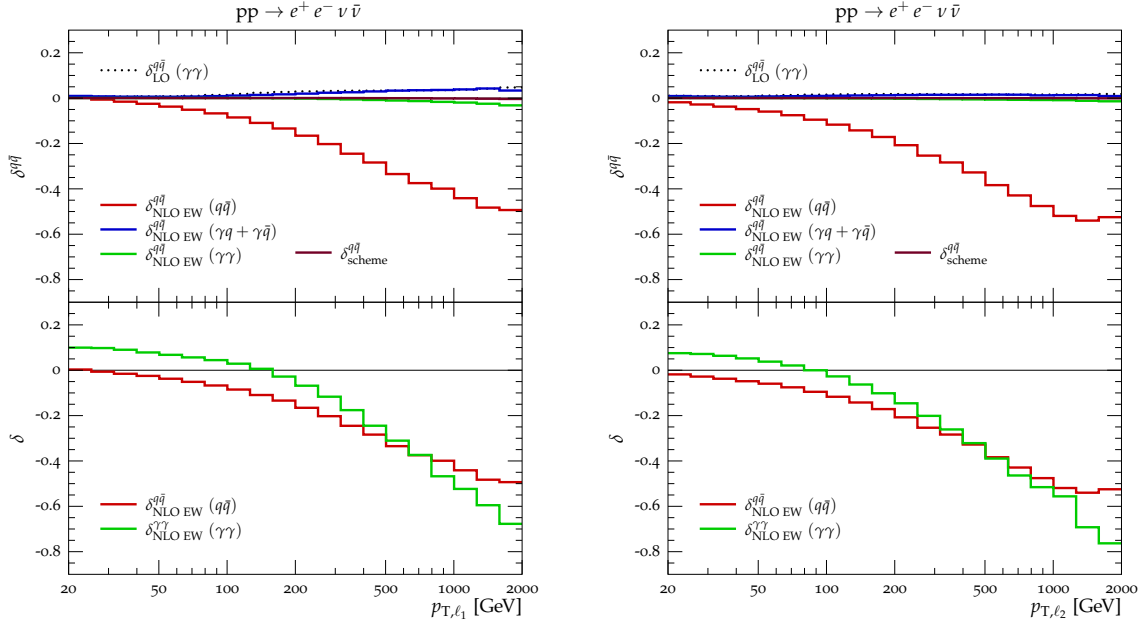


**Figure 25.** Relative corrections in the transverse momentum of the leading and subleading lepton,  $p_{T,\ell_1}$  and  $p_{T,\ell_2}$ , for  $pp \rightarrow e^+ e^- \nu \bar{\nu}$  at 13 TeV. Details as in Fig. 23.

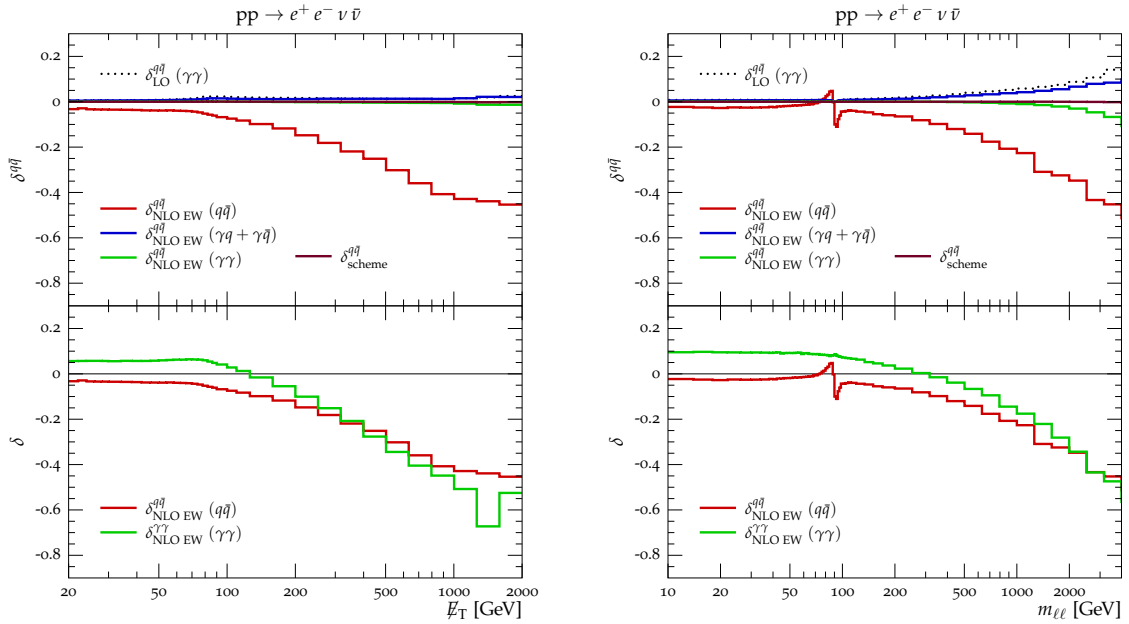


**Figure 26.** Relative corrections in the missing transverse momentum,  $E_T$ , and the invariant mass of the  $e^+ \mu^-$  pair,  $m_{\ell\ell}$ , for  $pp \rightarrow e^+ e^- \nu \bar{\nu}$  at 13 TeV. Details as in Fig. 23.

$pp \rightarrow e^+e^-\nu_e\bar{\nu}_e$	inclusive	$p_{T,\ell_1} > 500 \text{ GeV}$	$\cancel{E}_T > 500 \text{ GeV}$	$m_{\ell\ell} > 1 \text{ TeV}$
$\sigma^{\text{LO}}$ [fb]	$322^{+6\%}_{-8\%}$	$0.089^{+7\%}_{-6\%}$	$0.037^{+7\%}_{-6\%}$	$0.152^{+7\%}_{-6\%}$
$\sigma_{\text{QCD}}^{\text{NLO}}/\sigma^{\text{LO}}$	$1.04^{+7\%}_{-5\%}$	$1.33^{+11\%}_{-9\%}$	$1.34^{+11\%}_{-9\%}$	$1.06^{+5\%}_{-5\%}$
$\sigma_{\text{EW}}^{\text{NLO}}/\sigma^{\text{LO}}$	$0.97^{+5\%}_{-7\%}$	$0.69^{+6\%}_{-5\%}$	$0.73^{+6\%}_{-5\%}$	$0.78^{+7\%}_{-6\%}$
$\sigma_{\text{QCD}+\text{EW}}^{\text{NLO}}/\sigma^{\text{LO}}$	$1.01^{+7\%}_{-5\%}$	$1.02^{+9\%}_{-8\%}$	$1.07^{+10\%}_{-8\%}$	$0.84^{+5\%}_{-5\%}$
$\sigma_{\text{QCD}\times\text{EW}}^{\text{NLO}}/\sigma^{\text{LO}}$	$1.01^{+7\%}_{-5\%}$	$0.92^{+7\%}_{-6\%}$	$0.98^{+8\%}_{-7\%}$	$0.83^{+4\%}_{-4\%}$
$\delta_{\text{no } \gamma\text{PDF}}^{\text{LO}}$	-1 %	-4 %	-2 %	-6 %
$\delta_{\text{LUXqed}}^{\text{LO}}$	0 %	-0 %	-0 %	-0 %
$\delta_{\text{NNPDF3.0qed}}^{\text{LO}}$	-0 %	7 %	6 %	6 %
$\delta_{\text{no } \gamma\text{PDF}}^{\text{NLO QCD}\times\text{EW}}$	-2 %	-8 %	-5 %	-11 %
$\delta_{\text{LUXqed}}^{\text{NLO QCD}\times\text{EW}}$	-1 %	-0 %	-0 %	-2 %
$\delta_{\text{NNPDF3.0qed}}^{\text{NLO QCD}\times\text{EW}}$	-1 %	8 %	6 %	4 %

**Table 7.** Cross-sections for  $pp \rightarrow e^+e^-\nu_e\bar{\nu}_e$  at 13 TeV. Higher-order corrections, scale uncertainties and photon-induced contributions are presented as in Table 5.

$pp \rightarrow e^+e^-\nu_\mu\bar{\nu}_\mu$	inclusive	$p_{T,\ell_1} > 500 \text{ GeV}$	$\cancel{E}_T > 500 \text{ GeV}$	$m_{\ell\ell} > 1 \text{ TeV}$
$\sigma^{\text{LO}}$ [fb]	$23.0^{+5\%}_{-6\%}$	$0.0093^{+8\%}_{-7\%}$	$0.0187^{+7\%}_{-6\%}$	$0.0032^{+7\%}_{-7\%}$
$\sigma_{\text{QCD}}^{\text{NLO}}/\sigma^{\text{LO}}$	$1.01^{+6\%}_{-5\%}$	$1.25^{+9\%}_{-8\%}$	$1.26^{+9\%}_{-8\%}$	$1.09^{+6\%}_{-5\%}$
$\sigma_{\text{EW}}^{\text{NLO}}/\sigma^{\text{LO}}$	$0.95^{+5\%}_{-6\%}$	$0.65^{+5\%}_{-4\%}$	$0.63^{+4\%}_{-4\%}$	$0.81^{+6\%}_{-5\%}$
$\sigma_{\text{QCD}+\text{EW}}^{\text{NLO}}/\sigma^{\text{LO}}$	$0.96^{+6\%}_{-5\%}$	$0.90^{+7\%}_{-6\%}$	$0.89^{+7\%}_{-6\%}$	$0.90^{+5\%}_{-5\%}$
$\sigma_{\text{QCD}\times\text{EW}}^{\text{NLO}}/\sigma^{\text{LO}}$	$0.96^{+6\%}_{-5\%}$	$0.82^{+6\%}_{-5\%}$	$0.80^{+6\%}_{-5\%}$	$0.89^{+5\%}_{-4\%}$
$\delta_{\text{no } \gamma\text{PDF}}^{\text{LO}}$	-0.0 %	-0.4 %	-0.1 %	-1.4 %
$\delta_{\text{LUXqed}}^{\text{LO}}$	0.0 %	-0.0 %	-0.0 %	-0.0 %
$\delta_{\text{NNPDF3.0qed}}^{\text{LO}}$	-0.0 %	0.5 %	0.1 %	1.6 %
$\delta_{\text{no } \gamma\text{PDF}}^{\text{NLO QCD}\times\text{EW}}$	-0.0 %	-0.6 %	-0.1 %	-1.7 %
$\delta_{\text{LUXqed}}^{\text{NLO QCD}\times\text{EW}}$	-0.0 %	-0.0 %	-0.0 %	-0.3 %
$\delta_{\text{NNPDF3.0qed}}^{\text{NLO QCD}\times\text{EW}}$	-0.0 %	0.6 %	0.1 %	1.4 %

**Table 8.** Cross-sections for  $pp \rightarrow e^+e^-\nu_\mu\bar{\nu}_\mu$  at 13 TeV. Higher-order corrections, scale uncertainties and photon-induced contributions are presented as in Table 5.

## References

- [1] T. Gehrmann, M. Grazzini, S. Kallweit, P. Maierhöfer, A. von Manteuffel et al.,  *$W^+W^-$  Production at Hadron Colliders in Next to Next to Leading Order QCD*, *Phys.Rev.Lett.* **113** (2014) 212001, [[1408.5243](#)].
- [2] M. Grazzini, S. Kallweit, S. Pozzorini, D. Rathlev and M. Wiesemann,  *$W^+W$  production at the LHC: fiducial cross sections and distributions in NNLO QCD*, *JHEP* **08** (2016) 140, [[1605.02716](#)].
- [3] F. Cascioli, T. Gehrmann, M. Grazzini, S. Kallweit, P. Maierhöfer et al.,  *$ZZ$  production at hadron colliders in NNLO QCD*, *Phys.Lett.* **B735** (2014) 311–313, [[1405.2219](#)].
- [4] M. Grazzini, S. Kallweit and D. Rathlev,  *$ZZ$  production at the LHC: fiducial cross sections and distributions in NNLO QCD*, *Phys. Lett.* **B750** (2015) 407–410, [[1507.06257](#)].
- [5] F. Caola, K. Melnikov, R. Röntsch and L. Tancredi, *QCD corrections to  $ZZ$  production in gluon fusion at the LHC*, *Phys. Rev.* **D92** (2015) 094028, [[1509.06734](#)].
- [6] F. Caola, K. Melnikov, R. Röntsch and L. Tancredi, *QCD corrections to  $W^+W^-$  production through gluon fusion*, *Phys. Lett.* **B754** (2016) 275–280, [[1511.08617](#)].
- [7] A. Denner and S. Pozzorini, *One loop leading logarithms in electroweak radiative corrections. 1. Results*, *Eur.Phys.J.* **C18** (2001) 461–480, [[hep-ph/0010201](#)].
- [8] E. Accomando, A. Denner and A. Kaiser, *Logarithmic electroweak corrections to gauge-boson pair production at the LHC*, *Nucl. Phys.* **B706** (2005) 325–371, [[hep-ph/0409247](#)].
- [9] A. Bierweiler, T. Kasprzik, J. H. Kühn and S. Uccirati, *Electroweak corrections to  $W$ -boson pair production at the LHC*, *JHEP* **1211** (2012) 093, [[1208.3147](#)].
- [10] J. Baglio, L. D. Ninh and M. M. Weber, *Massive gauge boson pair production at the LHC: a next-to-leading order story*, *Phys.Rev.* **D88** (2013) 113005, [[1307.4331](#)].
- [11] S. Gieseke, T. Kasprzik and J. H. Kühn, *Vector-boson pair production and electroweak corrections in HERWIG++*, *Eur. Phys. J.* **C74** (2014) 2988, [[1401.3964](#)].
- [12] J. H. Kühn, F. Metzler, A. A. Penin and S. Uccirati, *Next-to-Next-to-Leading Electroweak Logarithms for  $W$ -Pair Production at LHC*, *JHEP* **06** (2011) 143, [[1101.2563](#)].
- [13] M. Billoni, S. Dittmaier, B. Jäger and C. Speckner, *Next-to-leading order electroweak corrections to  $pp \rightarrow W^+W^- \rightarrow 4$  leptons at the LHC in double-pole approximation*, *JHEP* **1312** (2013) 043, [[1310.1564](#)].
- [14] B. Biedermann, A. Denner, S. Dittmaier, L. Hofer and B. Jäger, *Electroweak corrections to  $pp \rightarrow \mu^+\mu^-e^+e^- + X$  at the LHC: a Higgs background study*, *Phys. Rev. Lett.* **116** (2016) 161803, [[1601.07787](#)].
- [15] B. Biedermann, A. Denner, S. Dittmaier, L. Hofer and B. Jäger, *Next-to-leading-order electroweak corrections to the production of four charged leptons at the LHC*, *JHEP* **01** (2017) 033, [[1611.05338](#)].
- [16] B. Biedermann, M. Billoni, A. Denner, S. Dittmaier, L. Hofer, B. Jäger et al., *Next-to-leading-order electroweak corrections to  $pp \rightarrow W^+W^- \rightarrow 4$  leptons at the LHC*, *JHEP* **06** (2016) 065, [[1605.03419](#)].
- [17] A. Denner, S. Dittmaier and R. Schuster, *Radiative corrections to  $\gamma\gamma \rightarrow W^+W^-$  in the electroweak standard model*, *Nucl. Phys.* **B452** (1995) 80–108, [[hep-ph/9503442](#)].
- [18] G. Jikia, *Electroweak  $O(\alpha)$  corrections to  $W^+W^-$  pair production in polarized gamma gamma collisions*, *Nucl. Phys.* **B494** (1997) 19–40, [[hep-ph/9612380](#)].
- [19] A. Bredenstein, S. Dittmaier and M. Roth, *Four-fermion production at gamma gamma colliders. 2. Radiative corrections in double-pole approximation*, *Eur. Phys. J.* **C44** (2005) 27–49, [[hep-ph/0506005](#)].
- [20] A. Martin, R. Roberts, W. Stirling and R. Thorne, *Parton distributions incorporating QED contributions*, *Eur.Phys.J.* **C39** (2005) 155–161, [[hep-ph/0411040](#)].

- [21] NNPDF collaboration, R. D. Ball et al., *Parton distributions with QED corrections*, *Nucl.Phys.* **B877** (2013) 290–320, [[1308.0598](#)].
- [22] C. Schmidt, J. Pumplin, D. Stump and C. P. Yuan, *CT14QED parton distribution functions from isolated photon production in deep inelastic scattering*, *Phys. Rev.* **D93** (2016) 114015, [[1509.02905](#)].
- [23] A. Manohar, P. Nason, G. P. Salam and G. Zanderighi, *How bright is the proton? A precise determination of the photon PDF*, [1607.04266](#).
- [24] S. Kallweit, J. M. Lindert, P. Maierhöfer, S. Pozzorini and M. Schönherr, *NLO QCD+EW Predictions for V+Jets Including Off-Shell Vector-Boson Decays and Multijet Merging*, [1511.08692](#).
- [25] L. A. Harland-Lang, V. A. Khoze and M. G. Ryskin, *Sudakov effects in photon-initiated processes*, *Phys. Lett.* **B761** (2016) 20–24, [[1605.04935](#)].
- [26] S. Kallweit, J. M. Lindert, P. Maierhöfer, S. Pozzorini and M. Schönherr, *NLO electroweak automation and precise predictions for W+multijet production at the LHC*, *JHEP* **04** (2015) 012, [[1412.5157](#)].
- [27] F. Cascioli, P. Maierhöfer and S. Pozzorini, *Scattering Amplitudes with Open Loops*, *Phys.Rev.Lett.* **108** (2012) 111601, [[1111.5206](#)].
- [28] The OPENLOOPS one-loop generator by F. Cascioli, J. Lindert, P. Maierhöfer and S. Pozzorini is publicly available at <http://openloops.hepforge.org>.
- [29] MUNICH is the abbreviation of “MULTi-chaNnel Integrator at Swiss (CH) precision”—an automated parton level NLO generator by S. Kallweit. In preparation.
- [30] T. Gleisberg, S. Höche, F. Krauss, M. Schönherr, S. Schumann, F. Siegert et al., *Event generation with SHERPA 1.1*, *JHEP* **02** (2009) 007, [[0811.4622](#)].
- [31] F. Krauss, R. Kuhn and G. Soff, *AMEGIC++ 1.0: A Matrix element generator in C++*, *JHEP* **0202** (2002) 044, [[hep-ph/0109036](#)].
- [32] T. Gleisberg and F. Krauss, *Automating dipole subtraction for QCD NLO calculations*, *Eur.Phys.J.* **C53** (2008) 501–523, [[0709.2881](#)].
- [33] M. Schönherr, *An automated subtraction of NLO EW infrared divergences*, [1712.07975](#).
- [34] A. Denner, S. Dittmaier, M. Roth and L. H. Wieders, *Electroweak corrections to charged-current  $e^+e^- \rightarrow 4$  fermion processes: Technical details and further results*, *Nucl. Phys.* **B724** (2005) 247–294, [[hep-ph/0505042](#)].
- [35] S. Catani and M. Seymour, *A General algorithm for calculating jet cross-sections in NLO QCD*, *Nucl.Phys.* **B485** (1997) 291–419, [[hep-ph/9605323](#)].
- [36] S. Catani, S. Dittmaier, M. H. Seymour and Z. Trocsanyi, *The Dipole formalism for next-to-leading order QCD calculations with massive partons*, *Nucl. Phys.* **B627** (2002) 189–265, [[hep-ph/0201036](#)].
- [37] S. Dittmaier, *A General approach to photon radiation off fermions*, *Nucl.Phys.* **B565** (2000) 69–122, [[hep-ph/9904440](#)].
- [38] S. Dittmaier, A. Kabelschacht and T. Kasprzik, *Polarized QED splittings of massive fermions and dipole subtraction for non-collinear-safe observables*, *Nucl.Phys.* **B800** (2008) 146–189, [[0802.1405](#)].
- [39] T. Gehrmann and N. Greiner, *Photon Radiation with MadDipole*, *JHEP* **1012** (2010) 050, [[1011.0321](#)].
- [40] A. Denner, S. Dittmaier and L. Hofer, *COLLIER – A fortran-library for one-loop integrals*, [1407.0087](#).
- [41] A. Denner and S. Dittmaier, *Reduction of one-loop tensor 5-point integrals*, *Nucl. Phys.* **B658** (2003) 175–202.
- [42] A. Denner and S. Dittmaier, *Reduction schemes for one-loop tensor integrals*, *Nucl. Phys.* **B734** (2006) 62–115.



- [43] A. Denner and S. Dittmaier, *Scalar one-loop 4-point integrals*, *Nucl. Phys.* **B844** (2011) 199–242.
- [44] G. Ossola, C. G. Papadopoulos and R. Pittau, *CutTools: A Program implementing the OPP reduction method to compute one-loop amplitudes*, *JHEP* **0803** (2008) 042, [[0711.3596](#)].
- [45] G. Ossola, C. G. Papadopoulos and R. Pittau, *Reducing full one-loop amplitudes to scalar integrals at the integrand level*, *Nucl.Phys.* **B763** (2007) 147–169, [[hep-ph/0609007](#)].
- [46] A. van Hameren, *OneLoop: For the evaluation of one-loop scalar functions*, *Comput.Phys.Commun.* **182** (2011) 2427–2438, [[1007.4716](#)].
- [47] S. Actis, A. Denner, L. Hofer, J.-N. Lang, A. Scharf and S. Uccirati, *RECOLA: REcursive Computation of One-Loop Amplitudes*, *Comput. Phys. Commun.* **214** (2017) 140–173, [[1605.01090](#)].
- [48] B. Biedermann, S. Brückner, A. Denner, M. Pellen, S. Schumann and J. M. Thompson, *Automation of NLO QCD and EW corrections with Sherpa and Recola*, [1704.05783](#).
- [49] J. H. Kühn, A. Kulesza, S. Pozzorini and M. Schulze, *Electroweak corrections to hadronic production of W bosons at large transverse momenta*, *Nucl.Phys.* **B797** (2008) 27–77, [[0708.0476](#)].
- [50] D. R. Yennie, S. C. Frautschi and H. Suura, *The infrared divergence phenomena and high-energy processes*, *Annals Phys.* **13** (1961) 379–452.
- [51] S. Schumann and F. Krauss, *A parton shower algorithm based on Catani-Seymour dipole factorisation*, *JHEP* **03** (2008) 038, [[0709.1027](#)].
- [52] S. Höche, S. Schumann and F. Siegert, *Hard photon production and matrix-element parton-shower merging*, *Phys. Rev.* **D81** (2010) 034026, [[0912.3501](#)].
- [53] M. Schönherr and F. Krauss, *Soft Photon Radiation in Particle Decays in SHERPA*, *JHEP* **12** (2008) 018, [[0810.5071](#)].
- [54] J. R. Andersen et al., *Les Houches 2015: Physics at TeV Colliders Standard Model Working Group Report*, in *9th Les Houches Workshop on Physics at TeV Colliders (PhysTeV 2015) Les Houches*, 2016. [1605.04692](#).
- [55] S. Alioli et al., *Precision Studies of Observables in  $pp \rightarrow W \rightarrow \ell\nu$  and  $pp \rightarrow \gamma, Z \rightarrow \ell^+\ell^-$  processes at the LHC*, Submitted to: Working Group Report (2016) , [[1606.02330](#)].
- [56] S. Höche, F. Krauss, M. Schönherr and F. Siegert, *A critical appraisal of NLO+PS matching methods*, *JHEP* **09** (2012) 049, [[1111.1220](#)].
- [57] T. Carli, T. Gehrmann and S. Höche, *Hadronic final states in deep-inelastic scattering with Sherpa*, *Eur. Phys. J.* **C67** (2010) 73–97, [[0912.3715](#)].
- [58] S. Höche, F. Krauss and M. Schönherr, *Uncertainties in MEPS@NLO calculations of h+jets*, *Phys. Rev.* **D90** (2014) 014012, [[1401.7971](#)].
- [59] PARTICLE DATA GROUP collaboration, K. Olive et al., *Review of Particle Physics*, *Chin.Phys.* **C38** (2014) 090001.
- [60] LHC HIGGS CROSS SECTION WORKING GROUP collaboration, S. Heinemeyer et al., *Handbook of LHC Higgs Cross Sections: 3. Higgs Properties*, [1307.1347](#).
- [61] A. Buckley, J. Ferrando, S. Lloyd, K. Nordström, B. Page, M. Rüfenacht et al., *LHAPDF6: parton density access in the LHC precision era*, *Eur. Phys. J.* **C75** (2015) 132, [[1412.7420](#)].
- [62] NNPDF collaboration, R. D. Ball et al., *Parton distributions for the LHC Run II*, *JHEP* **04** (2015) 040, [[1410.8849](#)].
- [63] V. M. Budnev, I. F. Ginzburg, G. V. Meledin and V. G. Serbo, *The Two photon particle production mechanism. Physical problems. Applications. Equivalent photon approximation*, *Phys. Rept.* **15** (1975) 181–281.
- [64] C. P. Yuan, *Update of the CT14 QED PDFs*, talk given at the PDF4LHC meeting on 13 Sep 2016.

- [65] C. Schmidt and C. P. Yuan. private communication.
- [66] M. Cacciari, M. Greco and P. Nason, *The  $P(T)$  spectrum in heavy flavor hadroproduction*, *JHEP* **05** (1998) 007, [[hep-ph/9803400](#)].
- [67] M. Rubin, G. P. Salam and S. Sapeta, *Giant QCD K-factors beyond NLO*, *JHEP* **09** (2010) 084, [[1006.2144](#)].
- [68] A. Buckley, J. Butterworth, L. Lönnblad, D. Grellscheid, H. Hoeth, J. Monk et al., *Rivet user manual*, *Comput. Phys. Commun.* **184** (2013) 2803–2819, [[1003.0694](#)].
- [69] M. L. Mangano et al., *Physics at a 100 TeV pp collider: Standard Model processes*, [1607.01831](#).
- [70] V. Bertone, S. Carrazza, D. Pagani and M. Zaro, *On the Impact of Lepton PDFs*, *JHEP* **11** (2015) 194, [[1508.07002](#)].
- [71] A. Denner, *Techniques for calculation of electroweak radiative corrections at the one loop level and results for W physics at LEP-200*, *Fortsch.Phys.* **41** (1993) 307–420, [[0709.1075](#)].